

Effects of Connections Detailing and Friction Dissipation Devices on the Seismic Response of a
Hospital Steel Braced Frame Building

Masaaki Ohira

A Thesis
in
The Department
of
Building, Civil & Environmental Engineering

Presented in Partial Fulfillment of the Requirements
for the Degree of Master of Applied Science (Civil Engineering) at
Concordia University
Montreal, Quebec, Canada

March 2020

© Masaaki Ohira, 2020

CONCORDIA UNIVERSITY
School of Graduate Studies

This is to certify that the thesis prepared

By: Masaaki Ohira

Entitled: Effects of Connections Detailing and Friction Dissipation Devices on the
Seismic Response of a Hospital Steel Braced Frame Building

and submitted in partial fulfillment of the requirement for the degree of

Master of Applied Science (Civil Engineering)

complies with the regulations of the University and meets the accepted standards with respect to originality and quality.

Signed by the final examining committee:

Dr. Anjan Bhowmick Chair

Dr. Emre Erkmen Examiner

Dr. Ion Stiharu Examiner

Dr. Lucia Tirca Supervisor

Approved by

Dr. M. Nokken, Chair of Department or Graduate Program Director

Dr. Amir Asif, Dean of Faculty

Date

ABSTRACT

Effects of Connections Detailing and Friction Dissipation Devices on the Seismic Response of a Hospital Steel Braced Frame Building

Masaaki Ohira

Hospitals are post-disaster buildings designed to withstand seismic forces that are amplified with an importance factor of $I_E=1.5$. Their seismic force-resisting system (SFRS) should be designed with $R_d > 2.0$, while the interstorey drift at each floor is limited to $1.0\%h_s$. Herein, R_d is the ductility-related force modification factor and h_s is the storey height. Although the non-structural components and the hospital contents are not part of this research, they constitute a larger loss in the event of an earthquake. As such, both interstorey drifts and floor accelerations should be within the required limits.

Concentrically braced frames (CBFs) are frequently employed as earthquake-resistant systems due to their high stiffness and moderate ductility. However, this system has shown several drawbacks such as the concentration of damage within a floor and high floor accelerations, which may be critical for acceleration-sensitive non-structural components. Recent experimental studies revealed that even moderately ductile concentrically braced frames (MD-CBF) may undergo unintended failure modes due to the limited deformation capacity of brace-to-frame connections. To overcome this drawback, it is proposed to provide an $8t_g$ elliptical clearance band in the brace-to-frame gusset plate instead of a linear $2t_g$ clearance, which is recommended by the code. Herein, t_g is the thickness of the gusset plate. The results pointed out that gusset plates with $8t_g$ elliptical clearance require less thickness than that with $2t_g$ linear clearance and provide larger rotation capacity. In consequence, the ductility of MD-CBF with brace-to-frame gusset plates detailed with $8t_g$ elliptical clearance is improved. Furthermore, in order to mitigate the floor acceleration, braces of CBFs can be replaced with sliding friction braces (SF), where each SF brace is made of a friction damper installed in-line with an HSS brace. The proposed sliding friction braced frame (SF-BF) system behaves elastically as a traditional CBF before friction devices are activated and experience nonlinear response after that. Thus, in the case of SF-BF system, the input energy is dissipated by friction devices and all adjacent members such as braces, connections, beams, and columns of the CBF system are designed to remain in the elastic range. It is noted that SF-BF systems are prone to residual interstorey drift, which can be

mitigated by: (i) using braced frame's columns continuous over all floors or (ii) adding back-up moment-resisting frames designed to provide the elastic frame action. The main objective of this thesis was three folds: (i) to investigate the inelastic behaviour of MD-CBF systems with $8t_g$ elliptical clearance gusset plate versus $2t_g$ linear clearance band; (ii) to develop an accurate numerical model for braces equipped with friction dampers using the OpenSees software and (iii) to examine the seismic response of SF-BF systems.

To carry out this research, a detailed model of a 4-storey hospital located in Victoria, BC on Site Class C was developed in OpenSees and subjected to 10 historical ground motions for nonlinear time-history analysis. In this manner, a model replicating the MD-CBF with $2t_g$ linear clearance band gusset plates for brace-to-frame connections and a model replicating the MD-CBF with $8t_g$ elliptical clearance band for brace-to-frame gusset plate detail were developed and the nonlinear time-history responses expressed in terms of interstorey drift, residual interstorey drift and floor acceleration were compared. A force-based design method was applied to design the SF-BF system. By optimizing the slip length and slip force in the damper, the slip-lock phase exhibited due to the bearing of the pretensioned bolts can be postponed while maintaining the drift below the code limits. Dynamic instability may become an issue when dampers with large slip lengths are installed.

From this research it was found that small difference was observed in the response of MD-CBFs when brace-to-frame gusset plates with $8t_g$ elliptical clearance was selected instead of $2t_g$ linear band detail. When the SF-BF system was designed using the force based design method, the HSS brace was proportioned such that the compression resistance of brace to be equal or greater than 130% slip force. Then, capacity design was employed to design the beams and columns of braced frames. An OpenSees model was developed to simulate the behaviour of Pall friction damper and brace assembly. From nonlinear dynamic analysis, it was found that large residual interstorey drift was observed when columns of braced frame were continuous over two storeys, although the interstorey drift is within the code limit, which is $1.0\%h_s$ for a hospital building. To mitigate the residual drift, continuous columns over the building height were considered. However, it was concluded that SF-BFs are not recommended for hospitals located in high risk seismic zones unless back-up moment-resisting frames designed for 25% base shear are provided.

ACKNOWLEDGEMENT

First and foremost, I would like to thank my thesis supervisor Dr. Lucia Tirca for her support and guidance throughout the years I've been privileged to work with her. Her passion for research has inspired me to question the assumptions to broaden my views and her dedication to mentoring her 'disciples' have taught me that teaching is a gift and not only a profession. Without her expertise, patience, and encouragements, this thesis would not have been possible.

I also want to extend my gratitude to Concordia University and its staff for providing me the necessary tools and professional networking to succeed as a graduate student and to grow as an engineer. I will miss my multicultural colleagues and friends: Ovidiu Serban, Mingzheng Wang, Melina Bosco, Leon Chen, Yudong Wang, Laura Manolache and all my office colleagues. It was a pleasure meeting you all! I hope our paths will cross again in the future.

To my family, words could not express the amount of gratitude I have for them. To my father who gave me the courage to pursue my passion, and to my mother who taught me to do so with integrity; I will forever be indebted to them for their selfless love and endless support. Now, that this chapter of my life has finally come to an end, I believe it is high time I returned the favour.

Last, but not least, to my beloved fiancée Thao who spent countless numbers of nights with me on this journey and who keeps me grounded when things get tough, I am truly blessed to have you. Thank you and I love you!

TABLE OF CONTENTS

LIST OF FIGURES.....	IX
LIST OF TABLES.....	XV
LIST OF SYMBOLS.....	XXI
CHAPTER 1 INTRODUCTION.....	1
1.1 GENERAL / BACKGROUND.....	1
1.2 OBJECTIVES AND SCOPE.....	3
1.3 DESCRIPTION OF METHODOLOGY	3
1.4 THESIS ORGANIZATION.....	4
CHAPTER 2 LITERATURE REVIEW.....	6
2.1 IMPORTANCE CATEGORIES FOR BUILDINGS	6
2.1.1 Importance Category and the Limit States Design according to NBCC 2010.....	6
2.1.2 Snow Load and Wind Load Calculation According to NBCC 2010	8
2.1.3 Earthquake Load Calculation According to NBCC 2010.....	9
2.2 SEISMIC DESIGN REQUIREMENTS FOR CONCENTRICALLY BRACED FRAMES AND SEISMIC DETAILING	11
2.2.1 Seismic Design of Centrically Braced Frames according to CSA S16 2009 standard.....	11
2.2.2 Learning from existing tests conducted on the brace and gusset plate systems of CBFs.....	14
2.2.3 Learning on the behaviour of CBF with elliptical clearance gusset plate connection	18
2.3 PAST STUDIES ON PALL FRICTION DAMPERS.....	27
2.4 MODELLING OF CONCENTRICALLY BRACED FRAMES USING OPENSEES	33
2.5 GUSSET PLATE WITH LINEAR CLEARANCE FOR BRACE-TO-FRAME CONNECTION.....	35
2.5.1 The geometry of $2t_g$ linear gusset plate.....	41
2.6 ELLIPTICAL CLEARANCE GUSSET PLATE	42
2.6.1 Rectangular gusset plate geometry design (Kotulka 2007).....	43
CHAPTER 3 BRACE-TO-FRAME CONNECTIONS	44
3.1 MODELLING OF GUSSET PLATE USING ABAQUS	46

3.2 FRICTION DAMPER IN-LINE WITH DIAGONAL BRACE	49
3.2.1 Modelling of friction damper in OpenSees	49
3.2.2 Calibration of parameters for the Bouc-Wen model.....	50
CHAPTER 4 CASE STUDY OF A HOSPITAL CBF BUILDING WITH ELLIPTICAL VERSUS TRADITIONAL GUSSET PLATE BRACE-TO-FRAME CONNECTIONS	53
4.1 DESIGN REQUIREMENTS FOR HOSPITAL BUILDINGS	53
4.1.1 Building description and geometry.....	53
4.1.2 Design of buildings with MD-CBF earthquake resisting system	61
4.1.3 Brace-to-frame connection design.....	68
4.2 OPENSEES MODEL	74
4.2.1 OpenSees framework	74
4.2.2 Model description of steel bracing member (brace, beam, column).....	74
4.2.3 Brace-to-frame connection modelling.....	78
4.3 NONLINEAR RESPONSE OF 4-STOREY HOSPITAL BUILDING	81
4.3.1 Ground motion selection and scaling	82
4.3.2 Nonlinear response of building at the design level $I_E=1.0$	84
4.3.3 Nonlinear response of CBF (E-W) corresponding to design spectrum amplified by $I_E=1.5$	95
CHAPTER 5 CASE STUDY OF HOSPITAL CBF BUILDING WITH FRICTION SLIDING BRACES	105
5.1 DESIGN OF CBF BUILDING WITH FRICTION SLIDING BRACES	105
5.2 CALIBRATION OF FRICTION DAMPERS IN OPENSEES	107
5.2.1 Elastic phase and sliding phase calibrations.....	108
5.2.2 Slip-lock phase calibration and failure.....	110
5.3 NONLINEAR RESPONSE OF 4-STOREY HOSPITAL BUILDING	112
5.3.1 Ground motion scaling	113
5.3.2 Nonlinear response	114
5.4 COMPARISON BETWEEN MD-CBF AND FS-BF SEISMIC RESPONSE	132
5.5 FS-BF WITH CONTINUOUS COLUMNS	138

CHAPTER 6 CONCLUSION AND FUTURE WORK.....	141
6.1 CONCLUSIONS	141
6.2 RECOMMENDATION FOR FUTURE WORK.....	143
REFERENCES	145

LIST OF FIGURES

Figure 2.1 Brace to frame gusset plate connection detailed to accommodate end inelastic rotation (CSA/S16 2009 Commentaries)	13
Figure 2.2 Establishing the gusset plate dimensions (Whitmore, 1952).....	16
Figure 2.3 The 2-storey chevron CBF full-scale specimen tested at the University of Berkeley (Uriz, 2005)	16
Figure 2.4 The HSS Brace response a) brace buckling b) crack propagation c) complete rupture (Uriz, 2005)	18
Figure 2.5 Beam-to-column connection failure (Uriz, 2005)	18
Figure 2.6 Test setup components and boundary conditions (Johnson 2005)	19
Figure 2.7 Single storey single bay test set up photograph (Johnson, 2005).....	21
Figure 2.8 Corner gusset plate connection details: a) tapered $2t_g$ linear clearance, b) rectangular $8t_g$ elliptical clearance.....	21
Figure 2.9 Experimental brace-to-frame connection failure a) Crack at gusset-to-column weld b) Base metal fracture c) Base metal tear near column face (Kotulka, 2007)	23
Figure 2.10 Test specimen TCBF1-HSS at NCREE in Taipei, Taiwan (Clark, 2009).....	24
Figure 2.11 Test specimen TCBF2-HSS at NCREE in Taipei, Taiwan (Lumpkin, 2009).....	25
Figure 2.12 Loading protocol for TCBF2 series (Lumpkin, 2009)	25
Figure 2.13 North brace of Specimen TCBF1-HSS on the 1 st storey a) Brace fracture at plastic hinge b) Initial tear lines c) Partial fracture d) Fracture Opening (Lumpkin, 2009).....	25
Figure 2.14 The response of the LSB joint: a) monotonic test; b) back-bone curve; c) hysteretic behaviour (Pall, 1979)	28

Figure 2.15 LSB joint and its hysteresis response under cyclic test of six case studies (Pall, 1979)	29
Figure 2.16 Friction damper test setup at Polytechnique University Montreal (Tirca et al., 2018)	31
Figure 2.17 Sub-assembly subjected to harmonic displacement cycles (Tirca et al., 2018)	31
Figure 2.18 Yield mechanisms and failure modes (Johnson, 2005)	36
Figure 2.19 HSS brace to gusset plate connection after Hsiao et al., 2013	38
Figure 2.20 Shear lag effects on slotted HSS brace ends (Martinez-Saucedo and Packer, 2009 and CSA/S16 2004)	39
Figure 2.21 Illustration of A_{gv} and A_n areas (Lumpkin, 2009)	40
Figure 2.22 Geometry of gusset plate with $2t_g$ clearance (Lumpkin, 2009)	41
Figure 2.23 The gusset plate dimensions H and W are obtained graphically (after Johnson 2005)	42
Figure 3.1 The gusset plate dimensions HT and WT obtained graphically (according to Kotulka, 2007)	45
Figure 3.2 Finite element model in ANSYS by Hsiao et al. (2012)	47
Figure 3.3 a) Boundary condition of gusset plate model in ABAQUS b) Expected yield line for $2t_g$ linear clearance c) Expected yield line for $8t_g$ elliptical clearance (Lumpkin, 2009)	48
Figure 3.4 Stress distribution for both types of clearance band resulted from ABAQUS models	48
Figure 3.5 Schematic model and the hysteresis response including the bearing stage of a friction-slipping brace (Tirca, 2015)	50
Figure 3.6 The effect of the parameter "exponent n " on the hysteresis response of Bouc-Wen model (Morales, 2012)	52

Figure 4.1 Plan view of typical floor	54
Figure 4.2 Elevation of braced frames: a) MD-CBFs with diagonal braces in E-W direction; b) Chevron MD-CBF in N-S direction	54
Figure 4.3 Members' section of MD-CBF in E-W direction.....	68
Figure 4.4 The OpenSees numerical model built for ¼ of the building	75
Figure 4.5 OpenSees model: a) E-W direction and b) N-S direction	75
Figure 4.6 Discretization of fiber cross-section of (a) HSS brace cross-section and (b) W-shape cross-section for beams and columns	76
Figure 4.7 Consideration of rigid end zones in OpenSees for CBF models (after Hsiao et al., 2012).....	79
Figure 4.8 Design spectrum and 5% damped absolute acceleration spectra of the scaled ground motions for: a) $I_E = 1.0$ and b), $I_E = 1.5$	84
Figure 4.9 Distribution of interstorey drift across the building height: a) $2t_g$ linear gusset plate model, b) $8t_g$ elliptical gusset plate model and c) Mean and Mean+SD comparison between the 2 models.....	87
Figure 4.10 Time-history response of MD-CBF subjected to Loma Prieta ground motion #739 scaled at code level considering $I_E=1.0$	87
Figure 4.11 Residual drift response of MD-CBF with: a) $2t_g$ linear gusset plate model and b) $8t_g$ elliptical gusset plate model. c) Mean and Mean+SD comparison between the 2 models ...	89
Figure 4.12 Distribution of floor acceleration along the MD-CBF height with a) $2t_g$ linear clearance gusset plate model, b) $8t_g$ elliptical clearance gusset plate model and c) Mean and Mean+SD comparison between the 2 models	92
Figure 4.13 Hysteretic loops of braces of MD-CBF (E-W) under GM #787 scaled at code level considering $I_E=1$	94

Figure 4.14 Hysteresis loops of the 3 rd floor braces resulted under: a) #739 Loma Prieta record, b) #1006Northridge record scaled to code level considering $I_E=1$	95
Figure 4.15 Distribution of interstorey drift: a) MD-CBF with $2t_g$ linear gusset plate model, b) MD-CBF with $8t_g$ elliptical gusset plate model and c) Mean and Mean+SD comparison between the 2 models	97
Figure 4.16 Residual drift response: a) MD-CBF with $2t_g$ linear clearance gusset plate model, b) MD-CBF with $8t_g$ elliptical clearance gusset plate model and c) Mean and Mean+SD comparison between the two models.....	99
Figure 4.17 Distribution of floor acceleration: a) MD-CBF with $2t_g$ linear clearance gusset plate model b) MD-CBF with $8t_g$ elliptical clearance gusset plate model and c) Mean and Mean+SD comparison between the 2 models	101
Figure 4.18 Hysteretic loops of HSS braces with $2t_g$ and $8t_g$ gusset plate model and interstorey drift time-history series resulted under GM #1006 scaled at code level considering $I_E=1.0$	102
Figure 4.19 Hysteretic loops of HSS braces with $2t_g$ and $8t_g$ gusset plate model and interstorey drift time-history series resulted under GM #1006 scaled at code level considering $I_E=1.5$	103
Figure 5.1 Elevation view of FS-BF system (E-W direction): a) elevation, slip force and designed member cross-sections and b) Detail of Pall Friction damper.....	106
Figure 5.2 OpenSees model of the experimental test	109
Figure 5.3 Hysteresis response of the OpenSees model versus a generic test response	110
Figure 5.4 Emphasized slip length of friction damper.....	111
Figure 5.5 Calibration of FD model in OpenSees against a generic hysteresis loop resulted from experimental test.....	112

Figure 5.6 Design spectrum and 5% damped absolute acceleration spectra of the scaled ground motions for: a) $I_E = 1.0$ and b), $I_E = 1.5$	114
Figure 5.7 Distribution of interstorey drift over building height for FS-BF (E-W direction): a) BW model b) EPP model	116
Figure 5.8 Time history response of FD-BF: a) scaled accelerogram of GM # 1006 and b) interstorey drift at each floor of hospital building.....	119
Figure 5.9 Time history response of FD-BF: a) scaled accelerogram of GM #739 and b) interstorey drift at each floor of hospital building.....	119
Figure 5.10 Time history response of FD-BF: a) scaled accelerogram of GM #796 and b) interstorey drift at each floor of hospital building.....	120
Figure 5.11 Distribution of residual interstorey drift along the height of FS-BF building (E-W)	122
Figure 5.12 Distribution of floor acceleration along the height of FS-BF building (E-W).....	122
Figure 5.13 Hysteretic loops of friction damper and interstorey drift time-history series resulted under GM #1006 scaled at code level considering $I_E=1.0$	124
Figure 5.14 Distribution of interstorey drift and damper's slip length demand across the building height under GMs scaled to comply with $I_E=1.5$	127
Figure 5.15 Distribution of residual interstorey drift along the height of FS-BF building under GMs scaled to comply with $I_E = 1.5$	128
Figure 5.16 Distribution of floor acceleration along the height of FS-BF building under GMs scaled to comply with $I_E = 1.5$	129
Figure 5.17 Hysteretic loops of friction damper and interstorey drift time-history series resulted under GM #1006 scaled at code level considering $I_E=1.5$ (slip length = 65 mm).....	130

Figure 5.18 Hysteretic loops of friction damper and interstorey drift time-history series resulted under GM #1006 scaled at code level considering $I_E=1.5$ (slip length = 45 mm)..... 131

Figure 5.19 Distribution of interstorey drift along the building height under GMs scaled to comply with $I_E =1$: a) BW & EPPGap material b) $2t_g$ linear model c) Comparison..... 133

Figure 5.20 Distribution of interstorey drift along the building height under GMs scaled to comply with $I_E =1.5$: a) BW & EPPGap material b) $2t_g$ linear model c) Comparison..... 133

LIST OF TABLES

Table 2.1 Importance Categories for buildings according to NBCC 2010.....	7
Table 2.2 Importance factors I_s , I_w and I_E corresponding to building importance category (NBCC 2010).....	7
Table 2.3 Characteristics of the most popular PEDDs (Symans et al., 2008)	27
Table 2.4 Brace-to-frame gusset plate connection design	36
Table 4.1 Dead load on structure	55
Table 4.2 Climatic data for Victoria, B.C., from NBCC 2010	55
Table 4.3 Live load and Snow load on building	56
Table 4.4 Beam sizes of gravity system.....	57
Table 4.5 Gravity column sections for 4-storey hospital building.....	57
Table 4.6 Seismic weight.....	58
Table 4.7 Brace sections of MD-CBF1 & MD-CBF4 corrected as per ETABS analysis (N-S) ..	59
Table 4.8 Brace sections of MD-CBF2 & MD-CBF3 corrected as per ETABS analysis (N-S) ..	60
Table 4.9 Brace sections corrected according to ETABS analysis (MD-CBF5, 6, 7 and 8 in E-W)	60
Table 4.10 Distribution of base shear along the building height according to dynamic distribution	60
Table 4.11 Design summary of tension-compression braces of MD-CBFs in E-W direction	62
Table 4.12 Design summary of inner chevron braces of MD-CBF2 and MD-CBF3 (N-S).....	63

Table 4.13 Design summary of outer chevron braces of MD-CBF1 and MD-CBF4 (N-S).....	63
Table 4.14 Probable resistance of brace members of MD-CBFs in the E-W direction.....	65
Table 4.15a Probable resistance of brace members in the N-S direction: inner MD-CBFs	65
Table 4.16 Beams design of MD-CBFs in E-W direction	65
Table 4.17 Beam design of inner chevron MD-CBF2 and MD-CBF3 in N-S direction	66
Table 4.18 Beam design of outer chevron MD-CBF1 and MD-CBF4 in N-S direction	66
Table 4.19 Exterior Column design of MD-CBFs in E-W direction	67
Table 4.20 Interior Column design of MD-CBFs in E-W direction	67
Table 4.21 Column design of inner chevron MD-CBF2 and MD-CBF3 in N-S direction	67
Table 4.22 Column design of outer chevron MD-CBF1 and MD-CBF4 in N-S direction	68
Table 4.23 The $2t_g$ clearance gusset geometry of brace-to-frame connections of MD-CBF (E-W)	72
Table 4.24 The $8t_g$ elliptical gusset geometry of brace-to-frame connections of MD-CBF (E-W)	72
Table 4.25 The brace-to-frame $2t_g$ linear clearance gusset plate connections calculations (E-W)	73
Table 4.26 The brace-to-frame $8t_g$ elliptical band gusset connections calculations (E-W direction)	73
Table 4.27 Parameters for low-cycle fatigue material of HSS braces with $2t_g$ linear gusset plate model (MD-CBFs in E-W direction).....	77
Table 4.28 Parameters for low-cycle fatigue material of HSS braces with $8t_g$ elliptical gusset plate model (MD-CBF in E-W direction)	77

Table 4.29 Parameters for out-of-plane rotational spring and torsional spring simulating the gusset plate with $2t_g$ model used for HSS braces to frame connections of MD-CBF (E-W)	80
Table 4.30 Parameters for out-of-plane rotational spring and torsional spring simulating the gusset plate with $8t_g$ elliptical model for HSS braces to frame connections of MD-CBF (E-W)	80
Table 4.31 Ground motion selection and characteristics	83
Table 4.32 Ground motion scaling factor to match the design level	84
Table 4.33 Fundamental period T_1 comparison between different software models	85
Table 4.34 Distribution of interstorey drift for MD-CBF with $2t_g$ linear clearance gusset plate model under 10 GMs scaled at code level considering $I_E=1.0$ (E-W)	85
Table 4.35 Distribution of interstorey drift for MD-CBF with $8t_g$ elliptical clearance gusset plate model under 10 GMs scaled at code level considering $I_E=1.0$ (E-W)	86
Table 4.36 Distribution of Mean, Mean+SD and Max. interstorey drift of MD-CBF response (E-W) obtained at code level considering $I_E=1.0$	86
Table 4.37 Distribution of residual drift along the building height for MD-CBF with $2t_g$ linear gusset plate model under 10 GMs scaled at code level considering $I_E=1.0$	88
Table 4.38 Distribution of residual drift along the building height for MD-CBF with $8t_g$ elliptical gusset plate model under 10 GMs scaled at code level considering $I_E=1.0$	88
Table 4.39 Distribution of Mean, Mean+SD and Max residual drifts of MD-CBF (E-W) response along the building height under GMs scaled at code level considering $I_E=1.0$	89
Table 4.40 Distribution of floor acceleration along the height of MD-CBF with $2t_g$ gusset plate model resulted under 10 GMs scaled at code level considering $I_E=1.0$	90
Table 4.41 Distribution of floor acceleration for MD-CBF with $8t_g$ gusset plate model resulted under 10 GMs scaled at code level considering $I_E=1.0$	91

Table 4.42 Distribution of Mean, Mean+SD and Max. floor acceleration of MD-CBF response when subjected to GMs scaled at code level considering $I_E=1.0$	91
Table 4.43 Distribution of interstorey drift recorded for MD-CBF (E-W) with $2t_g$ linear gusset plate model under 10 GMs scaled at code level considering $I_E=1.5$	96
Table 4.44 Distribution of interstorey drift recorded for MD-CBF (E-W) with $8t_g$ elliptical gusset plate model under 10GMs scaled at code level considering $I_E=1.5$	96
Table 4.45 Mean, Mean+SD and Max interstorey drift of MD-CBF response at code level considering $I_E=1.5$	96
Table 4.46 Distribution of residual drift of MD-CBF with $2t_g$ linear gusset plate model under 10 GMs scaled at code level considering $I_E =1.5$	98
Table 4.47 Distribution of residual drift of MD-CBF with $8t_g$ elliptical gusset plate model under 10 GMs scaled at code level considering $I_E =1.5$	98
Table 4.48 Mean, Mean+SD and Max. residual drifts response under GMs scaled at code level considering $I_E=1.5$	98
Table 4.49 Distribution of floor acceleration along the MD-CBF building height for the case with $2t_g$ gusset plate model resulted under 10 GMs scaled at code level considering $I_E=1.5$	99
Table4.50 Distribution of floor acceleration of MD-CBF building height with $8t_g$ gusset plate model resulted under 10 GMs scaled at code level considering $I_E=1.5$	100
Table 4.51 Distribution of Mean, Mean+SD and Max floor acceleration of MD-CBF response when subjected to GMs scaled at code level considering $I_E=1.5$	100
Table 5.1 Characteristics of FS-BF system (E-W direction) resulted from the equivalent static force procedure	107
Table 5.2 First mode period of studied structural systems	113
Table 5.3 Selected crustal ground motions and scaling factor.....	114

Table 5.4 Distribution of interstorey drifts of FS-BF using <i>BoucWen</i> material for FDs under scaled ground motions.....	115
Table 5.5 Distribution of interstorey drifts of FS-BF using EPP model for FDs under scaled ground motions.....	115
Table 5.6 Damper displacement demand simulated with <i>BoucWen</i> material under GMs.....	117
Table 5.7 Possible slip length resulted underground motions scaled to comply with $I_E=1$	117
Table 5.8 Proposed slip length for friction dampers associated with $I_E=1$	118
Table 5.9 Residual interstorey drift of FS-BF with FDs simulated with <i>BoucWen</i> material at $I_E=1$	121
Table 5.10 Distribution of floor acceleration of FS-BF equipped with friction dampers simulated with <i>BoucWen</i> material at $I_E=1$ (E-W direction).....	123
Table 5.11 Distribution of interstorey drift at code level with $I_E=1.5$ when braces are simulated using <i>BoucWen</i> material without Slip Lock simulation	125
Table 5.12 Distribution of Mean, Mean+SD and Max. interstorey drift response at code level considering $I_E=1.5$	125
Table 5.13 Distribution of damper slip length demand at code level with $I_E=1.5$ for FDs simulated with <i>BoucWen</i> material without SL simulation	126
Table 5.14 Proposed slip length for friction dampers associated with $I_E=1.5$	126
Table 5.15 Distribution of residual interstorey drift of FS-BF with FDs simulated with <i>BoucWen</i> material resulted under GMs scaled to comply with $I_E=1.5$	127
Table 5.16 Distribution of floor acceleration along the height of FS-BF building equipped with FDs simulated with <i>BoucWen</i> material under GMs scaled to comply with $I_E=1.5$ (E-W).	128
Table 5.17 Slip force and slip length of FS-BF hospital building	129

Table 5.18 Comparison of interstorey drift distribution along the height of FS-BF and MD-CBF buildings under GMs scaled to match the design spectrum associated to $I_E=1$	132
Table 5.19 Comparison of interstorey drift distribution along the height of FS-BF and MD-CBF buildings under GMs scaled to match the design spectrum associated to $I_E=1.5$	132
Table 5.20 Comparison of residual interstorey drift distribution along the height of FS-BF and MD-CBF buildings under GMs scaled to match the design spectrum associated to $I_E=1$..	134
Table 5.21 Comparison of residual interstorey drift distribution along the height of FS-BF and MD-CBF buildings under GMs scaled to match the design spectrum associated to $I_E=1.5$	134
Table 5.22 Comparison of floor acceleration distribution along the height of FD-BF and MD-CBF buildings under GMs scaled to match the design spectrum associated to $I_E=1.0$	136
Table 5.23 Comparison of floor acceleration distribution along the height of FD-BF and MD-CBF buildings under GMs scaled to match the design spectrum associated to $I_E=1.5$	136
Table 5.24 Distribution of peak interstorey drifts of FS-BF _{CC} under GMs scaled for at $I_E=1$	138
Table 5.25 Distribution of residual interstorey drifts of FS-BF _{CC} under GMs scaled for $I_E=1$..	139
Table 5.26 Distribution of floor accelerations of FS-BF _{CC} under GMs scaled for $I_E=1$	140

LIST OF SYMBOLS

A_g	gross area
A_{gp}	gross area of gusset plate
A_{gv}	gross area in shear
A_m	shear area of effective fusion face
A_{ne}	net area
A_w	area of effective weld throat
B_x	ratio at level x used to determine torsional sensitivity
BW	Bouc-Wen material
C_a	shape factor
C_b	basic roof snow load factor
C_e	Euler buckling load
C_f	compressive force in a member or component under factored load
C_r	factored compressive resistance of a member or component
C_u	probable compressive resistance of a bracing member
C'_u	probable post-buckling compressive resistance of a bracing member
C_w	wind exposure factor
CBF	centrically braced frame
CM	centre of mass
CR	centre of rigidity
D_s	smaller plan dimension
D_w	fillet weld leg width
e	eccentricity due to location of the centre of mass and the center of rigidity
e_x	design eccentricity
E	elastic modulus of steel (200 GPa assumed)
EPP	elastic perfectly plastic
$ESFP$	equivalent static force procedure
F_{slip}	slip force of friction damper
F_t	portion of V concentrated at the top of the structure
F_u	ultimate stress
F_y	yield stress

FD	friction dampers
$FS-BF$	friction sliding braced frame
g	acceleration of gravity
G	shear modulus of steel material (77 GPa assumed)
GP	gusset plate
GM	ground motion
h_n	total height of the building
h_s	interstorey height
I_E	earthquake importance factor of the structure
I_S	snow importance factor of the structure
I_W	wind importance factor of the structure
I_x, I_y	moment of inertia about x-x, y-y
J	torsion constant
K	effective length factor
KL	effective length
l, L	length of a member or component
L_w	welding length
$NBCC$	national building code of Canada
m	fatigue ductility exponent
M_p	plastic moment taken as ZF_y
M_r	factored moment resistance of a member or component
M_v	higher mode factor
$MD-CBF$	moderate-ductile concentrically braced frame
$MRSA$	modal response spectrum analysis
PGA	peak ground acceleration
PGV	peak ground velocity
r	radius of gyration
R_d	ductility related force modification factor
R_o	overstrength related force modification factor
r_x, r_y	radius of gyration about x-x, y-y axis
S_r	associated rain load in kPa with a 1-in-50 probability of exceedance per year

S_s	ground snow load in kPa with a 1-in-50 probability of exceedance per year
SFRS	seismic force resisting system
$S_a(T_a)$	design spectral response acceleration at the fundamental period of vibration
$S_a(T_1, 5\%)$	5% damped spectral acceleration at the structure's first mode period
S_a	pseudo acceleration
SD	standard deviation
T_a	fundamental period of the structure
T_f	tensile force in a member or component under factored loads
T_r	factored tensile resistance of a member or component
T_u	probable tensile resistance of bracing members
t	thickness of a member or component
t_g, t_{gp}	thickness of the gusset plate
U	factor account for shear lag effect
UHS	uniform hazard spectrum
U_2	amplification factor for P- Δ effects
V	lateral seismic design force at the base of the structure (base shear)
V_{dyn}	dynamic base shear
V_r	factored shear resistance of the fillet weld
w	width of the brace
W	seismic weight of the structure
W_w	Whitmore width of the gusset plate
WP	working point
X_u	electrode ultimate tensile strength
Z	plastic section modulus
ε_0	fatigue ductility coefficient
λ	slenderness ratio
ϕ	resistance factor

Chapter 1

INTRODUCTION

1.1 General / Background

Natural disasters are often unpredictable and vulnerable cities are at risk. In high seismic zones, earthquakes may cause severe damages to the building stock. When disaster strikes, repairing the infrastructure lifeline network is the key to restoring the social organization of communities (World Bank, 2008). Meanwhile, communities need to be prepared for such disasters and all leadership entities (municipal, provincial, federal) should assure the safety and security of the public by maintaining its public facilities operational throughout the event and its aftermath. All building structures of normal importance category, designed according to the modern codes and standards, are expected to withstand seismic loading while undergoing moderate to severe damage. However, hospital buildings, categorized as post-disaster importance category, should exhibit light damage and remain functional (e.g. non-structural components such as cladding, partition walls, ceilings should exhibit no to light damage and plumbing, electrical, heating system, elevators, etc. should remain operational).

In regions where earthquakes of higher than expected magnitudes may occur, there is a need to investigate the behaviour of existing post-disaster buildings to identify if the seismic details are adequate. Buildings in British Columbia (BC) are subjected to crustal earthquakes and to subduction earthquakes caused by the Cascadia subduction fault.

In North America, the steel concentrically braced frame (CBF) is a very popular structural system due to its high stiffness, moderate ductility, and ease to construct. However, past studies (Tremblay, 2001, Kotulka, 2007) have revealed the sensitivity of brace-to-frame connections during the braces inelastic response, when these yield in tension and buckle in compression. Recently, analytical and experimental studies on brace-to-frame gusset plate connections showed that current design requirements may lead to stiffer and stronger gusset plates, which possess limited deformation capacity, and in turn, may drive the CBF system to premature failure. Thus,

the yielding mechanisms and the failure hierarchy of the system's components are strongly linked to one another and need to be considered simultaneously (Roeder et al., 2011 and 2013). Accordingly, the fracture of braces caused by low-cycle fatigue should be the primary failure mechanism and their gusset plate failure to be the second. Meanwhile, the brace-gusset plate system should be detailed to allow the out-of-plane deflection of braces under earthquake shaking. To assure the collapse prevention performance of CBFs, changes in the gusset plate geometry that allow braces to fail at larger interstorey drift are recommended. To overcome this drawback, researchers proposed to modify the clearance geometry of brace-to-frame gusset plate connection considering that a smaller and thinner gusset plate increases the ductility of HSS braces. Hence, a gusset plate with $8t_g$ elliptical clearance band was proposed instead of the $2t_g$ linear band recommended by the current standard, where t_g is the thickness of the gusset plate. Allowing gusset plates to yield, the performance of CBF braces improves. To provide adequate brace-to-frame gusset plate connections, the CSA/S16 standard requires that these connections to respond in the elastic range when sustaining forces resulted from the probable tensile and probable buckling strength of brace members.

Applying a ductile seismic design procedure and capacity design method according to the current code and standard, the energy dissipated through brace yielding and buckling is exhibited, while the adjacent CBF members respond in the elastic range. It is known that HSS braces buckle out-of-plane and the attached gusset must possess larger tensile and compression strength than that of the brace members. In order to allow HSS braces to bend out-of-plane, the standard provisions complying with gusset plate design detail with a $2t_g$ linear clearance model is applied. Brace fracture at its mid-span length is the desired failure mechanism occurring after plastic hinges are developed in the $2t_g$ area of gusset plates. Thus, the thickness of the gusset plate and its geometry strongly influence the brace yielding mechanism.

Several researchers have conducted experimental tests to emphasize on the behaviour of brace-to-frame gusset plate connections (Whitmore, 1952, Astaneh-Asl, 1998). However, these tests were conducted without considering the complete frame action and the brace deformation demand when they experienced yielding in tension and buckling/ post-buckling in compression. Hence, in practice, it was shown that the linear clearance models have limited inelastic cyclic deformation, which resulted in fewer numbers of cycles triggered by braces' response.

As the number of components assembled in shop keeps increasing, special attention should be given to connections of a brace member with attached Passive Energy Dissipating Device (PEDD). Among the PEDDs, friction dampers rely on friction between specially coated plates to dissipate the input energy. These devices are usually installed in-line with braces. However, the current design proceedings do not provide design guidelines for braces equipped with friction dampers.

1.2 Objectives and Scope

The aim of this research project is three-fold:

- To investigate the nonlinear behaviour of multi-storey hospital building braced with moderately ductile concentrically braced frame system (CBF) with braces to frame gusset plate connections detailed with $8t_g$ elliptical clearance band against the $2t_g$ linear clearance.
- To develop an accurate numerical model for braces equipped with friction dampers using the OpenSees software.
- To refine the design method for multi-storey braced frame building equipped with friction dampers installed in-line with diagonal braces (FS-BF) and to identify the potential failure mode.

Through this analytical research, the overall understanding of nonlinear behaviour of CBFs with different seismic detailing and CBFs equipped with friction dampers employed in multi-storey post-disaster buildings is improved. The outcomes of this research can be used for design regulations and as input for further experimental tests.

1.3 Description of methodology

For attaining the aforementioned objectives, the following steps were carried out:

- Results from analytical and experimental tests were selected to design brace to frame gusset plate connections detailed with $8t_g$ elliptical clearance versus $2t_g$ linear clearance band subjected to monotonic and cyclic loadings. Based on these results, an analytical brace model was developed in OpenSees to study the influence of time-history loading on braces response. All selected braces are tubular, compact cross-sections, HSS, belonging to Class 1.
- To bring refinement in the design of multi-storey CBF equipped with friction-sliding braces (FS-BF). Data from experimental tests was analysed and a numerical model was proposed.
- To improve the overall understanding of the multi-storey moderately ductile CBF (MD-CBF) system equipped with advanced brace-to-frame connection detailing and that of the FS-BF system. A case study consisted of a 4-storey hospital building located on Site Class C (firm soil) in Victoria, British Columbia, was considered. Suitable ground motions were selected and scaled to match the design spectrum for Victoria according to NBCC 2010. The OpenSees models were developed for the 4-storey hospital building equipped with braced frames with three different seismic detailing: (i) MD-CBF with brace-to-frame gusset plate connections detailed with $2t_g$, (ii) MD-CBF with brace-to-frame gusset plate connections detailed with $8t_g$ elliptical clearance, and (iii) friction sliding braces for the FS-BF system. The obtained results are discussed in terms of interstorey drift, residual interstorey drift and floor acceleration.

1.4 Thesis organization

This thesis is organised in six chapters. The first chapter contains a brief introduction, the scope and thesis objectives, the methodology as well as the thesis organization. The second chapter summarises the literature review related to past studies presenting design principles and behavioural characteristics of concentrically braced frame systems with $2t_g$ linear clearance, $8t_g$ elliptical clearance and friction damper devices. Chapter 3 is related to brace-to-frame gusset plate connections design and guidelines. Experimental tests conducted on gusset plate detailed with $2t_g$ linear clearance and $8t_g$ elliptical clearance from the literature are investigated in order to calibrate the OpenSees model and replicate the behaviour of these connections. Using an existing full-scale experimental test conducted on an HSS brace equipped with Pall friction

damper, the OpenSees model was calibrated. The behaviour stages of a friction damper such as: slip-stick, sliding and bearing are discussed. In Chapter 4, a case study of a 4-storey hospital building located in Victoria, B.C is presented. The seismic force resisting system of the 4-storey building consists of MD-CBFs equipped with brace-to-frame gusset plate connections detailed with both clearance bands. Similarly, in Chapter 5, the nonlinear behaviour of the same 4-storey hospital building braced with the FS-BF system is investigated. Conclusions and recommendations for the future work are presented in Chapter 6.

Chapter 2

LITERATURE REVIEW

Seismic design provisions are considered in order to assure the safety of inhabitants and protect the value of their properties and their contents. This section contains existing guidelines related to the seismic design of post-disaster buildings. A brief summary of relevant past experiments focusing on the effect of brace-to-frame connection in CBF systems is also presented. Then, a literature review on passive energy dissipation devices, known as Pall friction dampers, is conducted.

2.1 Importance Categories for Buildings

2.1.1 Importance Category and the Limit States Design according to NBCC 2010

The National Building Code of Canada 2010 (NBCC) sets out technical provisions for the design and construction of new structures. For the purpose of computing all loads, an Importance Category must be assigned to buildings based on its use and occupancy as provided in Table 2.1. Thus, to provide an adequate safety level, schools, community centres, hospitals, power plants, emergency response facilities and other buildings containing hazardous materials are designed using increased importance factors, which determine how much the environmental loads for that structures need to be increased from a base reference design load. The snow, wind, and earthquake loads are known as environmental loads. Table 2.2 summarizes different importance factors used to scale up or down the environmental loads in function of the building's importance category. The importance factors for snow loads, I_s , wind loads, I_w , and earthquake loads I_E are different for ultimate limit state design (ULS) and for the serviceability limit state design (SLS).

Table 2.1 Importance Categories for buildings according to NBCC 2010

Use and Occupancy	Importance Category
Buildings that represent a low direct or indirect hazard to human life in the event of failure, including: <ul style="list-style-type: none"> • low human-occupancy buildings, where it can be shown that collapse is not likely to cause injury or other serious consequences • minor storage buildings 	Low
All buildings except those listed in Importance Categories Low, High and Post-disaster	Normal
Buildings that are likely to be used as post-disaster shelters, including buildings whose primary use is: <ul style="list-style-type: none"> • as an elementary, middle or secondary school • as a community centre Manufacturing and storage facilities containing toxic, explosive or other hazardous substances in sufficient quantities to be dangerous to the public if released	High
Post-disaster buildings are buildings that are essential to the provision of services in the event of a disaster, and include: <ul style="list-style-type: none"> • hospitals, emergency treatment facilities and blood banks • telephone exchanges • power generating station and electrical substations • control centres for air, land and marine transportation • public water treatment and storage facilities, and pumping stations • sewage treatment facilities and buildings having critical national defence functions • buildings of the following types, unless exempted from this designation by the authority: <ul style="list-style-type: none"> • emergency response facilities • fire, rescue and police stations, and housing for vehicles used for such purposes • communications facilities, including radio and television stations 	Post-disaster

Table 2.2 Importance factors I_s , I_w and I_E corresponding to building importance category (NBCC 2010)

Importance Category	Snow, I_s		Wind, I_w		Earthquake, I_E
	ULS	SLS	ULS	SLS	ULS
Low	0.8	0.9	0.8	0.75	0.8
Normal	1	0.9	1	0.75	1
High	1.15	0.9	1.15	0.75	1.3
Post-disaster	1.25	0.9	1.25	0.75	1.5

According to NBCC 2010, the ULS is concerned about safety and verifies that the load-carrying capacity of the system is not exceeded. The SLS may limit the intended use and occupancy of the buildings due to deflection limits, vibration, permanent deformation (e.g. residual interstorey drift) and local structural damage. According to Clause 4.1.3.5 of NBCC 2010, the intended use

of a building and the amount of damage that non-structural and structural members can withstand should be taken into consideration when proportioning structural members to avoid serviceability problems related to deflection. Thus, the building's lateral deflection under wind load and earthquake load must be verified to be within the code limits with respect to the building's importance category.

2.1.2 Snow Load and Wind Load Calculation According to NBCC 2010

According to Clause 4.1.6 of NBCC 2010, the specified snow load, S , due to snow and associated rain accumulation is calculated with Equation (2.1), where I_s is the importance factor for snow load, S_s is the 1-in-50 year ground snow load, C_b is the basic roof snow load factor, C_w is the wind exposure factor, C_s is the slope factor, C_a is the shape factor and S_r is the 1-in-50 year associated rain load.

$$S = I_s[S_s(C_b C_w C_s C_a) + S_r] \quad (2.1)$$

According to Clause 4.1.7 of NBCC 2010, the static procedure for wind load calculation is applied to buildings that are lower than 60m in height with a natural frequency greater than 1 Hz. In this light, the specified external pressure and suction, p , due to the wind is calculated using Eq.(2.2).

$$p = I_w q C_e C_g C_p \quad (2.2)$$

Herein, I_w is the importance factor for wind load, q is the reference velocity pressure, while C_e , C_g , and C_p are the exposure, gust effect, and pressure coefficient factor, respectively. Buildings that are taller than 60m, with the height-to-width ratios higher than 4 or with a natural frequency lower than 1 Hz are considered to be dynamically sensitive and a dynamic procedure shall be employed.

Buildings where $H/D_s < 1.0$ and $H \leq 20$ m are considered low-rise and those where $H/D_s \geq 1.0$ or $H > 20$ m are considered high-rise. Herein, H is the building height and D_s is the smaller plan

dimension. Static procedure for wind calculation is different for low-rise and high-rise buildings. In addition, partial loading cases must be conducted to examine the most severe torsional effects anticipated from wind loading.

The lateral deflection of buildings due to service wind and gravity loads shall be checked to ensure that structural and non-structural components will not be damaged. The total drift per storey under service wind and gravity loads shall not exceed 1/500 of the storey height unless other drift limits are specified in the design standard.

2.1.3 Earthquake Load Calculation According to NBCC 2010

The equation for estimating the fundamental period of the building, T_a , depends on the selected type of Seismic Force Resisting System (SFRS). For steel braced frames, the expression used to calculate the fundamental period T_a is given below. Based on this equation, the period T_a is only dependent on the total building height, h_n , hence the period yields the same value regardless of the direction under consideration. In this light, dynamic analysis can be used to determine the fundamental period of vibration in each principal direction of the building, however, the resulted period should not exceed $2T_a$.

$$T_a = 0.025h_n \quad (2.3)$$

The Uniform Hazard Spectrum (UHS) approach, based on 2% probability of exceedance in 50 years corresponding to 2475 years return period, was first introduced in NBCC 2005. For Site Class C, ($F_a=F_v=1$) the design spectrum (DS) is the same with the UHS. Using the equivalent static force procedure, the lateral design base shear, V , is calculated with Equation (2.4). However, V shall not be less than the minimum base shear as per Equation (2.5) and need not to be greater than the maximum base shear calculated using Equation (2.6) for any SFRS with $R_d \geq 1.5$.

$$V = S(T_a) \frac{M_v I_E W}{R_d R_o} \quad (2.4)$$

$$V_{min} = S(2.0)M_V I_E W / R_d R_o \quad (2.5)$$

$$V_{max} = \frac{2 S(0.2) I_E W}{3 (R_d R_o)} \quad (2.6)$$

where the 5% damped spectrum response acceleration $S(T_d)$ is given at specific periods of 0.2, 0.5, 1.0 and 2.0 s for each location. This spectrum response acceleration $S(T_d)$ is then amplified with factors that take into account the higher mode effects on base shear M_v and the building's importance category I_E . In the above equations, W is the building seismic weight including 25% snow load. The elastic base shear is reduced with the ductility-related force modification factor, R_d and the overstrength-related force modification factor, R_o . The typical values for R_d and R_o for each SFRS are given in the NBCC. These factors were incorporated to provide an economical design. Thus, buildings are designed to absorb and dissipate energy through the ductility capacity of the structure during earthquakes. Nonetheless, when higher values of R_d are selected during preliminary design, the building is more flexible and significant detailing of connections is required to provide the development of such high ductility.

According to NBCC, additional considerations are required for post-disaster buildings. In cases where $I_E F_V S_a(1.0) \geq 0.35$, the post-disaster building shall not have any irregularities conforming to Type 1 (vertical stiffness irregularity), Type 3 (vertical geometric irregularity), Type 4 (in-plane discontinuity in vertical seismic force resisting system), Type 5 (out-of-plane offsets), Type 6 (weak storey) and Type 7 (torsional sensitivity). Furthermore, the building must have a SFRS with $R_d \geq 2.0$ and have no storey with a lateral stiffness that is less than that of the storey above it.

Based on the maximum allowable lateral deflection limit set by NBCC, the largest interstorey drift at any level shall be limited to $0.01h_s$, $0.02h_s$ and $0.025h_s$ for post-disaster buildings, high importance category buildings and all other buildings respectively.

2.2 Seismic Design Requirements for Concentrically Braced Frames and Seismic Detailing

Concentrically braced frames (CBFs) provide the stiffness and strength needed to achieve operational performance objectives, which are primarily defined by the performance of non-structural elements (Hsiao, 2012). Proper detailing of brace-to-frame connections is required in order to allow braces to exhibit inelastic excursions during extreme events. Moreover, the surrounding frame members must remain elastic to avoid frame instability. In this matter, CBF systems are more likely to have a ductile mode of behaviour prior to brace fracture. The structure must tolerate these large inelastic demands without undergoing collapse or loss of life. Current design requirements and recent experimental findings of CBFs are presented hereafter.

2.2.1 Seismic Design of Concentrically Braced Frames according to CSA S16 2009 standard

The rules and requirements for the design of steel CBFs, are provided in the Canadian Standard Association CSA/S16. To establish a strength hierarchy along the load path, the seismic design provisions are based on the capacity design approach, which implies that the inelastic action occurs in members of the seismic force resisting system that are detailed for such action. Thus, specific elements or connections are designed to dissipate energy. These dissipative zones are detailed to suppress undesirable premature failure modes, such as local buckling and member instability, while the surrounding structural members are made sufficiently strong to allow for this energy dissipation while maintaining the structural integrity (Bruneau et al., 1998). For CBFs, the brace is expected to dissipate energy through its inelastic behavior during a severe seismic event. Thus, the surrounding structural elements such as beams, columns and brace-to-frame connections should be designed to resist the probable resistance of braces in order to behave elastically during earthquake events. As per CSA/S16 2009, for tension-compression braces, two loading scenarios are considered in design: (i) prior to reaching brace buckling, the brace is expected to develop its probable tensile and compressive resistance, T_u and C_u , respectively and (ii) after the occurrence of brace buckling, the brace member possesses only the probable post-buckling compression resistance C_u' and in the tension side, it possesses the probable tensile strength T_u . However, for a building of 4-storey height and less, the probable tensile strength can be reduced to $0.6T_u$.

According to CSA S16.1-09, the tensile resistance, T_r and the probable tensile resistance, T_u of a brace member subjected to axial tension force respectively are calculated using the following Equations:

$$T_r = \phi A_g F_y \quad (2.7)$$

$$T_u = A_g R_y F_y \quad (2.8)$$

Herein, A_g is the gross cross-sectional area of the brace member, ϕ is the resistance factor equal to 0.9, while the value of R_y can be taken as 1.1 for W-shape sections and the probable yield strength, $R_y F_y$, should not be taken less than 385 MPa. However, the probable yield stress $R_y F_y$ shall not be less than 460 MPa for HSS sections.

The axial compressive resistance C_r , the probable compression resistance, C_u and the probable post-buckling compressive resistance, C_u' , of brace members shall be calculated as:

$$C_r = \phi A_g F_y (1 + \lambda^{2n})^{-1/n} \text{ where } \lambda = \frac{KL}{r} \sqrt{\frac{F_y}{\pi^2 E}} \quad (2.9)$$

$$C_u = \min\{1.2C_r R_y / \phi, A_g R_y F_y\} \text{ where } \phi = 0.9 \quad (2.10)$$

$$C_u' = \min\{C_r R_y / \phi, 0.2A_g R_y F_y\} \quad (2.11)$$

Herein, A_g is the cross-sectional area of the brace, $n=1.34$ for hollow structural sections HSS manufactured in accordance with CSA G40.20, Class C (cold formed non-stress relieved). In the above equations, ϕ is a resistance factor taken as 0.9 unless otherwise specified. The brace member is considered pinned connected to the frame, which means $k=1$. However, kL in Eq. (2.9) is the effective length of the brace, marked L_H in Fig. 2.1. For simplification, L_H may be estimated at $0.9 L_{C-C}$.

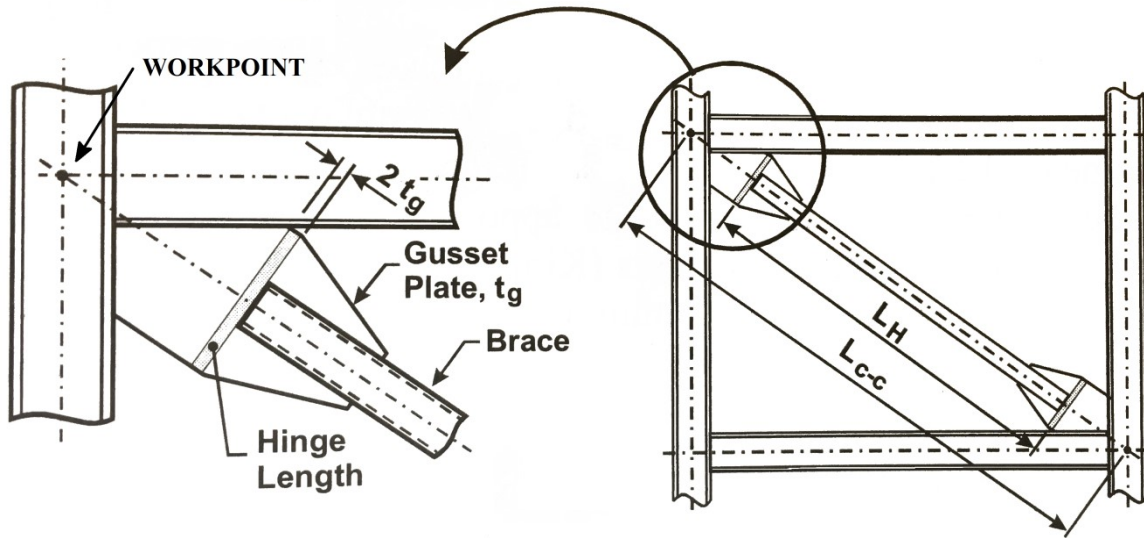


Figure 2.1 Brace to frame gusset plate connection detailed to accommodate end inelastic rotation (CSA/S16 2009 Commentaries)

The MD-CBFs are able to dissipate a moderate amount of energy through yielding of bracing members and are designed with $R_d = 3.0$ and $R_o = 1.3$. The MD-CBFs with tension-compression braces shall not exceed 40 m in height when designed in areas where the specified short-period acceleration ratio $I_E F_a S_a(0.2) \geq 0.35$ or $I_E F_v S_a(1.0) > 0.3$. The slenderness ratio, KL/r , of tension-compression bracing members shall not exceed 200. The effects of translational and rotational restraints at the brace ends should be accounted for in the calculation of KL . When $KL/r \leq 100$, for rectangular and square HSS, the width-to-thickness ratio computed as $[(b-4t)/t]$ should be $\leq 330/F_y^{0.5}$ where b is the HSS section dimension and t is its wall thickness.

The factored resistance of brace connections shall exceed both T_u and C_u values that may be developed by the brace section. Buckling of braces induces a rotational demand at the brace-gusset plate connections; hence, the gusset plate inserted in the slotted HSS brace should be detailed to possess sufficient flexural resistance to prevent any premature fracture. According to Astaneh and Goel (1985) and the CSA/S16 commentaries, in the case of an HSS brace attached to a single gusset plate, a ductile rotational behaviour must be allowed for in the gusset plate in order to accommodate the out of plane buckling of the HSS brace. According to Fig. 2.1, this can be achieved by providing a clear band equal to two times the thickness of the gusset plate, $2t_g$, at

the end of the brace member. Details on the brace-to-frame connection design are further discussed in Chapter 3.

2.2.2 Learning from existing tests conducted on the brace and gusset plate systems of CBFs

To improve the inelastic response of CBF braces, an adequate seismic detailing of braces to frame connections is required. A summary of previous experimental tests conducted to understand the importance of brace to frame connection detail on the inelastic behaviour of braces is presented below.

Several researchers (e.g., Wakabayashi 1973, Kahn and Hanson 1976, Astaneh et al. 1982, Aslani and Goel 1989) have studied the behaviour of brace-to-gusset plate connection systems subjected to monotonic and cyclic axial deformations loading. They have considered various design parameters such as the slenderness ratio, width-to-thickness ratio, gusset plate clearances, bolted vs. welded connection and in-plane vs. out-of-plane buckling response. The relevant conclusions that were reached in these studies are briefly summarized below.

Astaneh et al. (1985) conducted tests on double angle bracing specimens with tapered gusset plates at the University of Michigan. At that time, there were no seismic detailing specifications to predict the gusset plate deformation under a severe earthquake event. New modifications in the detailing of gusset plates were proposed to improve the energy dissipation capacity of braces and the structure's ductility.

The study led by Astaneh et al. (1985) provided several key findings, which are listed below:

1. The effective slenderness ratio and width-to-thickness ratio are the most influential parameters in determining the hysteretic behavior of bracing members.
2. The maximum compressive strength of brace decreases with the increasing number of cycles, hence strength deterioration was observed.
3. The development of buckling force in brace members may differ in the case of bolted gusset plate connections compared to welded connections due to the slippage of the bolts in the connections.

4. Bolt slippage can cause a pinched hysteresis loop, which decreases the energy dissipation capacity of the system.
5. A $2t_g$ linear clearance within the gusset plate was proposed to be provided at the end of the brace.

When brace buckles out-of-plane, the end rotation of brace causes significant rotation and bending demands on the gusset plates. The $2t_g$ clearance intends to accommodate the out-of-plane buckling of the brace by allowing the gusset plates to yield and bend in this $2t_g$ clearance band where plastic hinges will form.

Hardash and Bjorhovde (1985) confirmed that the Whitmore's method (1952) was appropriate to estimate the tensile stress and the tensile fracture capacity of the gusset plates. Then, the compressive capacity and the buckling strength of the gusset plates were investigated by Thornton in 1984. Based on the procedures proposed by Whitmore and Thornton, the tensile and compressive capacities of gusset plates was estimated. Then, several experimental studies were conducted to assess the response of gusset plate with $2t_g$ clearance subjected to monotonic and cyclic loading (Rabinovitch and Cheng 1993, Brown 1988, Grondin et al. 2000). From these studies, the following key conclusions were noted:

1. The design philosophy of weak gusset plate-strong brace combination resulted in a larger energy dissipation than that developed when the strong gusset plate-weak brace approach was employed.
2. The Whitmore method provided a conservative estimate of gusset plate capacity for compact specimens and overestimated the strength of slender brace connections.

To calculate the ultimate capacity of gusset plates, a schematic connection detail is presented in Figure 2.2. Researchers have assumed that the axial load spreads out at a 30-degree angle from the brace – gusset plate intersection line to the brace's end (see the grey brace segment). By joining the 30° lines at the end of the brace, the Whitmore's width, W_w parameter was revealed. Using this Whitmore's width and the effective length of the gusset, the compressive and tensile capacity of the gusset plate is calculated. The detailed calculation is presented in a later section.

To bring knowledge on the seismic response of chevron CBFs, Uriz and Mahin (2004) conducted at the University of California, Berkeley, a series of 8 tests consisting of HSS brace sections and gusset plate connections. Experimental testing on a full-scale two-storey CBF system with HSS brace sections was then carried out by Uriz (2005). All of the tapered gusset plates in this test used the $2t_g$ offset, as seen in Figure 2.3.

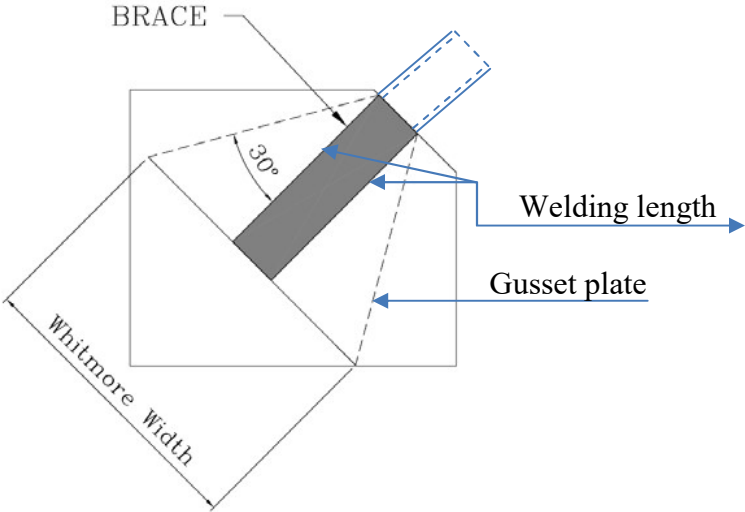


Figure 2.2 Establishing the gusset plate dimensions (Whitmore, 1952)

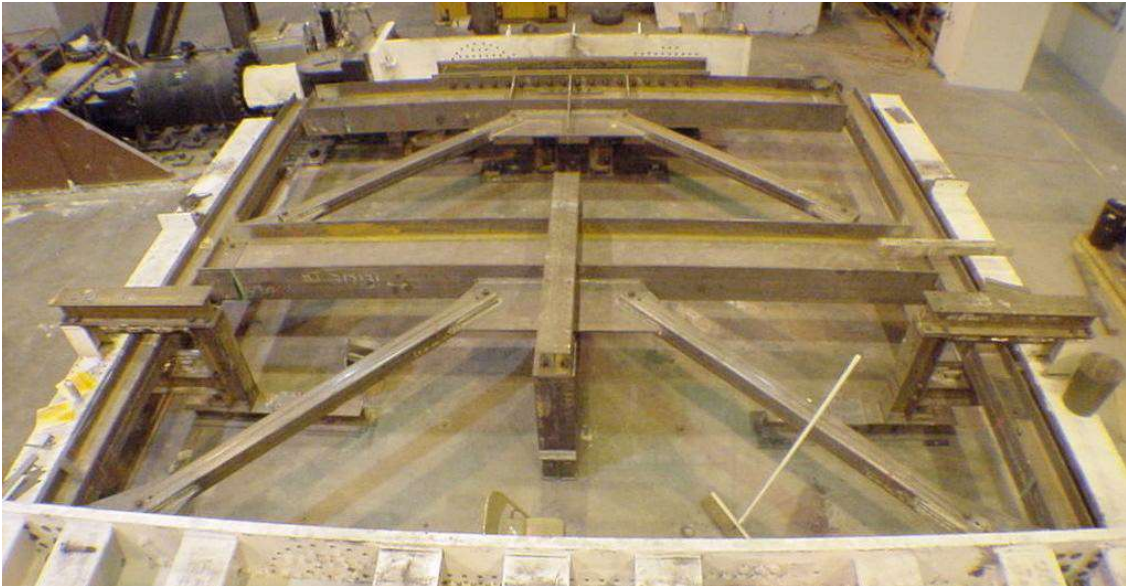


Figure 2.3 The 2-storey chevron CBF full-scale specimen tested at the University of Berkeley (Uriz, 2005)

The frame (beams and columns) was not sized for reuse, instead, it was designed as per the 1997 AISC seismic code, and so the beams were very large in order to account for the unbalanced vertical load that is associated with braces in a chevron configuration. The objectives of the tests were to improve the understanding of the behavior of full CBF systems, improve computer models and assess the design guidelines available at that time. A brief summary of the findings is listed below.

1. The framing elements experienced considerable damage at large drift ranges. This implies that the behavior of braced frames is highly system-dependent; meaning the framing element contribution must be included in the system performance.
2. After brace reached fracture, the lateral resistance of the structure is provided by the frame action of beams and columns. This can result in as much as a 30% loss of the initial pre-fracture capacity.
3. Uriz (2005) reported that when braces develop a slight amount of buckling, the distribution of lateral drift was nearly identical for the upper and lower floor. However, once the bottom floor braces were damaged at their mid-span as shown in Figure 2.4a, the inelastic behaviour and damage were concentrated on that specific floor. Due to the reduced load capacity of buckled braces, the lateral stiffness of the bottom floor was decreased, resulting in a soft-storey like response. This led to the complete fracture of the braces (Figure 2.4c) with the failure of the lower-level beam-to-column connections occurring soon after. Braced frame systems are more susceptible to soft storey effects than other SFRSs.
4. The beam was much larger than the column, hence the column received more critical damage in the form of local buckling and fracture on the flange facing the beam-to-column connection as shown in Figure 2.5. As illustrated in Figure 2.5 no stiffeners were provided in the W-shape column at the line of W-shape beam flanges.
5. Buckling Restrained Braces (BRB) were also installed in the same setup on the first floor while traditional CBFs were kept on the upper floor, however, BRB's are beyond the scope of this report.

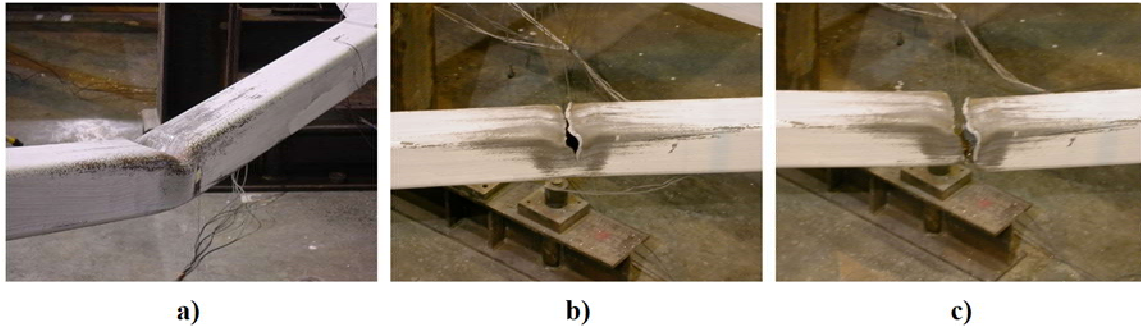


Figure 2.4 The HSS Brace response a) brace buckling b) crack propagation c) complete rupture (Uriz, 2005)

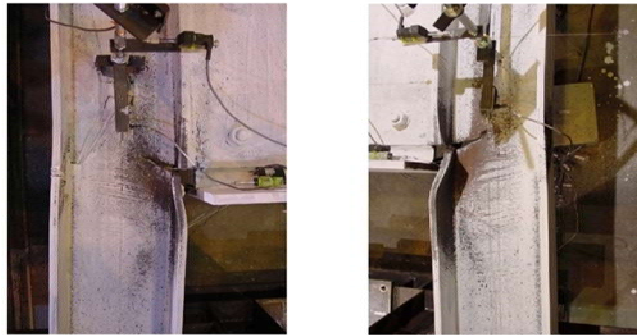


Figure 2.5 Beam-to-column connection failure (Uriz, 2005)

2.2.3 Learning on the behaviour of CBF with elliptical clearance gusset plate connection

This section will briefly summarize the findings from two full-scale specimen test programs. The purpose of these tests was to understand the response of CBFs while focusing on the gusset plate brace to frame connection performance. Various gusset plate connection design parameters were investigated, including the thickness and geometry of the gusset plate, types and sizes of clearance on the plate, and bolted and welded connections.

The first full-scale experimental program discussed hereafter was conducted under the guidance of Roeder and Lehman (2008). In this testing program, a single bay, single storey CBF was tested to establish the design guidelines on the detailing of gusset plates and to improve the base

knowledge of braced frame behavior (Johnson 2005, Herman 2006, Kotulka 2007 and Powell 2008). The test setup is shown in Fig. 2.6. The width of the CBF frame with a single diagonal brace is 12' (3.66m) and the height is 12' (3.66m).

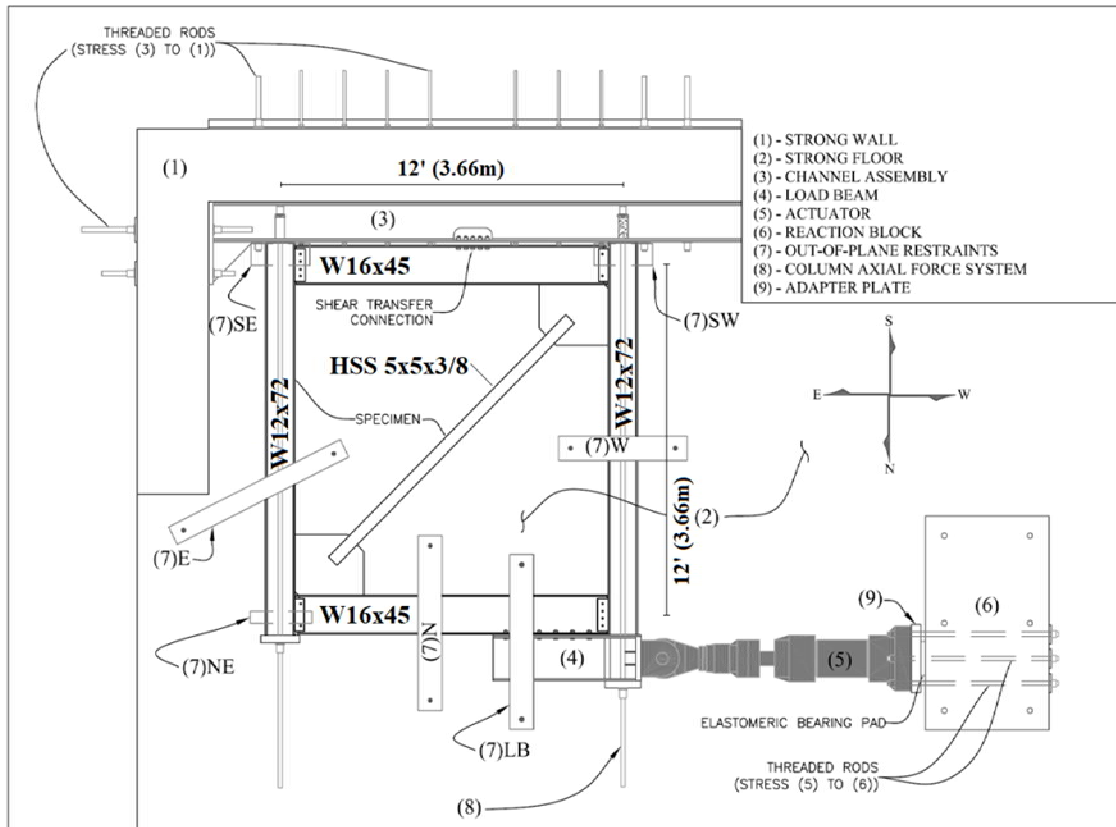


Figure 2.6 Test setup components and boundary conditions (Johnson 2005)

The tested specimen consists of typical beam and column sizes used in braced frames but the slab effects were not accounted for. For this test, all CBF members were sized in accordance with the *balanced design procedure*, which is based on balancing the yield mechanisms to prevent undesirable failure modes. In this testing program, an HSS 5x5x3/8 (HSS127x127x9.5) section was used for braces, the W16x45 (W410x67) section was used for beams and W12x72 (W310x107) for columns. The braced frame specimen was subjected to cyclic loading and various brace-to-frame connection design parameters were investigated and employed to

determine their effects on the overall performance of the frame. Several of these parameters are listed below.

- The shape of the gusset plate: tapered or rectangular gussets.
- Type of interface weld between the gusset plate and framing members: fillet and complete joint penetration (CJP) welds.
- Bolted and welded connections between the gusset plate and brace.
- Gusset plate thickness.
- Type and size of the clearance band of gusset plates: linear ($2t_g$) and elliptical ($8t_g$) for corner gusset plates.

A photo of the test setup illustrating the boundary conditions and loading techniques used during the experiment is given (Figure 2.7). To induce the expected frame behaviour of a real CBF system, the beams and columns were restrained from out-of-place buckling. An actuator applied displacement to the frame through the load beam, which was connected to the north beam and post-tensioned axial rods were installed to simulate the gravity loads in the columns.

Amongst the various conclusions that were derived from this testing program, the proposal of an $8t_g$ elliptical clearance for a corner gusset plate illustrated in Figure 2.8b is considered in this study. For comparison purposes, a corner gusset plate connections detailed with $2t_g$ linear clearance is also shown in Figure 2.8a.

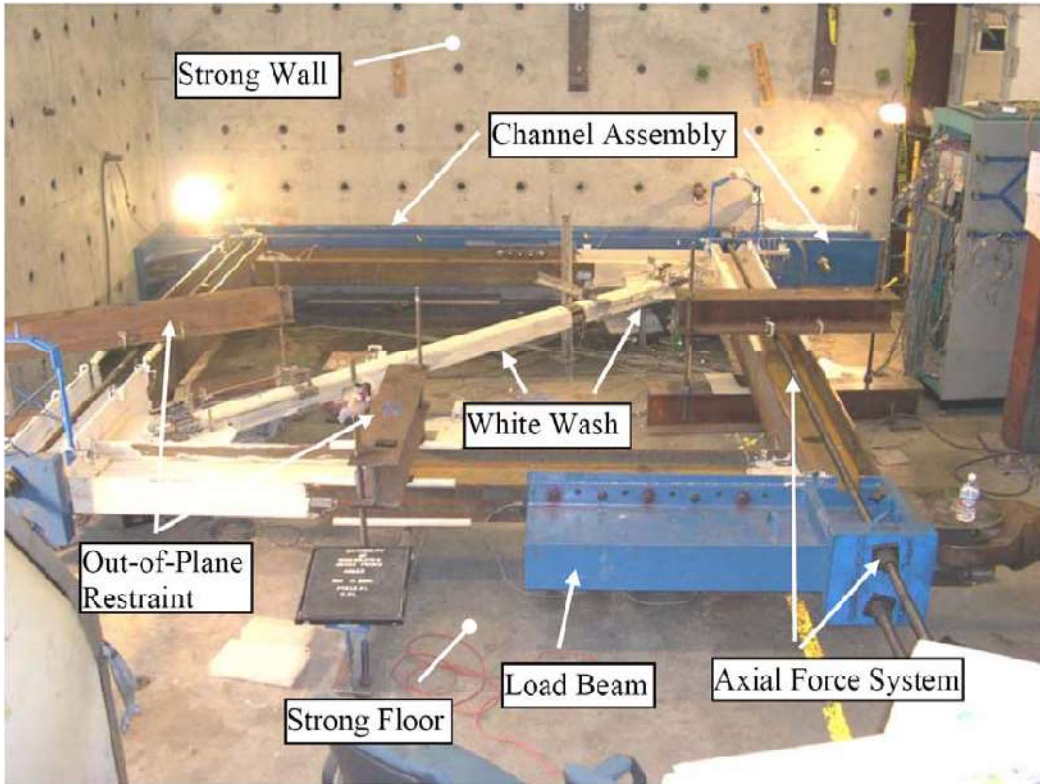


Figure 2.7 Single storey single bay test set up photograph (Johnson, 2005)

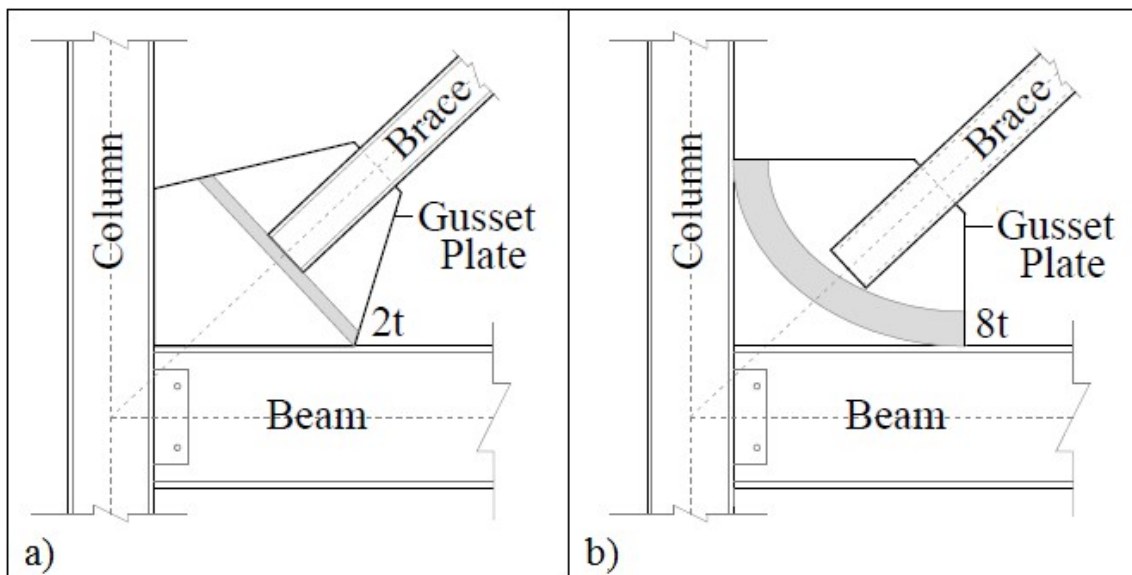


Figure 2.8 Corner gusset plate connection details: a) tapered $2t_g$ linear clearance, b) rectangular $8t_g$ elliptical clearance

Brace fracture at its mid-span length is the desired failure mechanism after plastic hinges are developed in the gusset plates at both ends of the brace located within the clearance band. Thus, the thickness of the gusset plate and its geometry strongly influence the brace yielding mechanism. However, previous studies revealed that although $2t_g$ linear clearance is provided for tapered gusset plates, it often leads to larger and thicker brace-to-frame connections, which possess limited deformation capacity, and in turn may drive the CBF system to premature failure. To overcome this drawback, researchers proposed to provide an $8t_g$ elliptical clearance band instead of the $2t_g$ linear clearance band in the gusset plate, as it often permits smaller and more compact gusset plates, in particular when rectangular shaped plates are used. The resulted connections have larger rotation capacity, which delays the fracture of the brace and reduces the damage to the welds between the gusset plate and the frame members, beams and columns. In this manner, the inelastic performance of the brace and the ductility of the CBF under large earthquake loads are improved.

Other recommendations that were outlined in the aforementioned studies are:

- Use of an interface weld between the gusset plate and framing elements equal to the gusset plate thickness with an electrode that matches the gusset plate metal to prevent premature weld cracking.
- Tapered gusset plates behave slightly differently than rectangular gusset plates. The tapered connection usually results in a smaller size but thicker gusset plate. Thus, they have the ability to reduce the plastic strain concentration at the brace center, prolonging the fracture life of the brace but they increase the inelastic demand on gusset interface welds and base metal. At large drift demands, crack welds and base metal fracture may be expected as shown in Figure 2.9.



Figure 2.9 Experimental brace-to-frame connection failure a) Crack at gusset-to-column weld b) Base metal fracture c) Base metal tear near column face (Kotulka, 2007)

The second testing program presented herein was continued at the National Center of Research Engineering (NCREE) in Taipei, China. In this program, the study of CBF was extended from the single storey frame to a multi-brace, multi-level configuration. The objective was to investigate the effect of composite concrete slabs on the CBF system and connection behavior under cyclic loading. For the first time, these tests allowed examination of the behavior of the middle gusset plate with different thicknesses of elliptical clearance band. The tests were performed and analyzed in two phases: three full-scale two-storey single-bay frames using multi-level X-brace configuration (Clark, 2009) and three full-scale three-storey frames using multi-level X-brace configuration at the bottom two stories and a chevron brace configuration at the top floor (Lumpkin, 2009). Both frame configurations included reusable composite floor slabs and were subjected to reversed cyclic loading at the roof level.

During the first phase, three tests labelled TCBF1-HSS, TCBF1-WF, and TCBF1-2t were conducted by Clark under the supervision of Profs Roeder and Lehman from Washington State University, US. The first two tests used $8t_p$ elliptical clearance on the corner and middle gusset plates while the third test TCBF1-2t utilized tapered gusset plates with $2t_p$ linear clearance required by the current code. Both specimens TCBF1-HSS and TCBF1-2t used HSS 5x5x3/8 for braces and specimen TCBF1-WF used wide flange braces. The frame setup for all three tests is shown in Figure 2.10.

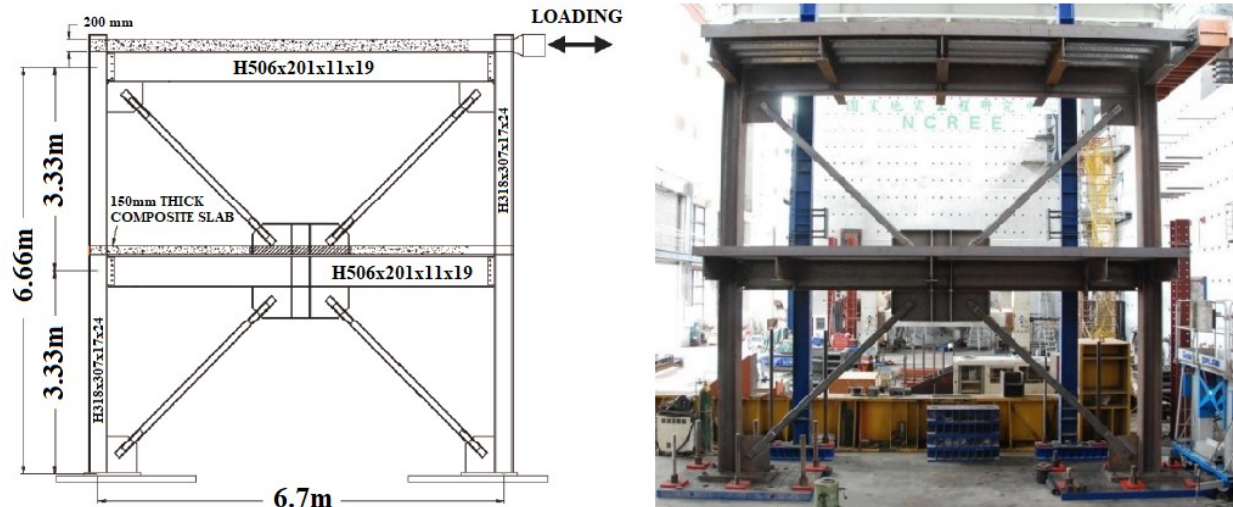


Figure 2.10 Test specimen TCBF1-HSS at NCREE in Taipei, Taiwan (Clark, 2009)

Lumpkin E.J. (2009) proceeded with the final phase and three tests where the specimens were labeled TCBF2-HSS, TCB2-WF and TCB2-IP were performed at NCREE under the guidance of Roeder, C.W.. The same braced frame configuration, which consisted of two W21x106 columns with two W21x68 beams at the bottom floors and a W24x94 beam at the top floor was used for all TCB2-series tests (Figure 2.11). The specimen TCBF2-HSS was designed for out-of-plane buckling using HSS 5x5x3/8 (HSS 127x127x9.5) on each storey, while the TCBF2-WF used wide flange braces H175x175x11. The TCBF2-IP was designed with in-plane buckling HSS 125x125x9 braces on each floor (Lumpkin, 2009). For TCBF2-HSS, the corner gusset plate used an $8t_p$ elliptical clearance band while the middle gusset plate used a $6t_p$ vertical offset from the beam as clearance. Both gusset plates were $3/8''$ (9.5 mm) thick and were rectangular in shape. For beam-to-column connections, a shear plate connection was used on the first floor and full moment resisting connections were used on the upper two levels.

A cyclic, pseudo-static, loading protocol was applied at the top of the frame. The actuators induced frame drift as the displacement control variable. To maintain a relatively constant loading rate, the duration of each cycle increased with increasing frame drift values. The resulted loading protocol (Figure 2.12) was used for all tests using the TCBF2 frame. The fracture of the North brace of Specimen TCBF1-HSS located at the 1st storey is shown in Figure 2.13.

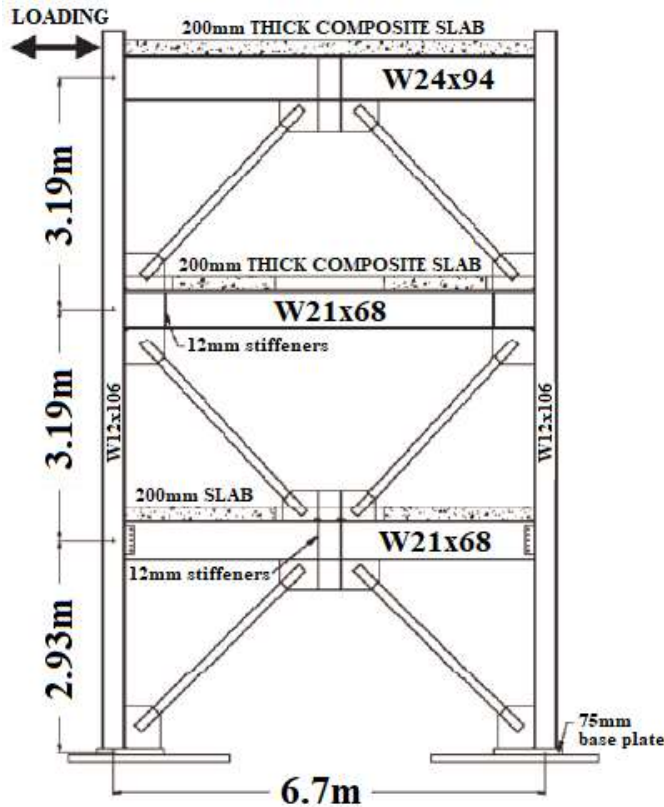


Figure 2.11 Test specimen TCBF2-HSS at NCREE in Taipei, Taiwan (Lumpkin, 2009)

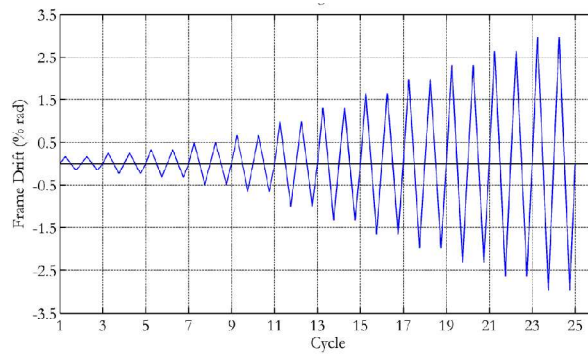


Figure 2.12 Loading protocol for TCBF2 series (Lumpkin, 2009)



Figure 2.13 North brace of Specimen TCBF1-HSS on the 1st storey a) Brace fracture at plastic hinge b) Initial tear lines c) Partial fracture d) Fracture Opening (Lumpkin, 2009)


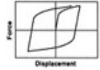
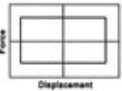
The relevant findings and recommendations formed from analysing the behaviour of specimens TCBF1-HSS and TCBF2-HSS are listed below.

- The benefit of $8t_g$ elliptical clearance band for corner gusset plates can be extended to multi-level buildings.
- Gusset plate interface welds should be designed for the full plastic capacity of the gusset plate rather than the brace.
- It is recommended to use a $6t_g$ vertical offset from the beam for clearance on middle gusset plates because it allows for substantial out-of-plane rotation while delaying interface weld tearing. This clearance is also allowed for more compact middle gusset plates, which require less or no edge stiffeners to better control the buckling of the plate.
- Shear plate connections result in less beam frame action because they are unable to transfer as much moment as fully welded connections. However, fully welded beam to column connections increase the frame action that occurs during the inelastic phases of CBF behavior, and thus the CBF is able to maintain a higher resistance after brace fracture or buckling. This, in turn, can decrease the possibility of a collapse or concentration of damage.
- The proposed balanced design procedure effectively balances the yield mechanisms and prevents undesirable failure modes in multi-level structures. As expected, first, the buckling of brace occurred and caused a plastic hinge to form at the middle of the brace under compressive load. At load reversal, initial tear lines appear at the plastic hinge, which is then followed by a partial fracture of the brace at the next tension cycle. The partial tear in the brace caused a reversal of the direction of buckling due to the new eccentricity created by the partial tear.

2.3 Past studies on Pall Friction dampers

The basic function of passive energy dissipation devices (PEDD) in a building is to absorb the earthquake input energy, thereby reducing energy dissipation demand on primary structural members and minimizing structural damage. The PEDDs can be classified into three categories: hysteretic devices, viscoelastic devices, and others. Hysteretic devices rely on the relative displacements of components within the device and are typically based on either metallic yielding or frictional sliding, while viscoelastic devices are velocity dependent. A brief summary of each PEDD with their advantages, disadvantages and their ideal hysteretic behavior are presented in Table 2.3.

Table 2.3 Characteristics of the most popular PEDDs (Symans et al., 2008)

Type of PEDD	Advantages	Disadvantages
Viscous Fluid Damper 	<ul style="list-style-type: none"> - Activated at low displacements - Minimal restoring force required - Proven record of performance 	<ul style="list-style-type: none"> - Possible fluid seal leakage - Higher initial cost
Metallic Damper 	<ul style="list-style-type: none"> - Stable hysteretic behavior - Familiar behavior (Yielding) 	<ul style="list-style-type: none"> - Device replacement after earthquake damage - May require nonlinear analysis (nonlinear behavior)
Friction Damper 	<ul style="list-style-type: none"> - Large energy dissipation per cycle - Not sensitive to temperature 	<ul style="list-style-type: none"> - Sliding conditions may change with time (reliability) - Nonlinear behavior - Large remnant displacements if no restoring force is provided by another system

In this study, friction dampers are selected for further investigations. Friction damper devices dissipate energy via frictional sliding across the interface between two solid bodies. Examples of such dampers include a series of steel plates that are bolted together. The activation of slip forces must occur before braces reach buckling. At the sliding interface between the steel plates, special materials may be utilized to promote stable coefficients of friction. Depending on the type of friction devices, they could be installed in line with single-diagonal or chevron steel braces. In the past, Pall (1979), Pall and March (1981) have proposed to be installed at the intersection of the X-braces. In general, hysteretic devices are installed in line with a brace and able to undergo the lateral deformation demand, while dissipating the hysteretic energy through friction. The purpose of installing friction devices into the structural system is to maintain the structural

components in the elastic range. The main frame and the supplemental energy dissipation system share the same deformation, which in turn is that of the entire system. It is paramount to assure a stable response of devices under dynamic loading. Thus, the energy dissipation devices installed in new or retrofitted buildings should slip before the shear resistance of the main structural system is reached. For example, friction energy dissipating devices are recommended to be used as follows:

- Friction devices in-line with brace members are added to the MRF system in order to reduce the interstorey drift.
- A minimum percentage of 25% MRF is required in order to reduce the residual drift when friction devices are installed in-line with braces of the CBF system in order to assure a back-up frame action (Tirca et al, 2018).

Pall friction dampers dissipate energy through friction developed by the relative sliding within two surfaces in contact, which are clamped by post-tensioned bolts. Herein, the slip length is defined by the distance from the initial position of the pre-tensioned bolt and the edge of the slotted hole. Also, the slip force is defined as the minimum required force to initiate sliding in the friction damper and is computed as the product between the friction coefficient and the normal force arising from the clamping action of the plate through pre-tensioned bolts. To obtain a smooth friction force 6 different materials or mechanical processes as depicted in Fig. 2.14 were considered by Pall (1979). The ideal hysteretic behavior of Pall friction dampers follows a smooth rectangular shape, which is characteristic of Coulomb friction.

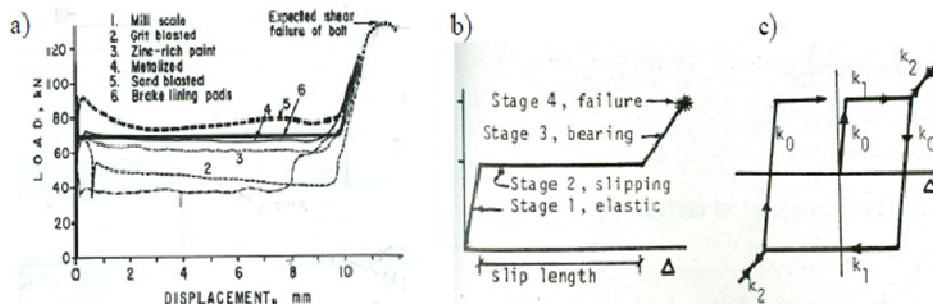


Figure 2.14 The response of the LSB joint: a) monotonic test; b) back-bone curve; c) hysteretic behaviour (Pall, 1979)

However, due to factors such as temperature, wear effects, and loss of pretension load, the friction coefficient during sliding may fluctuate, and in turn, affect the hysteretic behavior. In order to provide a stable friction coefficient in slip bolted joints, Pall investigated several types of surface treatments and lining materials under monotonic and quasi-static cyclic loading. The tests used a high-strength 12.7 mm pre-tensioned bolts to clamp the plates together. The hysteretic behavior of the six case studies and their associated degradation factor are shown in Figure 2.15.

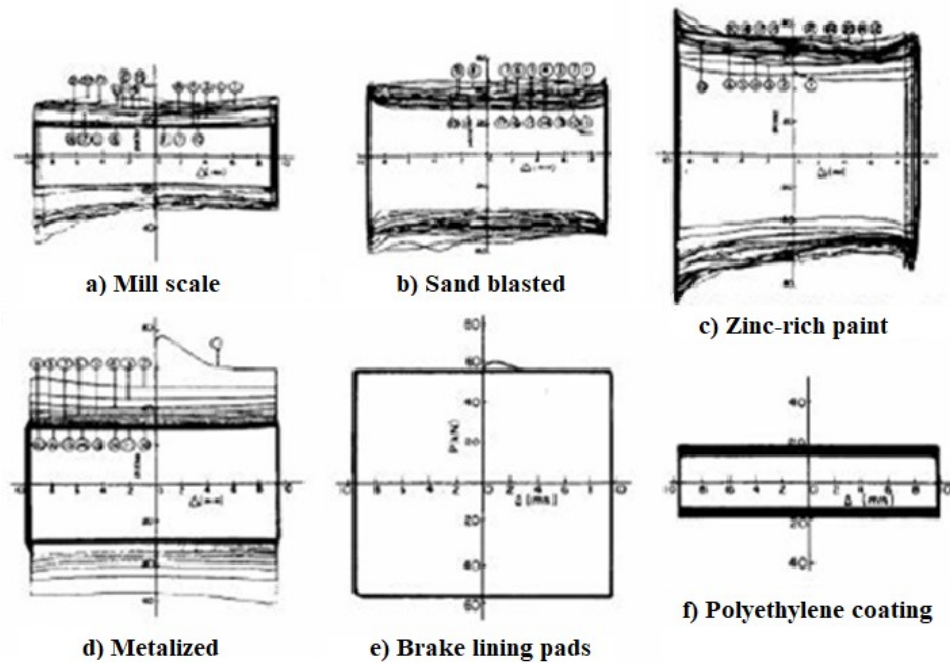


Figure 2.15 LSB joint and its hysteresis response under cyclic test of six case studies (Pall, 1979)

Pall has concluded that the most stable behavior was achieved when brake lining pads were used in contact with mill scale surface on plates. However, minor differences between the static and dynamic friction coefficients were observed.

In 1985, a reduced scale three-storey frame equipped with friction dampers was tested on a shake table at the University of British Columbia, Vancouver (Filiatrault, 1988). The response of friction dampers installed in braces added to a moment resisting frame (MRF) was much superior to that of a bare MRF. An earthquake record with a peak acceleration of 0.9g did not cause any damage to the friction sliding braced frame, while the MRF exhibited large permanent

deformations. In 1987, a nine-storey three-bay MRF frame equipped with friction dampers in an X-bracing system was tested on a shake table at Earthquake Engineering Research Center of the University of California at Berkeley (Aiken, 1993). All members of the friction damped MRF frame remained elastic for 0.84g acceleration, which was the maximum capacity of the shake table, while the MRF frame yielded at about 0.3g acceleration. The peak interstorey drift was 1%h_s. However, the behavior of a friction-sliding tension-compression diagonal brace (FSB) employed in this study may differ in several aspects.

As stated previously, Pall friction-dampers possess large rectangular hysteresis loops with a negligible fade over several cycles of reversals (Pall 1980, Filiatrault 1988). However, under large seismic excitations, the post-tensioned bolts may impact into the end of the slotted hole and undergo bearing or even bolt shear failure. Hence, the hysteretic behavior of the friction dampers is composed of four phases: elastic, slipping, bearing and failure of bolts, and the associated back-bone curve is illustrated in Figure 2.14b. However, the latter two phases were not considered in the previous testing by Pall. The latter phases were well documented in later studies conducted by Roik et al. (1988) and Lukkunaprasit et al. (2004). Furthermore, most computer models with friction dampers do not consider the limitation of slip distance and nor the bearing stage. In this light, Morales proposed design guidelines to calculate the required slip length in order to avoid the slip-lock phase (Morales, 2012). It is noted that, due to the lack of experimental tests on the bearing stage of friction dampers, the proposed computer model does not account for degradation during sliding once bearing has occurred. Also, the bearing and bolt tearing phases of friction damper are not calibrated with respect to experimental data, as there were none at that time.

Recent experimental testing of Pall friction dampers installed in line with braces was conducted in the Structure Lab of Polytechnique University Montreal (2014). The tests were carried out on full-scale brace-damper assemblies having 2 different nominal slip force capacities $F_{s1} = 550 \text{ kN}$ and $F_{s2} = 700 \text{ kN}$. As shown in Figure 2.16, the test setup consists of a 550 kN friction damper installed in line with an HSS 203x203x9.5 ($F_y = 350 \text{ MPa}$) at one end and connected to a W530x138 beam via a gusset plate on the other end. The damper specimen was detailed to accommodate a total slip distance of $1.3\Delta_d = \pm 65 \text{ mm}$, where Δ_d is the design slip length. Two high performance 1000 kN dynamic actuators were used to induce storey drift to the test setup.

The specimen was subjected to cyclic quasi-static displacement, real-time displacement histories obtained from a case study and wind load protocols as prescribed in ASCE/SEI 7-10. The test was reported by Tirca et al. (2018).

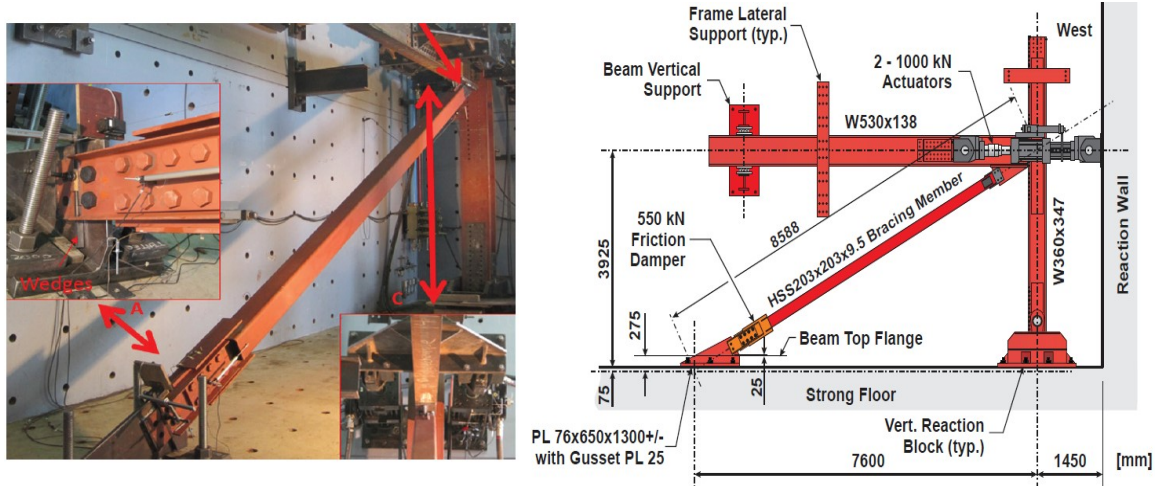


Figure 2.16 Friction damper test setup at Polytechnique University Montreal (Tirca et al., 2018)

In all these tests, the damper exhibited a uniform and stable hysteretic response with high energy dissipation capacity (Figure 2.16). Moreover, the slip force recorded slightly deteriorates from cycle to cycle under cyclic loading.

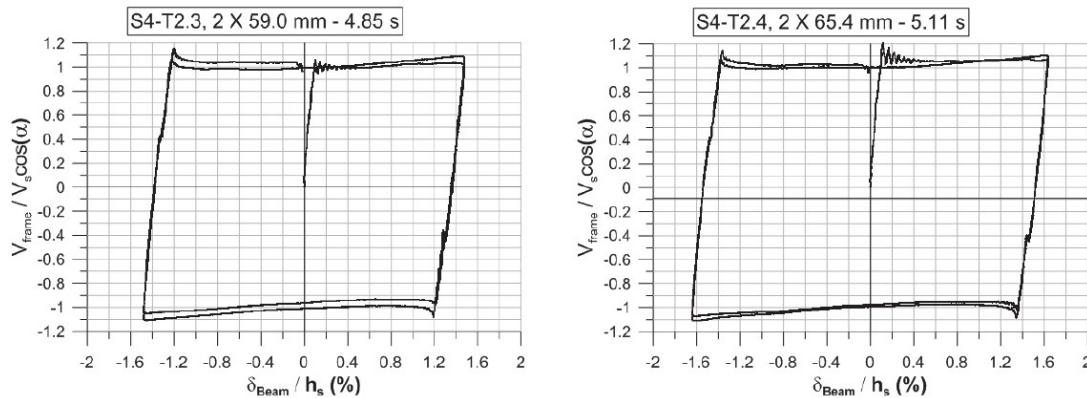


Figure 2.17 Sub-assembly subjected to harmonic displacement cycles (Tirca et al., 2018)

In North America, the first design guidelines addressing some provisions for steel frame with friction dampers were introduced in FEMA 356 (2000) and FEMA 450 (2003). Later on, the

aforementioned design guidelines were incorporated in Chapter 14 of ASCE 41-13, as well as in Chapter 18 of ASCE/SEI 7-10 standard. However, the aforementioned documents do not provide a force-based design method compatible with the building code.

Recent studies released by Tirca et al. (2018) proposed a simple force-based design method using $R_d=5.0$ and $R_o=1.1$ to design buildings equipped with friction dampers installed in CBF braces and a back-up MRF system. This approach in design represents a more attractive solution for day-to-day practices due to its similarities to CBF design. During the design process, ductility and overstrength related force modification factors R_d and R_o significantly reduce the base shear. In theory, friction sliding braced frame (FS-BF) could be assigned a high value of R_dR_o due to their high energy dissipation capacities and the possibility to adjust their slip length to accommodate anticipated displacements. However, the FS-BF system has little lateral stiffness during slippage, which makes the entire system prone to progressive drifting towards one predominant direction due to P-delta effects. In this parametric study, values of 4, 5 and 6 were considered for R_d , while the R_o factor was set to 1.1. In this light, a simple force-based method using $R_d=5.0$ and $R_o=1.1$ was concluded to have a median peak drift ratio between 1% and 1.5% for buildings up to 10-storey under both crustal and subduction ground motions. The study also proposes to design the MRF to resist 25% of the base shear used for the FSBF such that the frame behaves elastically up to 1.5% h_s .

The aforementioned guidelines specify general requirements, analysis procedures, and testing program required for friction damper. A brief review of these guidelines with highlights on friction damper devices design is presented below.

- Friction dampers are designed not to slip under wind load.
- Design HSS braces such that its compressive resistance C_r to be greater than 1.3 times the slip force of the attached friction damper ($C_r \geq 1.3F_s$).
- Similarly, apply capacity design to size the W-shape beams and columns of friction sliding braced frames. Consider C_u of braces in order to size the beam and columns assuming that braces should be kept straight during sliding.

- From time-history analysis establish the maximum damper displacement demand, Δ_{max} . Then, compute the required slip length of friction dampers, Δ_{slip} to be larger than 1.3 Δ_{max} in order to assure the required slip length, which is manufactured by friction damper's fabricator.
- To assure the frame action of FS-BFs, provide an additional MRF system designed to carry 25% of calculated base shear. Beams of MRF system should be designed to yield after friction dampers start to behave in the nonlinear range.

2.4 Modelling of Concentrically Braced Frames using OpenSees

Open System for Earthquake Engineering Simulation (OpenSees) is a computational platform for research in performance-based earthquake engineering developed at the Pacific Earthquake Engineering Research Center (McKenna 1997). Given its open-source nature, this software framework has been widely adopted by researchers for finite-element (FE) nonlinear analysis of structures due to its flexibility in material calibration.

A good CBF model would be able to replicate the post-buckling behavior of braces in compression and the fracture of brace due to re-loading in tension. To validate the plastic behaviour of braces, several parameters defined in the OpenSees model have been studied and validated against the experimental test results. The following models were built with nonlinear beam-column elements. Herein, the Menegotto-Pinto steel material (Steel02) was the nonlinear constitutive law used to model the material behaviour of all brace frame members (Aguero et al. 2006). To induce the out-of-plane buckling of braces, an initial imperfection of $L/500$ (L is the effective length of brace) is applied to the brace. Uriz et al. (2008) conducted an experimental and analytical study on CBF with chevron braces. It was concluded that brace fracture is often due to low-cycle fatigue. Hence, a fatigue material for HSS braces was first developed by Uriz and Mahin (2005). It consisted of a fatigue material assigned to the parental material (Steel02) of the brace to mimic the strength deterioration and eventual brace fracture of CBF. Thus, to simulate the behaviour of HSS braces, Uriz proposed to use 20 nonlinear beam-column element with distributed plasticity and fiber based section. The value of strain at which one cycle will cause failure (ϵ_o) and the slope of the Coffin-Manson curve in log-log space (m) are required as

input parameters in the definition of fatigue material in OpenSees. Later on, in order to further improve the accuracy of the material, Lignos and Karamachi (2013) proposed an empirical equation for HSS braces that is based on regression analysis where the strain ε_o is computed as a function of slenderness ratio, width-to-thickness ratio, and properties of brace steel material, while m was considered equal to -0.3. The expression for ε_o proposed by Lignos and Karamachi (2013) is shown below with its associated parameter conditions.

$$if \begin{cases} 27 \leq KL/r \leq 85 \\ 4.20 \leq w/t \leq 30.40 \\ 223 \leq F_y \leq 532 \text{ MPa} \end{cases} \text{ then } \varepsilon_o = 0.291 \left(\frac{KL}{r}\right)^{-0.484} \left(\frac{w}{t}\right)^{-0.613} \left(\frac{E}{F_y}\right)^{0.3} \quad (2.14)$$

As resulted, the equation was calibrated for stocky braces.

Similarly, to cover a larger interval of brace slenderness ratios, the following empirical equation was proposed for HSS braces by Tirca and Chen (2014) to predict the brace fracture due to low-cycle fatigue.

$$\text{When } 50 \leq KL/r \leq 150 \text{ then } \varepsilon_o = 0.006 \left(\frac{KL}{r}\right)^{-0.859} \left(\frac{b_o}{t}\right)^{-0.6} \left(\frac{E}{F_y}\right)^{0.7} \quad (2.15)$$

In the above equation, according to CSA/S16 standard, $b_o = b - 4t$ where b is the effective width and t is the thickness of the HSS brace. It is noted that the slope of Coffin-Manson m is assumed to be -0.5, which is the same as the value proposed by Uriz and Mahin (2005).

As more test data became available, a minimum of sixteen nonlinear beam-column with distributed plasticity was deemed sufficient to accurately simulate the hysteretic behavior of HSS brace upon failure (Hsiao et al. 2012). Several studies have shown that the gusset plate connection has a significant effect on the stiffness, resistance and inelastic deformation capacity of CBF. In this light, Hsiao provided an accurate simulation of brace-to-frame connection in OpenSees, which is discussed in a later section. In addition, it is required to consider other deterioration models associated with plastic hinging in steel components of CBF members like beam and columns that are involved in the development of storey mechanism, encountered after brace's fracture occurs (Lignos et al., 2012).

2.5 Gusset plate with linear clearance for brace-to-frame connection

Through the capacity design, the gusset plate of HSS brace connections is designed and detailed to provide ductile rotational behaviour. Thus, the factored flexural resistance of the connection shall equal or exceed $1.1ZR_yF_y$ of bracing member. Meanwhile, according to CSA/S16, the factored resistance of brace-to-frame connection shall equal or exceed both the probable tensile resistance of bracing members in tension, T_u and the probable tensile resistance of bracing members in compression, C_u . For chevron braces, when the tension brace force is less than T_u (e.g. $0.6T_u$ allowed for 4-storey and lower buildings) connections shall resist the gravity load combined with the forces associated with the attainment of R_y times the nominal flexural resistance of the beam at the brace connection. In this light, possible yield mechanisms and failure modes of CBF were identified by Johnson (2005) and are shown in Figure 2.18.

Seeing that seismic performance of CBFs relies on the ductility of the structure, all yield mechanisms such as yielding of the gusset plate, tensile yielding of braces, yielding of beams and columns at the gusset plate edge, and bolt hole elongation may all enhance the ductility of the frame (Kotulka, 2007). During severe earthquakes, these yielding will mitigate the overall damage to the structure by dissipating the energy through inelastic deformation. However, at all times, the failure modes shown in Figure 2.18 should not occur prior to brace fracture. By postponing the fracture of the brace, the brace is more likely to achieve its maximum inelastic deformation while dissipating energy. Herein, guidelines from CSA/S16 are followed to estimate the failure modes such as net section fracture of the brace, net section fracture of the gusset plate, buckling of the gusset plate, bolt fracture and block shear fracture are summarized in Table 2.5. In this study, the gusset plate inserted in the slotted HSS brace is welded as shown in Fig. 2.19. The probable axial force developed in the HSS brace member is transferred to the gusset plate through four fillet welds.

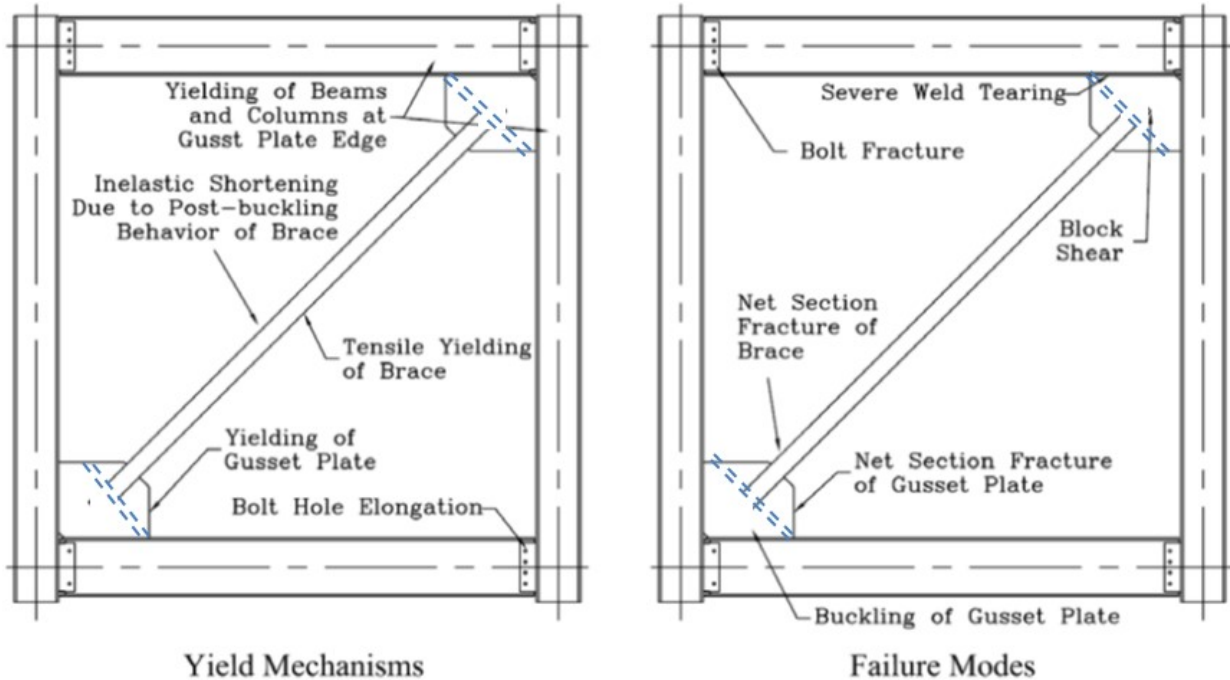


Figure 2.18 Yield mechanisms and failure modes (Johnson, 2005)

Table 2.4 Brace-to-frame gusset plate connection design

Failure Mode	Equation
1. Shear resistance of welding	$V_r = \min(0.66 \phi A_m F_y; 0.5 \phi A_w X_u)$
2. Tensile resistance of metal base	$T_r = \phi t_{gp} L_w F_y$
3. Yielding of gusset	$T_r = \phi A_{gp} F_y$
4. Buckling of gusset	$C_r = \phi A_{gp} F_y (1 + \lambda^{2n})^{-1/n}$
5. Net fracture of brace	$T_r = \phi_u A_{ne} F_u$ where $\phi_u = 0.75$
6. Block shear failure	$T_r = \phi_u \left[U_t A_n F_u + 0.6 A_{gv} \frac{(F_y + F_u)}{2} \right]$

According to CSA/S16, the minimum effective length of a fillet weld should be 38mm or 4 times the size of the fillet, whichever is larger. Meanwhile, the length of the fillet weld should provide a sufficient shear capacity in order to carry the transferred forces from brace to frame. The shear resistance of welding is the minimum between the strength per unit length of the base metal

along the fusion face of the weld and the shear resistance of the weld itself as per the equation shown below.

$$V_r = \min \begin{cases} 0.67\phi_w A_m F_u \text{ (yielding at the weld to base metal interface)} \\ 0.67\phi_w A_w X_u \text{ (fracture if the weld metal through weld throat)} \end{cases} \quad (2.16)$$

where A_m is the shear area of effective fusion face $A_m = D_w L_w$ and $X_u = 490 \text{ MPa}$ (E49XX electrode). Herein, D_w and L_w are the weld leg width and weld length. Conversely, A_w is the area of effective weld throat defined as $A_w = 0.707 D_w L_w$. For both cases, the coefficient ϕ_w is considered as 0.67.

The yielding resistance of the gusset plate, T_r , is given by Eq. (2.17).

$$T_r = \phi A_{gp} F_y \quad (2.17)$$

where A_{gp} is the effective area of gusset plate calculated as the product $W_w t_{gp}$ where W_w is the Whitmore width. The Whitmore width (W_w) is calculated using the following equation $W_w = 2L_w \tan 30^\circ + b_{HSS}$, which is established based on geometry.

The buckling resistance of the gusset plate, C_r , is calculated with the following equation.

$$C_r = \phi A_{gp} F_y (1 + \lambda^{2n})^{-1/n} \quad (2.18)$$

The compressive buckling resistance of the gusset plate is based on the slenderness $\lambda = \frac{KL_{avg}}{r} \sqrt{\frac{F_y}{\pi^2 E}}$, which requires to first determine the critical effective length L_{avg} . In the latter equation, K is considered equal to 0.67, while L_{avg} is calculated as an average value between the three lengths (L_1, L_2, L_3) resulted from the gusset plate geometry shown in Figure 2.19. This calculation is according to Hsiao et al. (2013). Furthermore, the radius of gyration of gusset plates r is estimated using $r = \sqrt{I_{gp}/A_{gp}}$ where $I_{gp} = W_w t_{gp}^3/12$ is the gusset plate's moment of

inertia in its weak section. In this manner, the buckling resistance of gusset plate $C_r = \phi A_{gp} F_y (1 + \lambda^{2n})^{-1/n}$ is determined using $n = 1.34$.

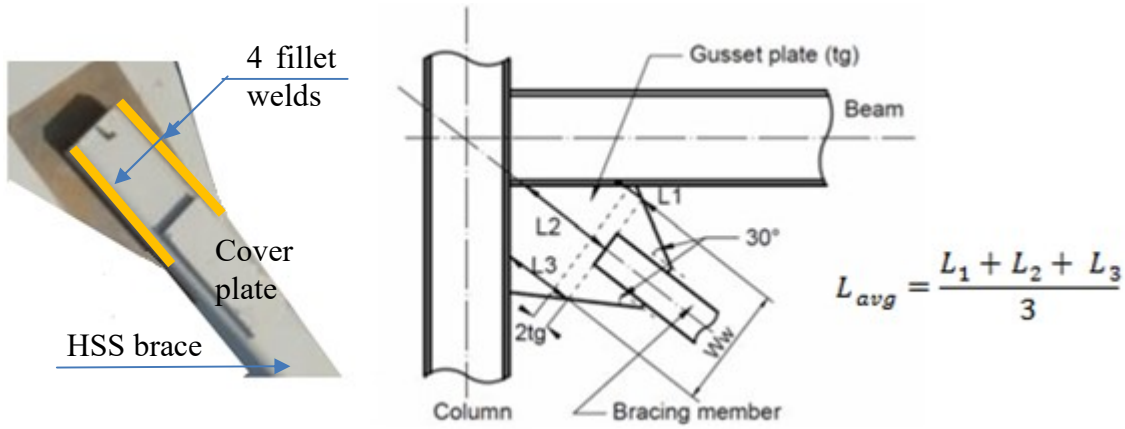


Figure 2.19 HSS brace to gusset plate connection after Hsiao et al., 2013

Based on the research conducted by Martinez-Saucedo and Packer (2009), the welding length has an influence over the net rupture of HSS braces due to the reduction of the cross-sectional area at the gusset plate slot. The cross-sectional capacity of the HSS brace is reduced due to shear lag. For this reason, a new clause 12.3.3.4 has been added to CSA/S16-14 to further reduce the effective area A_{ne} by a shear lag factor U for all slotted HSS welded connections (ie. $A_{ne} = UA_n$). This function defining the cross-sectional efficiency is plotted in Fig. 2.20 and is shown a smooth transition across the three limit states observed during testing: i) yielding and necking, ii) net section fracture from the shear lag effect and iii) tube wall tear out from block shear as presented in CSA/S16 commentaries.

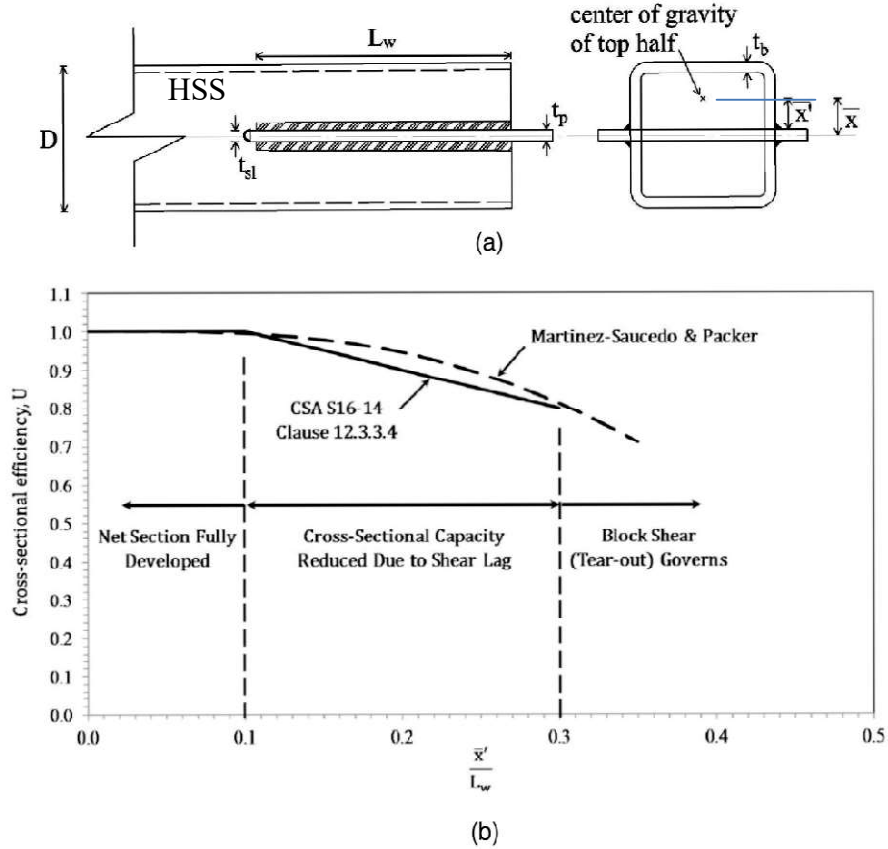


Figure 2.20 Shear lag effects on slotted HSS brace ends (Martinez-Saucedo and Packer, 2009 and CSA/S16 2004)

The net fracture of HSS brace is calculated as:

$$T_r = \phi_u A_{ne} F_u \quad (2.19a)$$

where $\phi_u = 0.67$ and $A_{ne} = A_n U$ when $\bar{x}'/L_w > 0.1$ and $A_{ne} = A_n$ when $\bar{x}'/L_w \leq 0.1$. Herein, \bar{x}' is the distance between the centre of gravity of half of the HSS cross-section taken from the edge of the connection plate (see Fig. 2.20) and L_w is the length of a single weld segment on the HSS (the usual case has the total weld length being $4L_w$) according to CSA/S16, 2014. Hence:

$$U = 1.1 - \frac{\bar{x}'}{L_w} \geq 0.8 A_n \quad \text{when } \bar{x}'/L_w > 0.1 \quad (2.19b)$$

$$U = 1.0 \quad \text{when } \bar{x}'/L_w \leq 0.1 \quad (2.19c)$$

In Figure 2.20, the bilinear approximation (solid line) given in the aforementioned equations was calibrated against experimental results (dashed line). It is noted that the curve suggested by CSA/S16-14 slightly underestimates the value of U to provide a conservative approach.

The tensile resistance of HSS brace connection due to block shear failure is calculated using Equation (2.20).

$$T_r = \phi_u \left[U_t A_n F_u + 0.6 A_{gv} \frac{(F_y + F_u)}{2} \right] \quad (2.20)$$

where ϕ_u is a factor taken as 0.75 for steel and U_t represents the efficiency factor taken as 1.0 for symmetrical blocks such as HSS brace. This equation has two parts: one is related to the net area in tension A_n , whereas the other is associated with the gross area along the shear failure plane A_{gv} . Since the gusset plate is not welded to the brace end (dimension perpendicular to brace length), there is no net area in tension, hence $A_n = 0$ while $A_{gv} = 4L_w D_w$ (assuming four fillet welds). The A_{gv} and A_n is shown in Fig. 2.21.

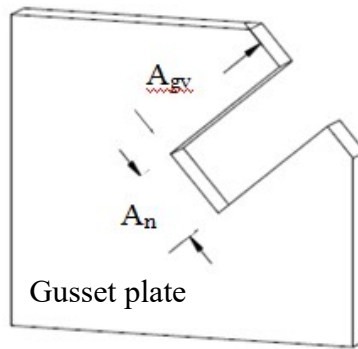


Figure 2.21 Illustration of A_{gv} and A_n areas (Lumpkin, 2009)

The HSS braces of the CBF systems are also prone to net fracture due to the reduction of the cross-sectional area of the brace at the gusset plate slot. This area can be reinforced with two cover plates. The tensile resistance of the brace with cover plates can be obtained using Eq. (2.21) where ϕ_r , ϕ and R_t are taken as 0.75, 1.0 and 1.1, respectively (AISC 2005, Haddad and Tremblay 2006).

$$T_{r,b} = U(\phi_r R_t A_{nb} F_{u,b} + \phi A_{g,CP} F_{u,CP}) \quad (2.21)$$

n the above equation, A_{nb} represents the cross-sectional area of the brace with the consideration of the gusset plate slot; $A_{g,CP}$ is the gross cross-sectional area of the added cover plate.

2.5.1 The geometry of $2t_g$ linear gusset plate

The geometry of $2t_g$ linear gusset plates can be determined graphically, using a computer-aided drafting program such as AutoCAD. This $2t_g$ clearance is measured from the end of the brace to a line that is perpendicular to the brace centerline as seen in Figure 2.22.

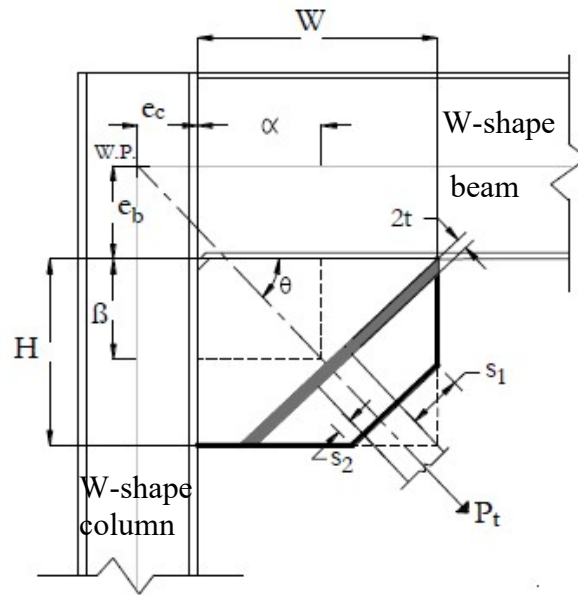


Figure 2.22 Geometry of gusset plate with $2t_g$ clearance (Lumpkin, 2009)

The centerline of the brace should intersect the working point (WP), which is defined as the intersection of the centerlines of the beam and column. With the WP established, it is possible to determine the gusset plate height (H) and width (W) by satisfying the equation given in AISC (20xx) and reproduced below.

$$\alpha + e_c = e_b \tan \theta + \beta \tan \theta \quad (2.22)$$

where α and β are given in Figure 2.22. Herein, β is defined as the distance from the beam flange to the centroid of the gusset-to-column connection, α is defined as the distance from the column flange to the centroid of the column-to-beam connection, e_b is half of the beam depth and e_c is

half of the column depth. Thus, α and β essentially locate the centroids of the gusset-to-column and gusset-to-beam connections along the centerline of the brace. This graphical method may be used to construct the $2t_g$ linear gusset plates. Equations for the height (H) and width (W) of the gusset plate are generated from the geometry shown in Figure 2.23.

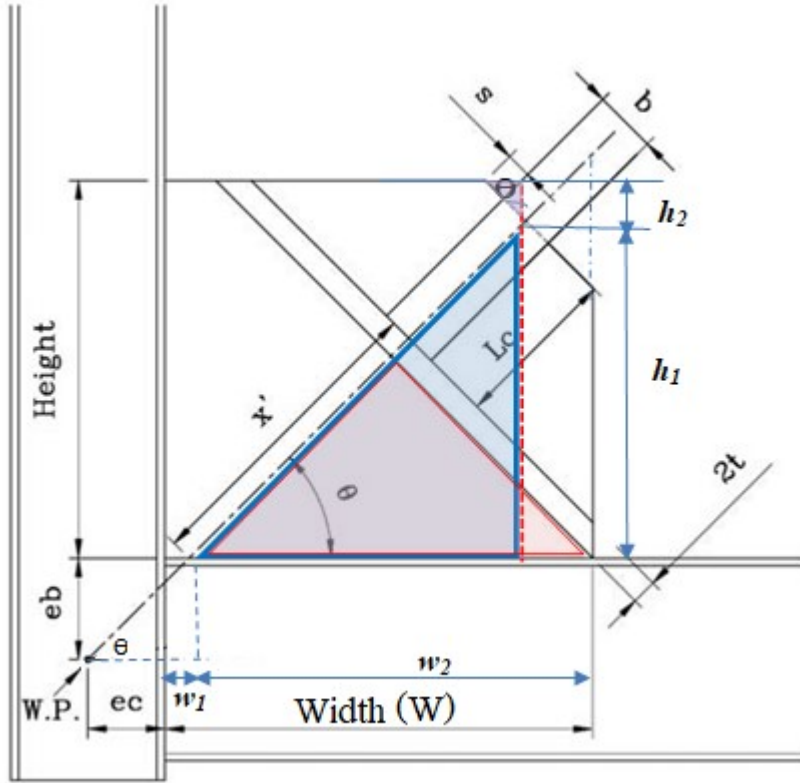


Figure 2.23 The gusset plate dimensions H and W are obtained graphically (after Johnson2005)

$$Height = h_1 + h_2 = (x' + L_c)\sin\theta + \left(\frac{1}{2}b + s\right)\cos(\theta) \quad (2.23)$$

$$Width = w_1 + w_2 = \left(\frac{e_b}{\tan\theta} - e_c\right) + \frac{x' - 2t_g}{\cos(\theta)} \quad (2.24)$$

As results, the value of x' can increase or decrease incrementally until a value satisfying Eq. (2.24) is found through convergence.

2.6 Elliptical clearance gusset plate

In 2005, Johnson has proposed the elliptical gusset plate. An $8t_g$ elliptical clearance band was recommended instead of a linear $2t_g$ clearance recommended by the code. It was concluded that

gusset plates with $8t_g$ elliptical clearance may lead to thinner and more flexible brace-to-frame connections, which allow larger out-of-plane deflection of braces while supporting the maximum load transferred by the brace. By allowing the gusset plate to yield and rotate during brace buckling, the strain accumulation at the center of the brace is reduced, thus prolonging the life of the brace. It is noted that the gusset plate must not fail prior to brace fracture as required by the capacity design method. In order to reduce the size of the gusset plate, an $8t_g$ elliptical clearance should be used for the brace-to-frame connection. The gusset plate geometry can be determined graphically, or mathematically using a procedure outlined by Kotulka (2007).

2.6.1 Rectangular gusset plate geometry design (Kotulka 2007)

Through experimental and analytical simulations by Yoo (2007), a value of $8t_g$ was deemed to provide the greatest inelastic deformation capacity prior to brace fracture. A list of steps to design the geometry of a rectangular gusset plate with an elliptical clearance is provided by Kotulka (2007). To determine the gusset plate dimensions (HT, WT) and the location of the center of the ellipse, it is required to use an iterative process until three geometric conditions are met. Furthermore, once the geometry is deemed adequate through convergence, the gusset plate is designed to satisfy equations provided in Table 2.4. In case that the thickness of the gusset plate needs to be changed, the whole process is repeated until all previous requirements are met.

Chapter 3

BRACE-TO-FRAME CONNECTIONS

The brace-to-frame connection design considers the effect of brace forces in order to allow the best overall seismic performance of the system while maximizing the system ductility prior to brace fracture. The HSS brace members of the CBF system are expected to exhibit fracture failure caused by low-cycle fatigue (Kotulka, 2007, Hsiao et al., 2013). Providing adequate connections detailing, the HSS braces will be able to yield and buckle out-of-plane, thus to elongate and shorten in order to dissipate energy. When braces are still loaded in compression after they exhibited buckling, a plastic hinge is formed at the brace mid-span length. To allow an HSS brace member to deflect out-of-plan, the gusset plate needs to possess sufficient flexural capacity to accommodate the brace deformation. After several loading and unloading cycles, a plastic hinge is intended to form in the clearance band of the brace-to-frame gusset plate connection. In this chapter, design procedures for $2t_g$ linear clearance gusset plate recommended by the code are presented first. Secondly, a more recent $8t_g$ elliptical clearance approach is also described in detail. Finally, relevant studies on the connection of Pall friction dampers installed in-line with CBF braces are presented. The OpenSees model for these connections is also presented.

To calculate the geometry of elliptical gusset plate shown Fig. 3.1, the procedure to follow is provided hereafter. The HT is assumed to be known and WT can be calculated as shown below:

$$HT = b + Nt_g \quad (3.10)$$

$$WT = a + Nt_g \quad (3.11)$$

where N is considered 8 and t_g is the thickness of gusset plate. From the above Eqs., it is required to determine a and b .

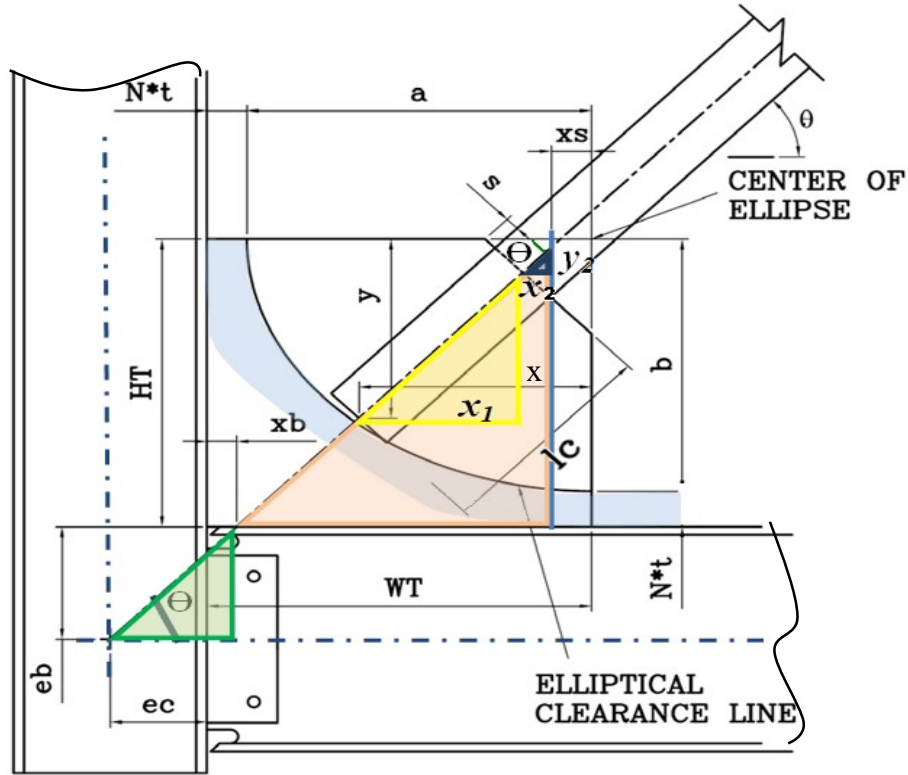


Figure 3.1 The gusset plate dimensions HT and WT obtained graphically (according to Kotulka, 2007)

From the triangle colored in green it results: $ec + xb = eb/\tan\theta$ or $xb = eb/\tan\theta - ec$.

From the orange triangle it results: $WT - xb - xs = b/\tan\theta$ or $WT = b/\tan\theta + xb + xs$ and Eq. (3.11) gives:

$$a = WT - \delta t_g = b/\tan\theta + xb + xs - \delta t_g \quad (3.12)$$

Using the yellow triangle provided in Fig. 3.1, $x_1 = lc \cos\theta$ and the x coordinate is computed as:

$$x = x_1 + xs + x_2 = lc \cos\theta + xs + (bf/2 + s) \cos^2\theta / \sin\theta \quad (3.13)$$

The y coordinate given in Fig. 2.24 is:

$$y = lc \sin\theta + (bf/2 + s) \cos\theta \quad (3.14)$$

As shown in Figure 3.1, the ellipse is offset from the beam and column faces at a distance of δt_g .

3.1 Modelling of gusset plate using ABAQUS

Due to the simplification in the modelling of gusset plates in OpenSees, it is not possible to get the stress or strain distribution in the gusset plate. By using finite element software Abaqus, it is possible to investigate where stresses are concentrated in the gusset plates when braces buckle. In this light, all brace-to-frame connections modelled in the case study in Chapter 4 were verified to have the expected $2t_g$ linear or $8t_g$ elliptical clearance band. The model in Abaqus did not consider the frame action. The purpose of the Abaqus model is to verify that the geometry of the gusset plate provides the expected clearance band.

There are 5 aspects of an element that characterizes its behaviour: type of elements, degrees of freedom, number of nodes (order of interpolation), formulation (Eulerian, Lagrangian, etc) and integration (Gaussian quadrature, reduced integration, etc). Shell elements are suitable for analyzing thin to moderately-thick shell elements with large nonlinear strain applications. In addition, higher-order elements are often used to avoid any hourglassing in the model, while reduced integration can be used to reduce the likelihood of shear locking to occur and to minimize computational time. Hence, all structural members are modelled as 8-node quadratic Shell element with reduced integration (S8R elements) to provide a relatively accurate result. The mesh size for braces and gusset plates are 30x15mm and 15x15mm, respectively. These mesh sizes were recommended by Hsiao et al. (2012) and illustrated in Figure 3.2. In his study, the finite element analysis was done in ANSYS using a 4-node quadrilateral shell element with 6 DOF (SHELL 181). The material is defined as a bilinear elastic-inelastic steel behavior with Young modulus 200GPa and Poisson's ratio 0.3.

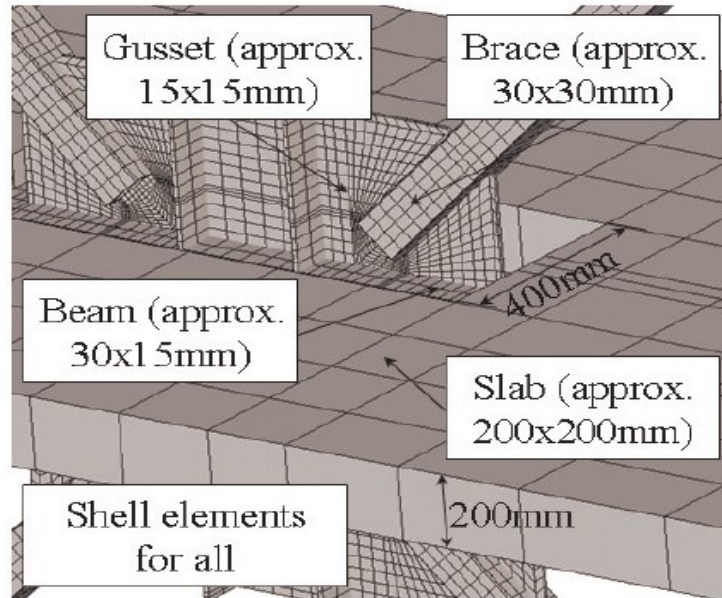


Figure 3.2 Finite element model in ANSYS by Hsiao et al. (2012)

Hourglassing may occur when large point loads are applied on a thin plate shell. This phenomenon is due to the Gauss points exhibiting zero strains. To avoid these types of hourglassing, rigid links were introduced at the reference point (master), where the load is applied, to the HSS perimeter nodes (slave), in order to have a realistic load path in the model. To simplify the modelling of welds, the residual stresses and distortions due to the welding process are completely neglected. Hence, the welded connections were modeled using tie constraints. Using symmetry, the model can be further reduced by carefully selecting adequate boundary conditions. The bases of the gusset plates were fully constrained to mimic the frame-to-gusset welded connections. From past experiments, the expected stress distribution or yield line is shown in the following figure.

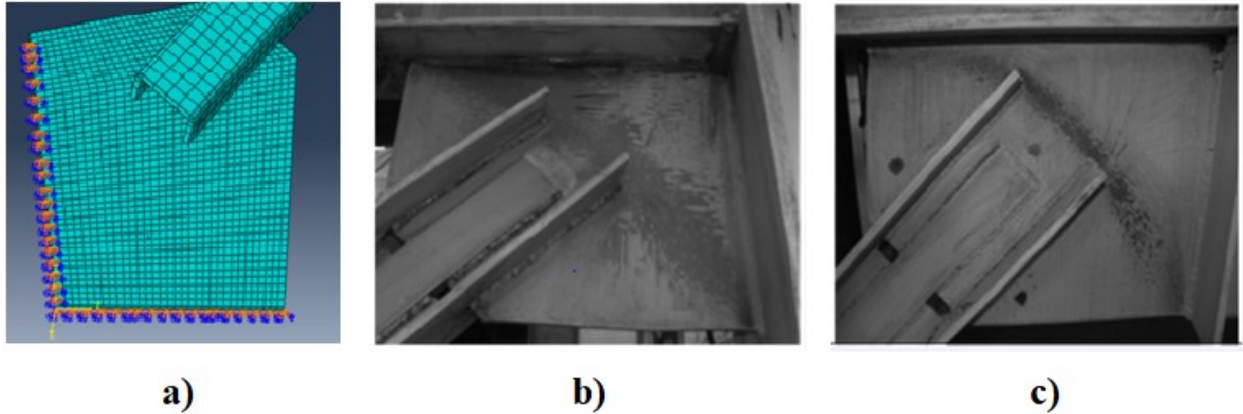


Figure 3.3 a) Boundary condition of gusset plate model in ABAQUS b) Expected yield line for $2t_g$ linear clearance c) Expected yield line for $8t_g$ elliptical clearance (Lumpkin, 2009)

Using ABAQUS and the modelling technique mentioned above, in Fig. 3.4 are shown the stress distributions obtained for a brace – gusset plate connection designed for the Case study presented in the Chapter 4. The $2t_g$ linear clearance model definitely has linear-like stress propagation, while the elliptical model shows stress concentrated around the brace, similar to what is observed in the experimental tests illustrated in Fig. 3.3 (Lumpkin E.J., 2009).

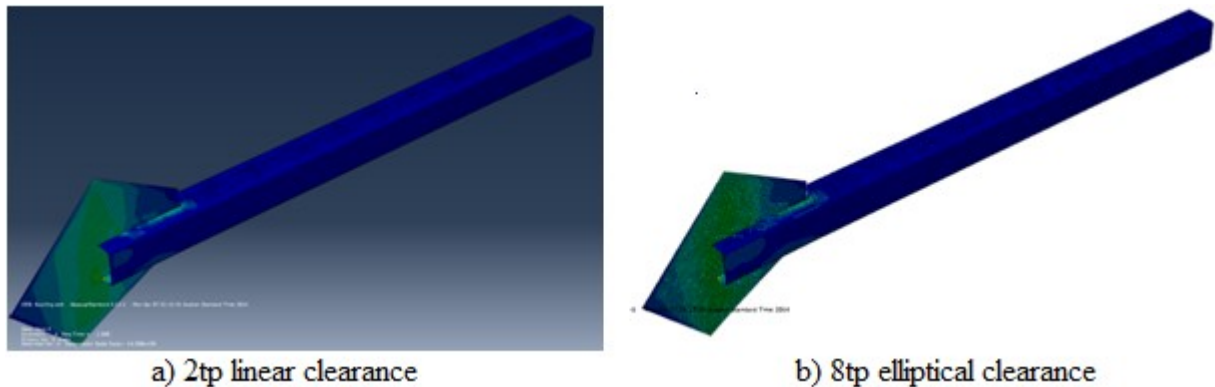


Figure 3.4 Stress distribution for both types of clearance band resulted from ABAQUS models

3.2 Friction damper in-line with diagonal brace

Previous studies have used mainly elastic-plastic models, which considered only the rectangular hysteresis shape characterised by the dry Coulomb friction, while the bearing phase has been ignored. Lukkunaprasit et al. (2004) have pointed out that previous studies did not take into account the nonlinear behaviour nor the slip-lock phase. In this light, Morales (2012) developed a computer model of friction damper device able to integrate the slipping and the slip-lock phase using the finite element library of the OpenSees software. It is noted that, due to the lack of experimental tests on the bearing stage of friction dampers, the proposed computer model does not account properly for it. Also, the bearing and bolt tearing phases of friction damper are not calibrated with respect to experimental data, as there were none at that time.

3.2.1 Modelling of friction damper in OpenSees

To reproduce the smooth transition from elastic behaviour to friction sliding, the simulation of this behavioural type was replicated by using the *Bouc-Wen* material developed in the OpenSees software. A parametric study has been conducted by Morales (2012). To simulate the stick-lock behaviour that occurs when the available slip length is consumed and the end post-tensioned bolts of friction device hit the edge of slotted hole, Morales (2012) used the model proposed by Lukkunaprasit et al. (2004) and added a series of translational springs made of *ElasticPerfectlyPlastic Gap* materials defined in both oscillation directions (tension and compression). Failure of friction damper device may be considered when the seismic demand expressed in terms of storey-drift is greater than the available slipping length of friction damper and the post-tensioned bolts impact the edge of slotted hole driving the post-tensioned bolts to behave either in bearing or in shear. For the first time, Morales (2012) has shown that the length of the slotted hole is an important design parameter for friction damper device. Hence, on the one hand, if the length of the slotted hole is too small, the energy dissipation capacity of the device is greatly reduced and the slip-lock phase is encountered earlier. On the other hand, if the slip length is too big (e.g. 2.5% h_s interstorey drift or greater), instability problems may occur and important permanent deformations are anticipated because the damper device does not possess a re-centering mechanism.

To capture the potential failure of friction damper, a *MinMax* material may be assigned to the *ElasticPerfectlyPlastic Gap* material to decouple the device when the maximum bolt bearing or shearing force is reached. The schematic representation of the friction-sliding brace is shown in Figure 3.5.

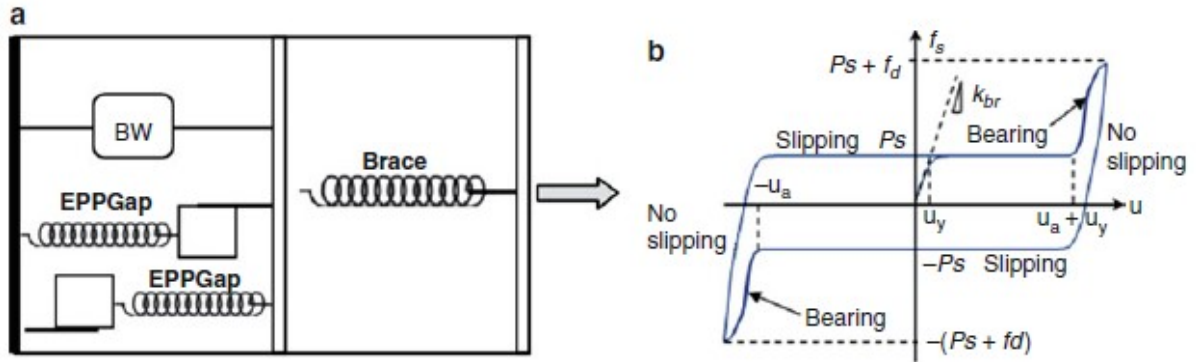


Figure 3.5 Schematic model and the hysteresis response including the bearing stage of a friction-sliding brace (Tirca, 2015)

As depicted, the device starts slipping when the slipping force, P_s is reached. The stiffness of the friction-sliding brace is the stiffness of the brace and the displacement at yielding (sliding) is $\Delta_y = P_s/K_b$. As shown in Figure 3.5b, the available slipping distance is $\pm u_a$. When the demand is larger than the available slipping distance the bearing phase occurs.

3.2.2 Calibration of parameters for the Bouc-Wen model

The parameters involved in the Bouc-Wen model influence the shape of the hysteresis response. Thus, tuning the hysteresis response parameters in accordance with the frame system behaviour, is an important issue addressed by several researchers (Baber and Noori 1985, Foliente 1993, Haukaas and Der Kiureghian 2004, Song and Der Kiureghian 2006). To simulate the inelastic behaviour of friction dampers based on the Bouc-Wen (BW) model a parameter study regarding its hysteresis shape was conducted by Morales (2012) and is illustrated in Figure 3.6. A summary of findings and recommendations regarding friction damper modelling is listed below:

- The *BoucWen* material is able to simulate the high nonlinear Coulomb friction and has the ability to represent different hysteresis shapes. It also ensures that there is a smooth

transition between the different phases of the friction damper, hence decreasing the likelihood of convergence problems.

- Parameters γ and β control the shape of the hysteresis cycle and the exponent n influences the sharpness of the model in the transition zones. Let Δ_y , P_{slip} and k_0 represent the yielding displacement, the slip force and the initial stiffness of the friction damper, which is the brace stiffness.

$$\gamma + \beta = \frac{1}{\Delta_y^n} \quad \text{where} \quad \Delta_y = \frac{P_{slip}}{k_0} \quad \text{and} \quad n = 10 \quad (3.15)$$

- The effect of the parameter "exponent n " on the hysteresis response is illustrated in Figure 3.12. As n increases, a smooth model is obtained, which approaches the elasto-plastic behaviour and better approximates the sharp transition zone. The restoring force $P_s(du/dt, z)$ has a linear and a nonlinear component as: $P_s(du/dt, z) = \alpha k_0 u + (1-\alpha)k_0 z$ where z is the hysteresis variable.
- For BW model without pinching or degradation, the value of $n = 10$ gives an acceptable level of prediction because the difference is reduced rapidly throughout the evolution of the post yielding stage (Morales 2012).
- The degradation process in stiffness and material related to loss of pretension force in bolts due to bolt impact and bearing were not considered. Thus, parameters controlling degradation were taken as:

$$A_0 = 1 \quad \text{and} \quad \alpha = A = \nu = \eta = 0 \quad (3.16)$$

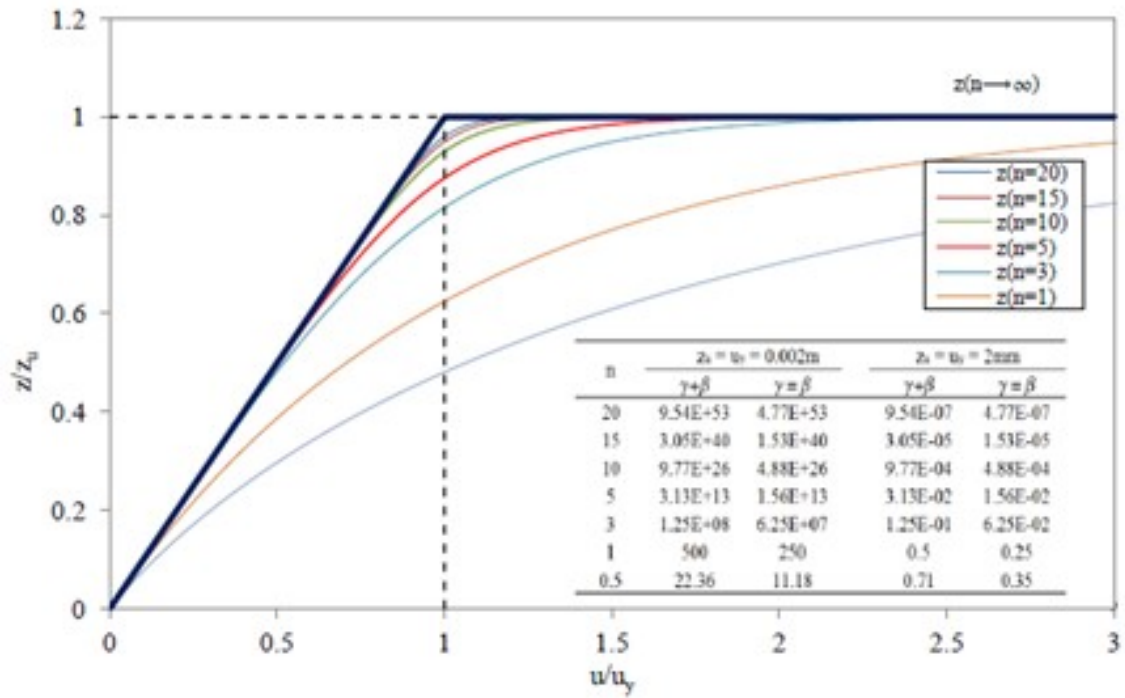


Figure 3.6 The effect of the parameter "exponent n " on the hysteresis response of Bouc-Wen model (Morales, 2012)

Chapter 4

CASE STUDY OF A HOSPITAL CBF BUILDING WITH ELLIPTICAL VERSUS TRADITIONAL GUSSET PLATE BRACE-TO-FRAME CONNECTIONS

In this chapter, a detailed design methodology is presented and a case study of a 4-storey hospital building located in Victoria, B.C. on Site Class C is illustrated. The proposed design method for CBFs with elliptical clearance brace-to-frame connections is developed considering the provisions for CBFs with linear clearance brace-to-frame connections provided in S16-2009 standard.

The case study is subjected to dynamic analyses by means of the linear modal response spectrum method using ETABS and the numerical integration nonlinear time-history method using the OpenSees software. The hospital building was subjected to a set of historical records selected and scaled to match the design spectrum (DS) for Victoria, B.C. For scaling, the procedure presented in ASCE/SEI 7-10 that was developed by Reyes and Kalkan (2011) was considered. A comparison between the response of CBFs with linear clearance gusset plate brace-to-frame connections and elliptical clearance gusset plate connections is presented.

4.1 Design requirements for hospital buildings

4.1.1 *Building description and geometry*

The selected case study is a 4-storey hospital building, located on firm soil (Site Class C) in Victoria, B.C. The typical floor plan of the hospital is the same as that of the Lion Gate hospital located in Vancouver, B.C. (Sherstobitoff, 2004). As illustrated in Fig. 4.1, the hospital building covers a rectangular area of 21.5 m times 80.4 m. The seismic force resistant system consists of four chevron MD-CBFs in the N-S direction and four MD-CBFs with diagonal braces in the E-W direction as presented in Fig. 4.2. All MD-CBFs are designed with tension-compression braces. The total building height is 18.2m, while the height of the ground floor is 5.0 m and that of typical floors is 4.4m.

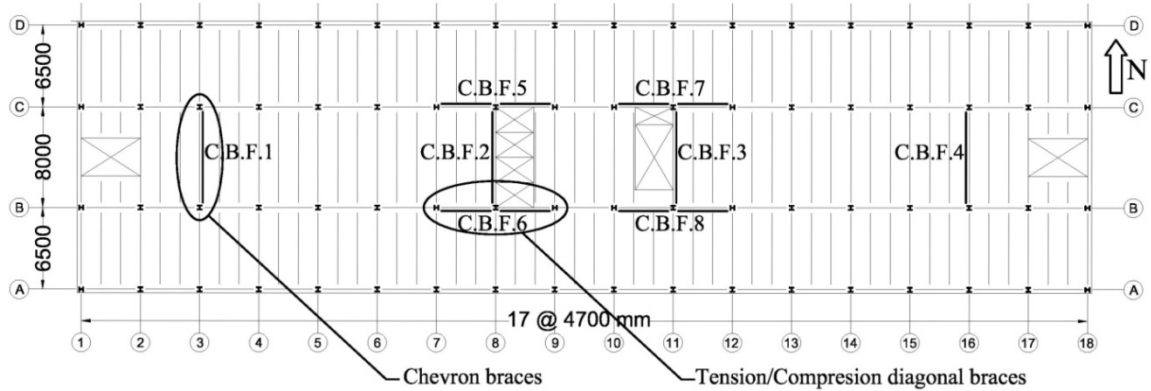


Figure 4.1 Plan view of typical floor

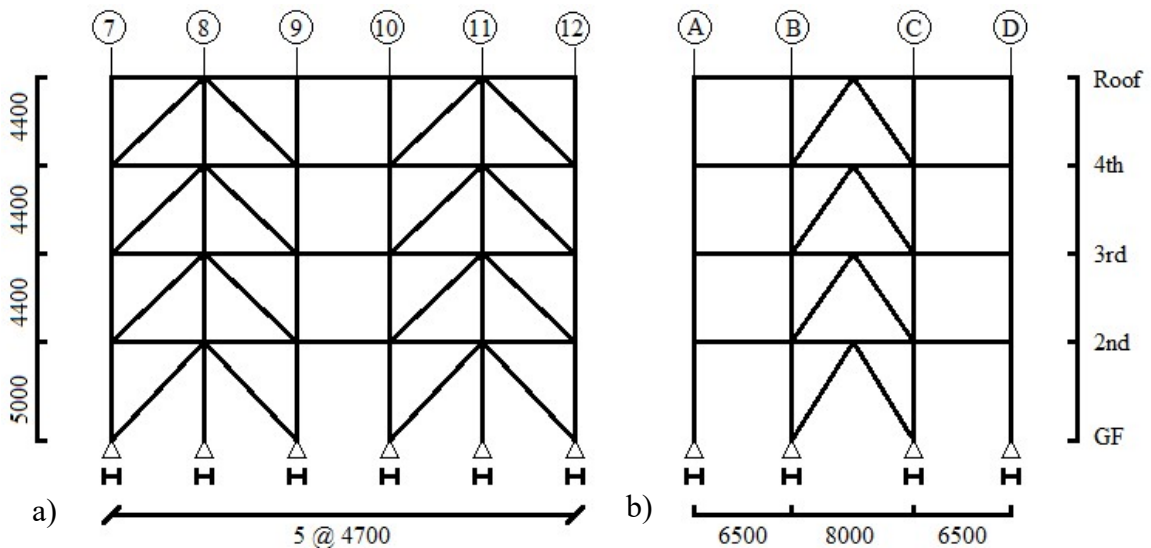


Figure 4.2 Elevation of braced frames: a) MD-CBFs with diagonal braces in E-W direction; b) Chevron MD-CBF in N-S direction

Prior to the frame design, it is required to estimate all loads and to determine the sections of members that will resist the gravity load. In this manner, the total seismic weight of the building can be estimated with adequate precision. All gravity loads, such as dead load (D), live load (L) and snow load (S) are assumed to be uniformly distributed. The dead load for typical floor and roof is provided in Table 4.1, while relevant climatic data for snow load and seismic load (E) estimation is shown in Table 4.2.

Table 4.1 Dead load on structure

DL on Typical floor (kPa)	
Material	Load (kPa)
Steel Deck with 100mm concrete cover	1.9
Partition walls	1.0
Mechanical components	0.3
Ceiling	0.1
Flooring	0.2
Total:	3.5
DL on Roof (kPa)	
Steel Deck with 100mm concrete cover	1.9
Mechanical components	0.3
Ceiling	0.1
Green roof (saturated weight)	1.0
Drainage and roof slope	0.4
Roofing (insulation, roof membrane)	0.2
Total:	3.9
DL -Cladding (kPa)	
East-West walls	2.0
North-South walls	1.0

Herein, a CANAM composite steel deck (38 mm deep steel deck with concrete topping equating 100mm thickness) was selected. Thus, for typical floor and roof, the dead load is 3.5 kPa and 3.9 kPa, respectively.

Table 4.2 Climatic data for Victoria, B.C., from NBCC 2010

Location	Snow load, [kPa]		Wind Pressure, [kPa]	Seismic Data [g]				
	S_s	S_r		S_a(0.2)	S_a(0.5)	S_a(1.0)	S_a(2.0)	PGA
	Victoria	1.1	0.2	0.57	1.2	0.82	0.38	0.19

According to NBCC 2010, for Victoria, the computed snow load at the roof level using Eq. (2.1) is $S = 1.25[1.1(0.8 \times 1.0 \times 1.0 \times 1.0) + 0.2] = 1.35 \text{ kPa}$, where $I_s = 1.25$ for post-disaster category buildings. The live load is presented in Table 4.3.

Table 4.3 Live load and Snow load on building

Floor	Minimum Specified Live Load (kPa)	Use and Occupancy
Roof	1.0	Flat roof with snow load = 1.35 kPa
4th floor	2.4	Office and Recovery area, light equipment
3rd floor		
2nd floor	3.6	Operation room and laboratories
Ground floor	4.8	Lobby and Cafeteria

The building structure is composed of a gravity system and a lateral force resisting system (LFRS). The gravity system is designed to withstand the maximum factored load obtained from the following load combinations:

$$a) 1.4D \quad (4.1a)$$

$$b) 1.25D + 1.5L + 0.5S \quad (4.1b)$$

$$c) 1.25D + 1.5S + 0.5L \quad (4.1c)$$

All secondary beams, girders, and columns are selected as W-sections, while brace members are made of hollow structural sections (HSS). In addition, all columns and beams were made of CSA G40.21 steel with nominal yield strength $F_y=345 \text{ MPa}$ and $F_u=450 \text{ MPa}$. The summary of the design is provided in Table 4.4 for secondary beams and girders and in Table 4.5 for gravity columns. Secondary beams and girders were selected such that the factored moment resistance of the member M_r is larger than the maximum bending moment $M_{f,max}$ due to gravity loads ($M_r > M_{f,max}$). However, in some cases, the serviceability criterion, which limits the beam deflection to be smaller than $l/360$, where l is the total beam length in millimetres, governed the selection of beam's sections. Gravity columns were designed such that the axial compressive resistance C_r to be greater than the factored axial compressive force C_f . It is noted that the live load reduction factor was taken into consideration as per NBCC 2010 requirements.

Table 4.4 Beam sizes of gravity system

Beam Sections (from Gravity Design)				
Storey	Secondary beam (6.5m span)	Secondary beam (8m span)	Interior Girder (4.7m span)	Edge Girder (4.7m span)
Roof	W310x21	W310x28	W360x33	W310x28
3 rd & 4 th floor	W310x21	W310x28	W360x33	W310x28
2 nd floor	W310x24	W310x33	W360x39	W310x33

Table 4.5 Gravity column sections for 4-storey hospital building

Column Sections (from Gravity Design)		
Storey	Interior Columns	Corner and Edge Columns
Roof	W200x42	W200x36
4 th floor	W200x42	W200x36
3 rd floor	W200x71	W200x52
2 nd floor	W200x71	W200x52

The columns of LFRS are designed to withstand the maximum factored load obtained from the load combinations presented as equations 4.2a and 4.2b. The earthquake load combination (Eq. 4.2b) governs the design of LFRS at all floors.

$$a) 1.25D + 1.4W + 0.5L \text{ or } 0.5S \quad (4.2a)$$

$$b) 1.0D + 1.0E + 0.5L + 0.25S \quad (4.2b)$$

As mentioned in Section 2.1.3, the empirical fundamental period of the building in the direction of loading, T_a , is computed as $0.025h_n$ for braced frames, where h_n is the building height. Thus, the fundamental period is $T_a = 0.025 \times 18.2 = 0.455$ s. According to NBCC 2010, when a dynamic analysis is provided, the computed fundamental period shall not be taken greater than $2T_a$. In this light, the design period used for the preliminary design of the studied building is selected as $2T_a = 0.91$ s. Then, a numerical model of the structure was developed to assess its dynamic response based on modal response spectrum analysis using the ETABS computer program (CSI, 2016). Based on the equivalent static force procedure (ESFP), the base shear, V is computed from the following equation: $V = S(T_a)M_v I_E W / (R_d R_0)$. The 5% damped spectral

response acceleration $S(T_a) = 0.459g \sim 0.46g$ corresponding to $T_a = 0.91s$ is obtained by interpolation. The factor accounting for higher modes effect on base shear is $M_v = 1.0$, while the earthquake importance factor I_E for post-disaster buildings is 1.5 ($I_E = 1.5$). For MD-CBFs, the values of the ductility-related and overstrength-related force modification factors are $R_d = 3.0$ and $R_0 = 1.3$, respectively. The total seismic weight of the building, W , including 25% snow load at the roof level is 32807 kN. The seismic weight of each floor is provided in Table 4.6. Thus, according to the ESFP, the base shear is $V = 0.46 \times 1.0 \times 1.5 \times 32807 / (3 \times 1.3) = 5804$ kN.

Table 4.6 Seismic weight

Floor	Dead load			Additional framing load			Total kN
	Load kPa	Area m ²	Total DL kN	Column/Beam kN	Snow 25% kN	Facade kN	
4	3.9	1759	6861	413	594	677	8544
3	3.5	1759	6157	475	0	1353	7985
2	3.5	1759	6157	540	0	1353	8050
1	3.5	1759	6157	625	0	1445	8228
						TOTAL	32807

The storey force acting on the SFRS with torsional effect is determined using Eq.(4.3).

$$F_x = F_x \frac{k_i}{\sum k_i} \pm \frac{T_x}{d} \frac{k_i d_i^2}{\sum k_i d_i^2} \quad (4.3)$$

In the equation above, the first term is related to the distribution of shear force among the MD-CBFs displaced in the direction of calculation and the second term is related to the shear component caused by torsion where all MD-CBFs regardless of their orientation participate. In this light, SFRSs that are located further from the CR (center of rigidity) are expected to have larger brace sections because of the torsion effect. In the N-S direction, the additional shear caused by torsion account for 33% and 10% in the case of outer chevron, and inner chevron, respectively. However, in the E-W direction, the 2% contribution of the shear caused by torsion is negligible. According to Fig. 4.1, the plan is symmetric in both orthogonal directions and the CR and CM are in the same location leading to $e_x = 0$. Thus, the eccentricity is equal to accidental eccentricity.

The brace sections obtained through the preliminary design are shown in Table 4.7. From the modal response spectrum analysis using ETABS software, the resulted first mode period is $T_1=0.559$ s in the N-S direction and $T_1=0.561$ s in the E-W direction, and the associated dynamic base shear is $V_{dyn,N-S}=7848$ kN and $V_{dyn,E-W}=8719$ kN, respectively. It is noted that both values are greater than $V=5804$ kN resulted from the equivalent static force procedure provided in the NBCC. The dynamic base shear V_{dyn} is significantly larger than the design base shear; hence members of MD-CBFs are redesigned and upgraded locally using the dynamic storey forces obtained in ETABS to meet the strength criteria. This iterative process adds more stiffness to the building, which shortens the dynamic period and is repeated until the increase in V_{dyn} no longer requires any structural alteration. During each iteration, the effects of P- Δ were considered in the analysis when required. The P- Δ effects amplify the seismic force. If the stability coefficient θ_x is greater than 0.1, the P- Δ effect must be taken into account during the design by amplifying the storey forces F_x by a factor U_{2x} associated to that floor. If the stability coefficient θ_x is lesser than 0.1, the effects of P- Δ is negligible and can be ignored in the design.

$$U_{2x} = 1 + \theta_x \quad \text{where} \quad \theta_x = \frac{P_x (R_d \Delta_x)}{R_o V_x h_{sx}} \quad (4.4)$$

where P_x is the cumulated gravity load computed using the load combination $D+0.5L+0.25S$ above the floor x under consideration, $R_d \Delta_x$ is the maximum inelastic interstorey drift at floor level x , V_x is the design seismic storey shear, while h_{sx} and R_o correspond to the storey height of floor x and the overstrength-related force modification factor, respectively. Due to the strict drift limit set for post-disaster buildings, calculations show that in both directions, P- Δ effect can be neglected at all floors. A summary of the design progression is shown in Tables 4.7, 4.8 and 4.9.

Table 4.7 Brace sections of MD-CBF1 & MD-CBF4 corrected as per ETABS analysis (N-S)

Outer chevron brace in N-S direction (MD-CBF1 and MD-CBF4)							
Braces from ESFP at $T=0.91s$ $T_{dyn}=0.559s$	C_f/C_r from ESFP	1 st iteration $T_{dyn}=0.495s$	C_f/C_r from ETABS	2 nd iteration $T_{dyn}=0.469s$	C_f/C_r from ETABS	3 rd iteration $T_{dyn}=0.471s$	C_f/C_r from ETABS
HSS 152x9.5	0.90	HSS 178x9.5	0.87	HSS 178x13	0.80	HSS 178x13	0.82
HSS 178x13	0.82	HSS 203x13	0.80	HSS 203x13	0.95	HSS 203x13	0.99
HSS 203x9.5	1.00	HSS 203x16	0.87	HSS 254x13	0.80	HSS 254x13	0.82
HSS 254x13	0.65	HSS 254x13	0.87	HSS 305x13	0.76	HSS 305x13	0.79

Table 4.8 Brace sections of MD-CBF2 & MD-CBF3 corrected as per ETABS analysis (N-S)

Inner chevron brace in N-S direction (MD-CBF2 and MD-CBF3)							
Braces from ESFP at $T=0.91s$ $T_{dyn}=0.559s$	C_f/C_r from ESFP	1 st iteration $T_{dyn}=0.495s$	C_f/C_r from ETABS	2 nd iteration $T_{dyn}=0.469s$	C_2/C_r from ETABS	3 rd iteration $T_{dyn}=0.471s$	C_f/C_r from ETABS
HSS 152x8	0.79	HSS 152x9.5	0.95	HSS 152x13	0.88	HSS 152x13	0.91
HSS 152x13	0.91	HSS 178x13	0.81	HSS 178x13	0.96	HSS 203x9.5	0.95
HSS 178x9.5	1.00	HSS 203x9.5	0.99	HSS 203x13	0.91	HSS 203x13	0.95
HSS 203x9.5	0.97	HSS 203x16	0.87	HSS 254x13	0.78	HSS 254x13	0.81

Table 4.9 Brace sections corrected according to ETABS analysis (MD-CBF5, 6, 7 and 8 in E-W)

Tension-Compression diagonal braces of MD-CBF in E-W direction							
Braces from ESFP at $T=0.91s$ $T_{dyn}=0.561s$	C_f/C_r from ESFP	1st iteration $T_{dyn}=0.506s$	C_f/C_r from ETABS	2nd iteration $T_{dyn}=0.486s$	C_f/C_r from ETABS	3rd iteration $T_{dyn}=0.483s$	C_f/C_r from ETABS
HSS 152x8	0.70	HSS 152x9.5	0.92	HSS 152x9.5	0.99	HSS 152x13	0.83
HSS 152x13	0.83	HSS 178x13	0.81	HSS 178x13	0.85	HSS 178x13	0.88
HSS 178x9.5	0.90	HSS 203x9.5	0.98	HSS 203x13	0.80	HSS 203x13	0.82
HSS 178x13	0.93	HSS 203x16	0.85	HSS 203x16	0.88	HSS 203x16	0.90

On the 4th iteration, no structural members were required to be modified and thus, the sections obtained from the 3rd iteration are kept. Using the updated sections, the first mode period of the building decreased to $T_{N-S} = 0.471$ s and $T_{E-W} = 0.483$ s while the base shear increased to $V_{dyn,N-S} = 9621$ kN and $V_{dyn,E-W} = 9349$ kN. The distribution of base shear along the building height is provided in Table 4.10.

Table 4.10 Distribution of base shear along the building height according to dynamic distribution

Storey	Storey force (N-S direction)	Storey force (E-W direction)
	[kN]	[kN]
Roof	3991	3982
4 th storey	2429	2582
3 rd storey	1748	1799
2 nd storey	1181	1258
Total base shear, V_{dyn}	9349	9621

Torsional sensitivity is determined by calculating the maximum of all values of B_x in both principle directions at each floor x using the following equation:

$$B_x = \delta_{max}/\delta_{avg} \quad (4.4)$$

where δ_{max} is the maximum storey displacement at the extreme points of the structure at level x induced by the equivalent static forces acting at distances $\pm 0.1D_{nx}$ from the centre of mass at each floor, while δ_{avg} is the average of the displacements at the extreme points of the structure at level x produced by the above forces. If any of the values of B_x exceeds 1.7 and $I_E F_a S_a(0.2) > 0.35$, the building is considered torsional sensitive. In this case study, during each iteration, the maximum ratio resulted at the 3rd floor in both directions, i.e. $B_{3x}=1.32$ for E-W and $B_{3y}=1.53$ for N-S, which are both less than 1.7; thus the building is not torsional sensitive.

4.1.2 Design of buildings with MD-CBF earthquake resisting system

A detailed design procedure of the MD-CBF considered in the last iteration (E-W) direction is presented for exemplification. The demand to capacity ratio is also included for each structural member selected. This ratio shows the amount of reserve capacity of the SFRSs of building to resist a severe earthquake.

4.1.2.1 Design of braces

Braces are the first members to be designed within a MD-CBF system. These elements are proportioned to resist the storey shear force in combination with the gravity load component (DL+0.5LL+0.25SL). Based on the capacity design concept, the shear force developed in the i^{th} floor is equally distributed to both tension and compression braces, which belong to the same storey. Braces were made of square Hollow Structural Sections (HSS) and comply with G40.21-350W Class C steel (cold formed) having $F_y=350$ MPa and $F_u=450$ MPa.

The brace element is designed to resist compression and tension factored forces (C_f , T_f) such that $C_f \leq C_r$ and $T_f \leq T_r$, where C_r and T_r are the member resistance in compression and tension, respectively. Herein, C_r and T_r are calculated as: $C_r = 0.9AF_y(1+\lambda^{2n})^{-1/n}$ and $T_r = 0.9AF_y$. In these formulas λ is the slenderness ratio, A is the cross-sectional area and F_y is the steel strength.

For this study, only Class 1 HSS brace sections were selected from CSA/S16-09. The slenderness ratio KL/r of bracing members shall not exceed 200 ($KL/r < 200$). Furthermore, when the specified short-period spectral acceleration ratio, $I_E F_a S_a(0.2)$, is equal to or greater than 0.75 or the specified one-second spectral acceleration ratio, $I_E F_a S_a(1.0)$, is equal to or greater than 0.30, the slenderness ratio of HSS bracing members shall not be less than 70.

$$\begin{cases} I_E F_a S_a(0.2) = 1.5 \times 1.0 \times 1.20 = 1.80 > 0.75 \\ I_E F_a S_a(1.0) = 1.5 \times 1.0 \times 0.38 = 0.57 > 0.30 \end{cases} \rightarrow KL/r \geq 70 \quad (4.5)$$

According to Clause 27.5.3.2 of CSA/S16, for HSS members with $KL/r < 100$, the width-to-thickness ratio b_0/t shall be smaller than $330/\sqrt{F_y}$, which is equal to 17.64 for $F_y = 350$ MPa. Herein, $b_0 = (b-4t)$ where b is the width and t is the wall thickness of HSS member.

The tension-compression diagonal brace sections resulted from design in the E-W direction are summarized in Table 4.11. Chevron brace sections resulted from design in the N-S direction are given in Table 4.12 and Table 4.13. In these tables, the gross area of braces A_g , the width-to-thickness ratio b_0/t , the radius of gyration r , the corresponding slenderness ratio KL/r , the brace compression resistance C_r and the reserve capacity in compression C_f/C_r are also given. For all braces, the demand-to-capacity ratio C_f/C_r shall be smaller than 1.0. For preliminary design, the effective length of the brace KL was considered as $0.9L$ to account for the length of brace-to-frame connections at brace ends. Therefore, the effective length of braces displaced in the E-W direction is 6180 mm and 5790 mm for ground floor braces and typical floor braces, respectively. Similarly, the effective length of braces displaced in the N-S direction is 5760 mm for braces at ground floor and 5350 mm for those at typical floor.

Table 4.11 Design summary of tension-compression braces of MD-CBFs in E-W direction

St.	$0.9L_b$ m	HSS Section	A_{brace} mm	b/t <17.64	r mm	KL/r <200	λ -	C_r kN	C_f/C_r <1.0	T_r kN	T_f/T_r <1.0
4	5.79	152x152x13	6680	15.00	56.1	103	1.37	855	0.82	2104	0.33
3	5.79	178x178x13	7970	7.69	66.5	87	1.16	1272	0.89	2511	0.44
2	5.79	203x203x13	9260	14.74	76.9	75	1.00	1734	0.83	2917	0.49
1	6.18	203x203x16	11200	9.69	75.3	82	1.09	1914	0.91	3528	0.49

Table 4.12 Design summary of inner chevron braces of MD-CBF2 and MD-CBF3 (N-S)

St.	0.9L _b m	HSS Section	A _{brace} mm	b/t <17.64	r mm	KL/r <200	λ -	C _r kN	C _f /C _r <1.0	T _r kN	T _f /T _r <1.0
4	5.35	152x152x13	6680	14.74	56.1	95	1.27	951	0.90	2104	0.38
3	5.35	203x203x9.5	7150	11.62	78.4	68	0.91	1469	0.95	2252	0.59
2	5.35	203x203x13	9260	8.80	76.9	70	0.93	1870	0.95	2917	0.58
1	5.76	254x254x13	11800	15.54	97.6	59	0.79	2714	0.80	3717	0.57

Table 4.13 Design summary of outer chevron braces of MD-CBF1 and MD-CBF4 (N-S)

St.	L _{eff} m	HSS Section	A _{brace} mm	b/t <17.64	r mm	KL/r <200	λ -	C _r kN	C _f /C _r <1.0	T _r kN	T _f /T _r <1.0
4	5.35	178x178x13	7970	9.69	66.5	80	1.07	1393	0.82	2511	0.42
3	5.35	203x203x13	9260	8.80	76.9	70	0.93	1870	0.99	2917	0.61
2	5.35	254x254x13	11800	15.54	97.6	55	0.73	2846	0.82	3717	0.61
1	5.76	305x305x13	14400	19.46	118.0	50	0.65	3697	0.78	4536	0.62

As resulted from Tables 4.12 and 4.13, for the bottom floors braces the slenderness ratio is less than 70 as recommended by CSA/S16 standard. To increase the slenderness ratio, one can increase the span between grid lines B and C from 8.0 m to 9.0 m to change the configuration of the braces or to increase the number of braces in order to reduce the section size. However, in the US steel design standard, it is not required to select braces with $kL/r > 70$.

4.1.2.2 Design of beams and columns

The goal of seismic design is to assure adequate strength, stiffness, and energy dissipation capacity for the seismic force resisting system. The current standard requires that all adjacent members and connections of bracing members of CBFs to be designed to resist forces corresponding to brace members' capacity. A summary of the design process is provided below.

All beams and columns were made of W-sections complying with ASTM A572 Grade 50 steel with $F_y = 345$ MPa and $F_u = 450$ MPa. For I-shape Class 1 and 2 members subjected to axial compression and bending, the following interaction equation is used:

$$\frac{C_f}{C_r} + 0.85 \cdot U_1 \cdot \frac{M_f}{M_r} < 1.0 \quad \text{where} \quad U_{1x} = \frac{\omega_{1x}}{(1 - C_f/C_e)} \quad \text{and} \quad C_e = \frac{\pi^2 E \cdot I_x}{L^2} \quad (4.6)$$

where the coefficient ω_1 is taken as 1.0 for members subjected to distributed loads or a series of point loads between supports and 0.85 for members subjected to a concentrated load or moment between supports, while the Euler buckling load C_e is dependent on the moment of inertia about x-x axis of the section I_x and the beam clearance length L .

Similarly, for I-shape Class 1 and 2 members subjected to axial tensile force and bending moments, equation 4.7 can be used.

$$\frac{T_f}{T_r} + \frac{M_f}{M_r} < 1.0 \quad (4.7)$$

As mentioned in Chapter 2, to design the beams of the CBF system with $R_d > 1.5$, two scenarios of braces buckling in compression and yielding in tension are considered:

- a) Braces have reached the stage of post-buckling and the beam has lost its braces support. Thus, after buckling is experienced by the compressive brace, only the probable post-buckling strength estimated as $C'_u = \min\{C_r R_y / \phi, 0.2 A_g R_y F_y\}$ is expected in the compression braces. The braces in tension are expected to develop the probable tensile strength, T_u . However, for buildings less than 4-storey height, $0.6 T_u$ is allowed to be used instead, where $T_u = A F_y R_y$.
- b) Prior to buckling, the beam of the chevron braced frame system is supported by braces at its mid-span. In this scenario, brace members are expected to be able to develop the probable buckling strength C_u in addition to the probable tensile strength T_u . Again, for buildings less than 4-storey height, $0.6 T_u$ is allowed. The probable compressive strength is computed as $C_u = \min\{1.2 C_r R_y / \phi, A_g R_y F_y\}$ where $\phi = 0.9$ and $R_y F_y = 460 \text{ MPa}$. Herein, $R_y F_y$ is the probable steel stress for HSS brace members.

The value of T_u , C_u and C'_u for each HSS brace computed with $R_y F_y = 460 \text{ MPa}$ is listed in the tables below:

Table 4.14 Probable resistance of brace members of MD-CBFs in the E-W direction

MD-CBF5, MD-CBF6, MD-CBF7 and MD-CBF8					
Floor	HSS section	T_u (kN)	$0.6 T_u$ (kN)	C_u (kN)	C_u' (kN)
4	HSS 152x152x13	3073	1845	1498	615
3	HSS 178x178x13	3666	2200	2229	733
2	HSS 203x203x13	4260	2556	3038	852
1	HSS 203x203x16	5152	3092	3354	1030

Table 4.15a Probable resistance of brace members in the N-S direction: inner MD-CBFs

MD-CBF2 and MD-CBF 3					
Floor	HSS section	T_u (kN)	$0.6T_u$ (kN)	C_u (kN)	C_u' (kN)
4	152x152x13	3073	1844	1666	615
3	203x203x9.5	3289	1974	2574	658
2	203x203x13	4260	2556	3277	852
1	254x254x13	5428	3257	4756	1086

Table 4.15b Probable resistance of brace members in the N-S direction: outer MD-CBFs

MD-CBF1 and MD-CBF4					
Floor	HSS section	T_u (kN)	$0.6T_u$ (kN)	C_u (kN)	C_u' (kN)
4	178x178x13	3666	2200	2441	733
3	203x203x13	4260	2556	3277	852
2	254x254x13	5428	3257	4987	1086
1	305x305x13	6624	3974	6478	1325

Beam member sections, as well as the axial force and bending moment sustained by these W-shape beams are provided in Table 4.16 (E-W) and Tables 4.17 and 4.18 (N-S).

Table 4.16 Beams design of MD-CBFs in E-W direction

Floor	Beam section	C_f kN	C_r kN	T_f kN	T_r kN	M_f kN.m	M_r kN.m	Comp. Eq. 4.6	Tension Eq. 4.7
4	W360x64	1662	2389	1662	2564	107	354	0.98	0.95
3	W410x85	2724	3240	1562	3402	88	537	0.99	0.62
2	W460x97	3185	3733	2119	3875	88	677	0.97	0.68
1	W460x106	3358	4098	2443	4253	98	742	0.94	0.71

Table 4.17 Beam design of inner chevron MD-CBF2 and MD-CBF3 in N-S direction

Floor	Beam section	C _f kN	C _r kN	T _f kN	T _r kN	M _f _{DL+0.5LL+0.25SL+E} kN.m	M _r kN.m	Comp. Eq. 4.6	Tension Eq. 4.7
4	W920x201	1588	7730	1588	8064	1762	2600	0.78	0.87
3	W920x201	2441	7853	1483	8064	1886	2600	0.93	0.91
2	W920x253	2773	9938	2272	10175	2411	3420	0.88	0.93
1	W920x313	3507	12252	2822	12537	3242	4220	0.94	0.99

Table 4.18 Beam design of outer chevron MD-CBF1 and MD-CBF4 in N-S direction

Floor	Beam Section	C _f kN	C _r kN	T _f kN	T _r Kn	M _f _{DL+0.5LL+0.25SL+E} kN.m	M _r kN.m	Comp. Eq. 4.6	Tension Eq. 4.7
4	W920x223	2045	8785	2045	9009	2103	2960	0.85	0.94
3	W920x253	2944	99930	2101	10175	2443	3420	0.90	0.92
2	W920x313	3827	12252	3142	12537	3073	4220	0.93	0.98
1	W920x381	4237	14980	3904	15309	3957	5280	0.92	0.99

The columns were assumed to be continuous over each two-storey. Similar to CBF beam design, columns must be sized by considering the minimum compression force resulted from the two scenarios:

- Assuming that all braces reached C_u and $0.6T_u$, the columns of CBF shall carry the tributary gravity load associated with (1.0DL+0.5LL+0.25SL) in combination with the axial load due to brace effects C_u and $0.6T_u$.
- By considering $R_d = 1$ and $R_o = 1.3$, the columns of CBF is designed to resist the factored load combination (1.0DL+0.5LL+0.25SL+1.0E).

For W-shape column members subjected to axial compression and bending, the following interaction equation is used:

$$\frac{C_f}{C_r} + 0.85 \cdot U_1 \cdot \frac{M_f}{M_r} < 1.0 \quad \text{where } M_f = 0.2ZF_y \text{ and } M_r = \phi ZF_y \quad (4.8)$$

where Z is the plastic section modulus of the column section and ϕ is taken as 0.9. A minimum of $0.2M_p$ of the column should be considered for column's design. Columns should meet the

requirement of Class 1 or Class 2 beam-column. The summary of CBF column design is presented in Table 4.19 and Table 4.20 (E-W), as well as in Table 4.21 and Table 4.22 (N-S).

Table 4.19 Exterior Column design of MD-CBFs in E-W direction

Floor	Height m	Column section	A_g mm ²	λ -	C_f kN	C_r kN	U_1 -	M_{fx} kN	M_{rx} kN	Comp. Check <i>Eq. 4.8</i>
Roof	4.4	W310x79	-	-	204	-	-	-	-	-
4	4.4	W310x79	10100	0.93	1383	2032	0.63	90	403	0.87
3	4.4	W360x216	-	-	3057	-	-	-	-	-
2	5.0	W360x216	27600	0.66	5299	7038	0.63	298	1342	0.94

Table 4.20 Interior Column design of MD-CBFs in E-W direction

Floor	Height m	Column section	A_g mm ²	λ -	C_f kN	C_r kN	U_1 -	M_{fy} kN	M_{ry} kN	Comp. Check <i>Eq. 4.8</i>
Roof	4.4	W310x107	-	-	-	-	-	-	-	-
4	4.4	W310x107	13600	0.76	2457	3201	0.75	56	254	0.96
3	4.4	W360x216	-	-	-	-	-	-	-	-
2	5.0	W360x216	27600	0.66	5004	7038	0.68	153	687	0.90

Table 4.21 Column design of inner chevron MD-CBF2 and MD-CBF3 in N-S direction

Floor	Height m	Column section	A_g mm ²	λ -	C_f kN	C_r kN	U_1 -	M_{fx} kN	M_{rx} kN	Comp. Check <i>Eq. 4.8</i>
Roof	4.4	W310x86	-	-	-	-	-	-	-	-
4	4.4	W310x86	11000	0.92	1591	2232	0.63	99	447	0.90
3	4.4	W360x287	-	-	-	-	-	-	-	-
2	5.0	W360x287	36600	0.65	6227	9422	0.63	407	1830	0.85

Table 4.22 Column design of outer chevron MD-CBF1 and MD-CBF4 in N-S direction

Floor	Height m	Column section	A_g mm^2	λ -	C_f kN	C_r kN	U1 -	M_{fx} kN	M_{rx} kN	Comp. Check Eq. 4.8
Roof	4.4	W310x107	-	-	-	-	-	-	-	-
4	4.4	W310x107	13600	0.76	2157	3201	0.64	124	558	0.86
3	4.4	W360x347	-	-	-	-	-	-	-	-
2	5.0	W360x347	44200	0.64	8560	11430	0.63	500	2249	0.94

Thus far, the same sections are for MD-CBF for both $2t_g$ linear clearance models and $8t_g$ elliptical clearance models. These sections are showed for MD-CBF (E-W) in Figure 4.3.

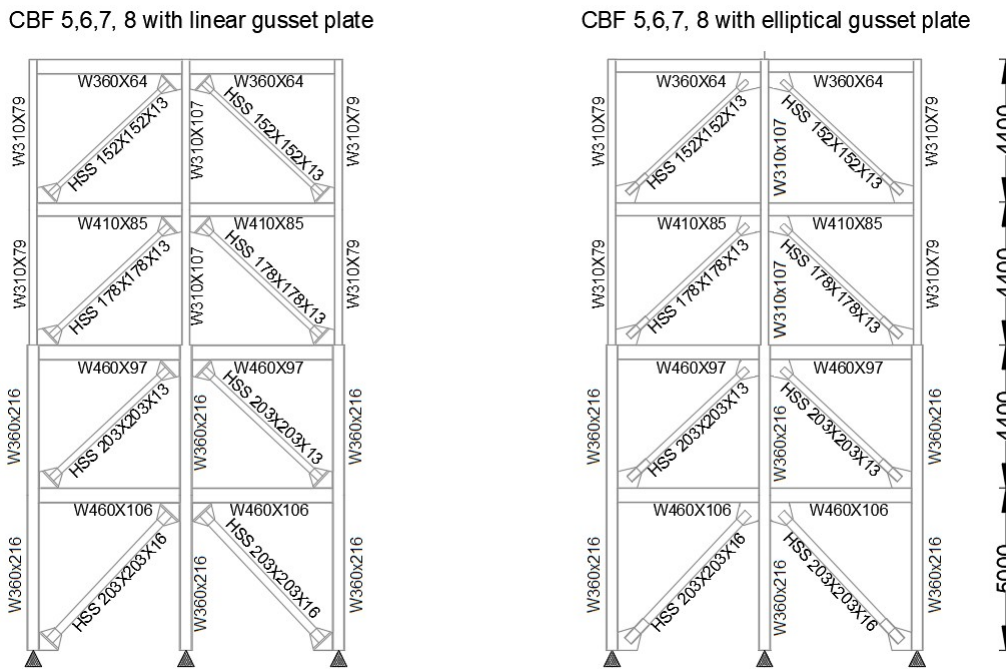


Figure 4.3 Members' section of MD-CBF in E-W direction

4.1.3 Brace-to-frame connection design

Current proceedings recommend to use a gusset plate with $2t_g$ linear clearance to provide sufficient yield mechanism in the gusset plate connecting braces to frames, where t_g is the thickness of the gusset plate. Using this linear clearance, it allows more cycles to be exhibited by the braces. Research conducted on linear clearance band of gussets with different clearance-to-

thickness ratios, weld lengths and angles are provided in the literature. Results showed that the $2t_g$ linear clearance leads to satisfactory brace performance. However, from the literature resulted that tests were done without considering the complete frame action and excluded the deformation demand resulting from cyclic inelastic axial and post-buckling deformation of the brace. Hence, in practice, it was shown that the linear clearance models still limit the inelastic cyclic deformation of braces before brace experiences fracture failure.

Recent studies propose an elliptical clearance model to provide a better yield mechanism in the gusset plate. Through experimental testing, the elliptical model improved the cyclic and inelastic performance of the frame and provided better rotational capacity, while being smaller and hence the brace's gusset plate connections could be more economical. For the elliptical model, different clearance-to-thickness ratio, weld length and angles were considered in testing. These results indicated that the 8 times the thickness of the gusset plate, $8t_g$, provides the best performance among the elliptical clearance models. For these reasons, the following gusset plate design details will utilize the $8t_g$ elliptical clearance model to further improve the building response.

Other related recommendations that were proposed are listed below:

- Weld thickness should be bigger than 0.9 times the thickness of the plate.
- Thinner gusset plate tends to perform much better; thick plates will increase the stiffness of the frame, hence attracting more loads to the frame.

Sample Calculation for B.F.1 and B.F.2 at the roof level:

The details on how to determine the gusset plate geometry for both $2t_g$ linear and $8t_g$ elliptical clearance models are shown below. In this study, the axial force from the HSS brace is transferred to the gusset plate through four E49XX electrode fillet welds with the ultimate strength of $X_u=490\text{MPa}$. The first step in design is to assume a weld led width D_w . In practice, the maximum size for a single pass weld is 8mm (Kotulka, 2007). In this manner, the required length of the weld can be determined using the following equation.

$$L_{weld} = \frac{\max(T_u : C_u)}{V_{r,unit}} \quad \text{where} \quad V_{r,unit} = \min \left\{ \begin{array}{l} 0.67\phi_w A_m D_w F_u \\ 0.67\phi_w 0.707 D_w X_u \end{array} \right. \quad (4.9)$$

Herein, $V_{r,unit}$ represents the strength per unit length of the weld. The calculated weld length was then rounded up to the next 1/8" increment for constructability and practical reasons. From geometry, the Whitmore width W_w can be calculated using the following equation:

$$W_w = 2L_{weld} \tan 30 + b_{brace} \quad (4.10)$$

Next, preliminary gusset plate thicknesses $t_{g,req}$ can be determined based on the yielding of the Whitmore width cross-section, the tensile resistance of metal base and the fracture of Whitmore width and, as resulted from Equations 4.11, 4.12 and 4.13, respectively.

The minimum required gusset plate thickness $t_{g,req}$ associated to yielding of gusset plate can be derived from Equation 2.17 of Chapter 2 as such:

$$t_{g,req} = \frac{T_u}{\phi W_w F_y} \quad (4.11)$$

Similarly, for the tensile resistance of metal base (gusset plate) $T_r = \phi A_{ne} F_y$, where A_{ne} is assumed to be equal to 2 times the product of $L_{weld} \times t_g$ (ie. $A_{ne} = 2L_{weld} t_g$), $\phi = 0.9$ and the required thickness of gusset plate is calculated as:

$$t_{g,req} = \frac{T_u}{\phi 2L_w F_y} \quad (4.12)$$

Finally, using Equation 2.19a with $A_{ne} = W_w t_g$, the minimum required gusset plate thickness related to net fracture of Widthmore width is:

$$t_{g,req} = \frac{\max(T_u ; C_u)}{\phi_u W_w F_u} \text{ where } \phi_u = 0.75 \quad (4.13)$$

The gusset plate thickness $t_{g,req}$ was considered and rounded up to the next 1/8" increment. Lastly, the buckling capacity of the gusset plate (Eq. 2.18), the tensile resistances due to block shear failure (Eq. 2.20) and net rupture of HSS brace with shear lag effect (Eq. 2.21) are verified using the obtained thickness of gusset plate. As mentioned in Chapter 2 Table 2.4, the compressive buckling capacity of the connection is $C_r = 0.9A_g F_y (1 + \lambda^{2n})^{-1/n}$ where $A_g = W_w t_g$ in this case. Similarly, the tensile resistance of HSS brace due to block shear failure is verified using $T_r = \phi_u \left\{ U_t A_n F_u + 0.6 A_{gv} \frac{F_y + F_u}{2} \right\}$ where $A_n = 0$ and $A_{gv} = 4t_{brace} L_{weld}$. Finally,

the tensile resistance of the gusset plate due to block shear failure is computed as $T_r = \varphi_u \left\{ U_t A_n F_u + 0.6 A_{gv} \frac{F_y + F_u}{2} \right\}$ using $A_n = t_g b_{brace}$ and $A_{gv} = 2t_g L_{weld}$.

These steps are repeated until all requirements are met. It is also noted that the initially estimated weld leg width D_w should be incremented to examine other possible connection designs. During the initial design phase, the overall height HT and width WT are often too large. By increasing D_w , shorter weld length L_w is achieved, which in turn produces a more compact gusset plate connection. Furthermore, the larger the gusset plate connection, the shorter the effective brace length becomes. Stocky braces tend to have less rotational capacity; hence, they should be avoided.

In general, *the governing failure modes for gusset plates are block shear failure and net rupture*. If the computed thickness $t_{g,req}$ does not meet all the requirements, it is recommended to increase the weld length L_w rather than the thickness of gusset plate t_g . As previously mentioned, thinner brace-to-frame connections tend to perform better. Furthermore, by increasing the weld length, thinner weld leg width D_w may also be achieved; which is beneficial for both cost and constructability.

In cases where block shear failure of HSS brace governs the design, it may be advantageous to start the design by assuming the weld length to be equal to two times the width of the attached brace ($L_w = 2w$) and to determine the required weld leg width D_w accordingly. In this manner, the framing system is less prone to shear lag effects and promotes thinner gusset plates. It also ensures that largest net area $A_{n2} = 1.00W_{HSS}t_{HSS}$ is considered during the net rupture check. It should lessen the number of iterations required to meet all requirements.

In Table 4.23, the $2t_g$ linear clearance gusset plate design parameters for the diagonal brace in the E-W direction are summarized. As illustrated, the following tables contain the selected weld leg width D_w , welding length L_w , Whitmore width W_w , thickness of gusset plate t_g , overall height HT and width WT of gusset plate, and the lengths L_1, L_2, L_3 used for the compressive buckling check. It is noted that the minimum size of fillet weld, D_{min} , used to connect two elements with a thickness t_1 and t_2 is 6.0 mm if $12 \text{ mm} < \max(t_1; t_2) \leq 20 \text{ mm}$ and $D_{min} = 8\text{mm}$ for $\max(t_1; t_2) > 20 \text{ mm}$. The maximum fillet weld size, D_{max} is equal to $(t-2)$ when $t \geq 6\text{mm}$. Therefore, the size of fillet weld showed in Table 4.23 responds to these requirements.

Table 4.23 The $2t_g$ clearance gusset geometry of brace-to-frame connections of MD-CBF (E-W)

MD-CBF with diagonal braces and $2t_g$ linear clearance for brace to frame connections (E-W)										
St.	D_w	L_w	W_w	t_g	L_1	L_2	L_3	$L_{ave}=\sum L_i/3$	HT	WT
	<i>mm</i>	<i>mm</i>	<i>mm</i>	<i>mm</i>	<i>mm</i>	<i>mm</i>	<i>mm</i>	<i>mm</i>	<i>mm</i>	<i>mm</i>
4	16	330	533	19.05	437	545	272	418	659	790
3	16	394	633	19.05	517	627	310	485	757	920
2	16	457	731	19.05	462	694	335	498	845	950
1	20	457	731	25.4	346	686	346	460	901	890

Similarly, the design of $8t_g$ elliptical gusset plate follows the same design process. However, when the same gusset plate thickness and weld length were used, the overall dimensions of the gusset plate, designed for an $8t_g$ elliptical clearance band, were much smaller than that resulted for the $2t_g$ linear clearance model. From previous research, thinner gusset plates were reported to perform better as they are less stiff. In this light, the weld lengths L_w were increased until thinner gusset plates were achieved. However, if the resulted geometry is bigger than that of $2t_g$ linear, it was disregarded since previous studies concluded that elliptical clearance gusset plate model should yield a more compact connection. In Table 4.24, the $8t_g$ elliptical clearance gusset plate design parameters for the diagonal brace in the E-W direction are summarized.

Table 4.24 The $8t_g$ elliptical gusset geometry of brace-to-frame connections of MD-CBF (E-W)

MD-CBF with diagonal braces and $8t_g$ elliptical clearance for brace to frame connections										
Floor	D_w	L_w	W_w	t_{gusset}	L_1	L_2	L_3	$L_{ave}=\sum L_i/3$	HT	WT
	<i>mm</i>	<i>mm</i>	<i>mm</i>	<i>mm</i>	<i>mm</i>	<i>mm</i>	<i>mm</i>	<i>mm</i>	<i>mm</i>	<i>mm</i>
4	14	410	625	15.875	204	364	30	199	603	730
3	16	394	633	19.05	274	397	65	245	618	771
2	16	457	731	19.05	201	458	72	244	712	810
1	20	473	749	22.225	120	502	126	250	815	809

All $8t_g$ elliptical clearance gusset plates are smaller in dimensions and thickness than the $2t_g$ linear model. Hence, braces are slightly longer when the $8t_g$ elliptical model is employed and they are expected to have better rotational capacity. The weld leg width, weld length, and Whitmore width remain relatively the same for the bottom three floors. For storeys 1 and 4 brace connections, a thinner plate is required for the $8t_g$ elliptical model. The non-linear behavior

of the brace on these floors is expected to be more favorable. The reserve capacities of the connections and the demand-to-capacity ratios for each verification case are presented in Tables 4.25 and 4.26.

Table 4.25 The brace-to-frame $2t_g$ linear clearance gusset plate connections calculations (E-W)

St.	Shear resistance of welds		Yielding of GP		Metal base resistance		Buckling of GP		Block shear of HSS		Net rupture of HSS	
	V_r	T_u/V_r	T_r	T_u/T_r	T_r	T_u/T_r	C_r	C_u/C_r	T_r	T_u/T_r	T_r	T_u/T_r
4	3286	0.94	3154	0.97	3906	0.79	2863	0.52	3091	0.99	3496	0.88
3	3918	0.94	3742	0.98	4657	0.79	3234	0.68	3685	0.99	4293	0.85
2	4550	0.94	4323	0.99	5409	0.79	3699	0.81	4279	0.995	5061	0.84
1	5688	0.91	5765	0.89	7212	0.71	5461	0.61	5227	0.99	5953	0.87

Table 4.26 The brace-to-frame $8t_g$ elliptical band gusset connections calculations (E-W direction)

St.	Shear resistance of welds		Yielding of GP		Metal base resistance		Buckling of GP		Block shear of HSS		Net rupture of HSS	
	V_r	T_u/V_r	T_r	T_u/T_r	T_r	T_u/T_r	C_r	C_u/C_r	T_r	T_u/T_r	T_r	T_u/T_r
4	3567	0.86	3080	0.998	4038	0.76	3043	0.49	3834	0.80	3255	0.94
3	3918	0.94	3742	0.980	4657	0.79	3690	0.60	3685	0.99	3844	0.95
2	4550	0.94	4323	0.985	5409	0.79	4266	0.70	4279	0.995	4531	0.94
1	5886	0.88	5171	0.996	6529	0.79	5144	0.65	5409	0.95	5389	0.96

As expected, the governing connection check is the block shear failure and the tensile net rupture. The minimum value of C_r and T_r from all these verification is kept as an indicator for brace-to-frame connection failure.

4.2 OpenSees model

4.2.1 OpenSees framework

Due to the highly nonlinear response of CBF when braces yield, buckle and eventually fracture, a non-linear time-history analysis was conducted in the OpenSees environment to compare the inelastic behaviour of buildings equipped with the code recommended $2t_g$ linear clearance gusset plate and the proposed $8t_g$ elliptical clearance model. In this light, a numerical 2D model with the option for braces to deform out-of-plane was built and described hereafter. To reduce the computational time, the structural system in the E-W direction was developed for a quarter of the building and in the N-S direction for half of the building considering the building's symmetry, as shown in Figure 4.4. In addition, the effect of rigid end zones was also considered for the beam-column and beam-column-brace connections (Figure 4.5). In this light, the considered rigid links were simulated using elastic beam-column elements with large stiffness.

4.2.2 Model description of steel bracing member (brace, beam, column)

All CBF members (braces, beams and columns) were modelled as non-linear force-based beam-column elements with distributed plasticity and fiber cross-section formulation. *Steel02* material known as Giuffre-Menegotto-Pinto with isotropic strain hardening is assigned to the nonlinear beam-column elements. The Giuffre-Menegotto-Pinto model is able to account for the accumulated plastic deformation at each point of load reversal and is based on the same concept and equations as the Menegotto-Pinto function where stresses are expressed as a function of strain. In this manner, the Baushinger effect and the residual stresses can be well accounted by using the *Steel02* material (Lamarche and Tremblay 2008). Parameters to define *Steel02* material were selected according to Aguero et al. (2006). Accordingly, the hysteresis loop follows the previous loading path for a new reloading curve, while deformations are cumulated. Thus, the accuracy of modelling the behaviour of brace that yields in tension and buckles in compression depends on the following parameters: initial out-of-straightness; the fiber discretization technique and numbers of fibers within the member's cross-section; the number of elements across the brace length; and the number of integration points per element.

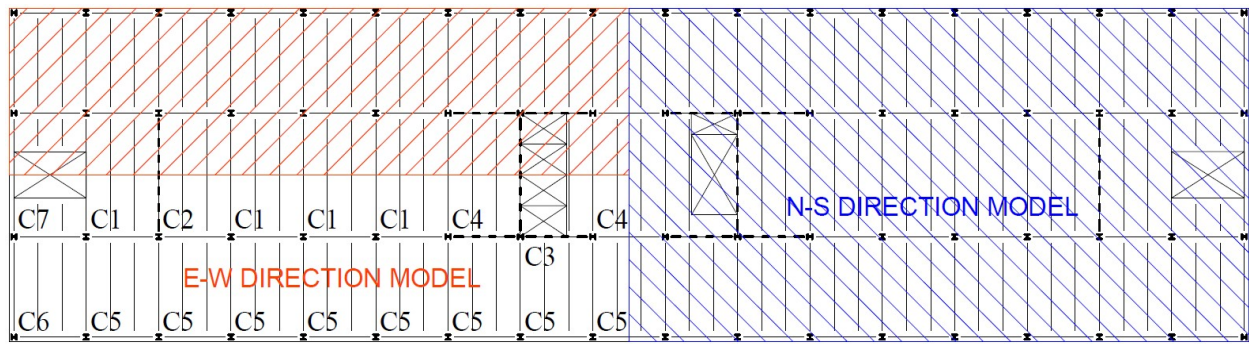


Figure 4.4 The OpenSees numerical model built for $\frac{1}{4}$ of the building

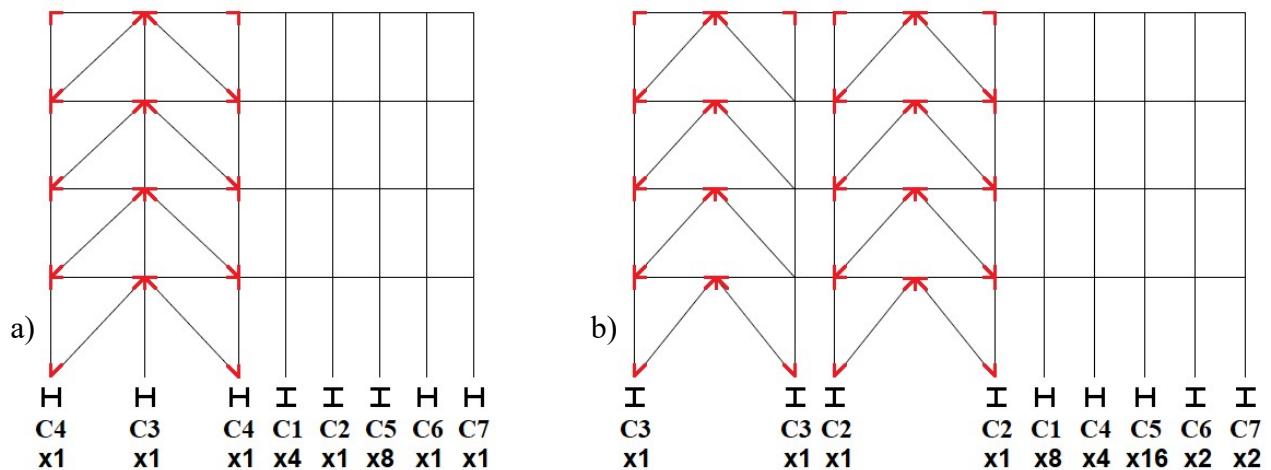


Figure 4.5 OpenSees model: a) E-W direction and b) N-S direction

In this light, to simulate the nonlinear behaviour of the CBF members, the cross-section of each element was discretized in fibers as illustrated in Figure 4.6. In total, the HSS brace cross-section was divided into 240 fibers, whereas, the W-shape cross-section was discretized into 120 fibers for beams and columns. In all cases, the web and flanges were discretized using 5 fibers along the thickness and 8 across with a total of 40 fibers, whereas the rounded corner of HSS section was divided into 20 fibers where four fibers in the circumferential direction and five in radial direction were used. Each brace member was discretized into 16 elements along its brace length with 3 integration points per element, as per Hsiao et al. (2013). By subdividing the cross-sectional area into fibers, it was possible to record both the compressive and tensile stress and strain distribution by selecting fibers on opposite sides of member with adequate accuracy. A

quadratic out-of-plan imperfection of $L_{br}/500$ was also assigned to braces to simulate and initiate the out-of-plane buckling of HSS braces; where L_{br} is the effective length of brace. Similarly, CBF columns were made of 8 nonlinear beam-column elements with distributed plasticity and fiber section having 4 integration points per element and an initial out-of-plane imperfection of 1/1000 of the effective length of column was considered. The CBF's beams were discretized into 4 elements with 3 integrations points per element and no out-of-plane imperfection. Increasing the number of elements or integration points will increase the accuracy of the model; however, it can significantly increase the computational time.

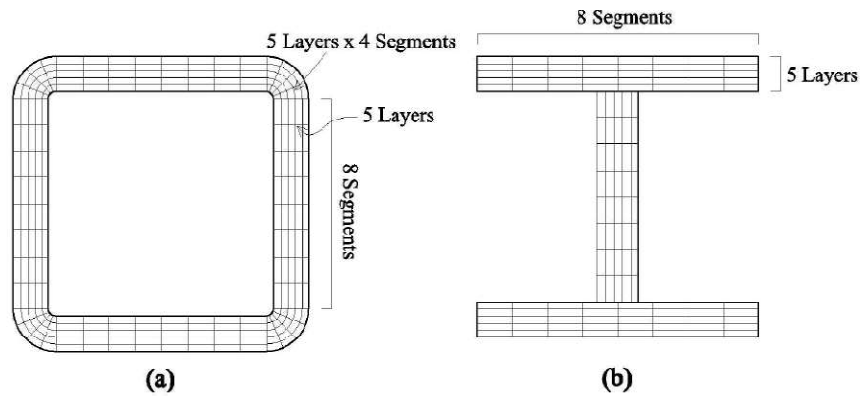


Figure 4.6 Discretization of fiber cross-section of (a) HSS brace cross-section and (b) W-shape cross-section for beams and columns

In addition, to replicate the failure of the brace member due to low-cycle fatigue, the fatigue material formulated in OpenSees is wrapped to the parental *Steel02* brace's material. Input parameters to define the fatigue material are taken from equation 2.13. Hence, the value of strain at which one cycle will cause failure, ϵ_o , and the slope of Coffin-Manson curve in log-log space, m , were computed from the equation proposed by Tirca and Chen (2014) for a wide range of slenderness ratios of square HSS brace cross-sections, $50 < KL/r < 150$. Consequently, the ductility coefficient $m = -0.5$ was considered constant for all braces, while the values of $\epsilon_o = 0.006 \left(\frac{KL}{r}\right)^{0.859} \left(\frac{b_0}{t}\right)^{-0.6} \left(\frac{E}{F_y}\right)^{0.1}$ calculated for braces of MD-CBFs are shown in Table 4.27 and Table 4.28, for $2t_g$ linear gusset plate and $8t_g$ elliptical gusset plate models, respectively. It is

noted that the actual effective KL_{eff} was measured by subtracting the diagonal length of the gusset plate L_{gp} from the full diagonal length of the frame. In this manner, the accuracy of the model is improved.

Table 4.27 Parameters for low-cycle fatigue material of HSS braces with $2t_g$ linear gusset plate model (MD-CBFs in E-W direction)

Parameters for low-cycle fatigue material of brace								
L_b (mm)	L_g	KL_{eff}	r_{brace}	KL_{eff}/r	bo/t	E/ F_y	ϵ_o	m
6433	545	5344	56.1	95	15.00	579.7	0.112	-0.5
6433	627	5180	66.5	78	7.69	579.7	0.141	-0.5
6433	694	5044	76.9	66	14.74	579.7	0.082	-0.5
6867	686	5494	75.3	73	9.69	579.7	0.116	-0.5

Table 4.28 Parameters for low-cycle fatigue material of HSS braces with $8t_g$ elliptical gusset plate model (MD-CBF in E-W direction)

Parameters for low-cycle fatigue material of HSS brace								
L_b (mm)	L_{gp}	KL_{eff}	r_{brace}	KL_{eff}/r	bo/t	E/ F_y	ϵ_o	m
6433	364	5705	56.1	102	15.00	579.7	0.118	-0.5
6433	397	5639	66.5	85	7.69	579.7	0.151	-0.5
6433	458	5516	76.9	72	14.74	579.7	0.089	-0.5
6867	502	5863	75.3	78	9.69	579.7	0.122	-0.5

Moreover, in order to capture the P- Δ effect of MD-CBF system, leaning columns connected at each floor by means of truss elements with large stiffness (link beam) were added to the model. These rigid link beams also simulate the rigid diaphragm effect and assure that the beam nodes move horizontally together. Herein, leaning columns are referred to as gravity columns. All columns were assumed continuous over two storeys and pinned at both ends. Furthermore, the seismic mass was applied to each node of CBF columns, however the associated lumped gravity load was applied to all columns (including the leaning columns) and to the beams of CBFs. Gravity columns, link beams and all rigid link segments incorporated in the model were elastic beam-column elements, while brace connections and beam-column connections were modeled

with the *Zero-Length* element. To model the beam-column connections as shear-tab connections, one rotational spring was added in the *Zero-Length* element in the plan of beam bending. According to Liu and Astaneh (2004), the rotational spring shall have the capacity to transfer up to 20% of the plastic bending capacity of the beam to the rigid link ($K_{spring} = 0.20(EI/L)_{beam}$).

4.2.3 Brace-to-frame connection modelling

As previously stated in Section 2, Hsiao et al. (2012) provided an accurate simulation of brace-to-frame connection in OpenSees. In this light, a *Zero-Length* element was added at both brace ends. It connects the brace member to a rigid link, which simulates the remaining part of the gusset plate. As illustrated in Figure 4.7, three rigid end zones were used, hence the rigid part of gusset plate has a minimal in plane deformation relative to other deformation modes of the frame. In addition, the rigid links were simulated using elastic beam-column elements with large stiffness.

Brace connections were modelled by defining two rotational springs and one torsional spring in the *Zero-Length* element (Uriz and Mahin, 2008). Both flexural springs are made of *Steel02* material and the torsional spring is made of elastic material. The first rotational spring is assigned to simulate the out-of-plane deformational stiffness of the connection at the brace end. The rotational stiffness is computed according to Hsiao et al. (2012) and is given below.

$$K_{rotational} = \frac{E}{L_{avg}} \frac{W_w t_g^3}{12} \quad (4.14)$$

The second rotational spring was assigned to control the in-plan buckling. The stiffness of the rotational spring was based upon the geometry and properties of the gusset plate as shown in Figure 4.7 (Hsiao et al., 2012). In this manner, its in-plane flexural stiffness was assigned larger than that of the brace. It is noted that the post-yield stiffness of the rotational spring was considered as 1% of the initial rotational stiffness.

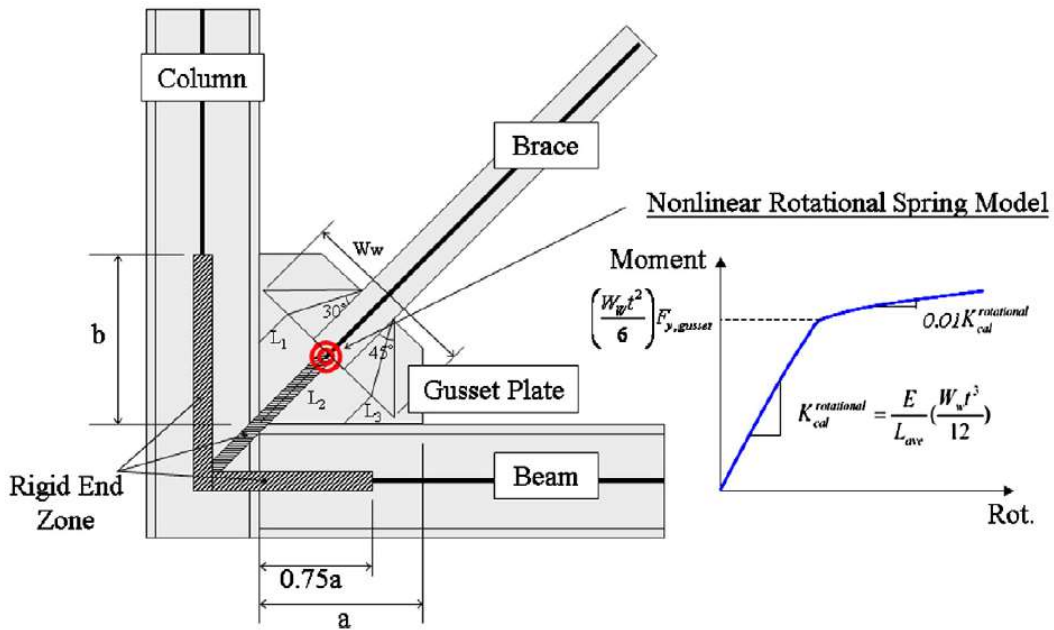


Figure 4.7 Consideration of rigid end zones in OpenSees for CBF models (after Hsiao et al., 2012)

Finally, the torsional spring was assigned to prevent torsion of brace and is defined using equation 4.15. Both rotational springs were made of *Steel02* material and the torsional spring of *Steel01* (elastic material).

$$K_{torsional} = \frac{GJ}{L_{avg}} \text{ where } J = 0.333W_w t_g^3 \quad (4.15)$$

where G is the shear modulus taken as 77000 MPa , L_{ave} is the average value between the L_1 , L_2 , L_3 lengths given below, and J is the torsion constant. The parameters resulted for $2t_g$ linear gusset plate modelling are given in Table 4.29 and for $8t_g$ elliptical gusset plate in Table 4.30.

Table 4.29 Parameters for out-of-plane rotational spring and torsional spring simulating the gusset plate with $2t_g$ model used for HSS braces to frame connections of MD-CBF (E-W)

$L_{ave.}$ (mm)	W_w (mm)	t_g (mm)	$K_{rot-out-of-plane}$ (Nm)	M_p (Nm)	J (mm ⁴)	$K_{tor.}$ (Nm)
418	533	19.05	147022	11289	1227683	226187
485	633	19.05	150362	13392	1456338	231326
497	731	19.05	169403	15473	1682691	260620
459	731	25.40	434450	27508	3988601	668384

Table 4.30 Parameters for out-of-plane rotational spring and torsional spring simulating the gusset plate with $8t_g$ elliptical model for HSS braces to frame connections of MD-CBF (E-W)

$L_{ave.}$ (mm)	W_w (mm)	t_g (mm)	$K_{rot.-out-of-plane}$ (N.m)	M_p (N.m)	J (mm ⁴)	$K_{tor.}$ (Nm)
199	625	15.88	208979	9187	832571	321505
245	607	19.05	284761	12841	1396483	438093
244	706	19.05	333449	14944	1625138	512998
249	724	22.23	531799	20869	2647671	818151

It is noted that, when the same Whitmore width and gusset plate thickness are used for both clearance models, the resulted torsion constant J and plastic moment M_p remain the same as well. However, the difference in the parameter input is seen in $K_{torsional}$ and $K_{rotational}$. Thus, it reinforces the idea that the thickness of gusset plate plays an important role in the performance of CBF than its geometrical shape.

To capture the failure of the gusset plate, in the same *Zero-Length* element, which defines the gusset plate connection on the axial direction, a *MinMax* material was defined. This material returns zero values for the tangent stress by decoupling the brace if the strain or the deformation ever falls below or above certain threshold values. The minimum and the maximum threshold values for the strain/deformation were calculated based on the gusset plate capacity limit previously calculated and the axial stiffness of the gusset plate.

4.3 Nonlinear response of 4-storey hospital building

A dynamic analysis is required to assess the nonlinear response of a structure. According to sentence 4.1.8.3.12(7) in NBCC 2010 Commentary J, the design elastic base shear V_e , must be divided by the product $R_d R_o$ and multiplied by the importance factor I_E to obtain the design base shear, V_d . The previous ETABS Modal Response Spectrum Analysis (MRSA) was scaled in this manner to be on a comparable basis to the static base shear, which is determined by using the ESFP. In this light, the building was subjected to amplified forces and structural members were sized to withstand its effects. The resulting deflections and drifts were elastic due to these adjustments and thus needed to be multiplied by the product $R_d R_o / I_E$, as specified in Sentence 4.1.8.3.12(10), in order to obtain realistic values of anticipated deflections and drifts. Focusing on the importance factor I_E , forces were multiplied by $I_E=1.5$ and the resulting drifts were divided by $I_E=1.5$. Hence, the drift limits recommended by the code are evaluated at the design spectrum (DS) level, which corresponds to $I_E=1$. It is noted that for Site Class C, the design spectrum is the same with the uniform hazard spectrum (UHS).

Designing a post-disaster building, it requires to have bigger structural members to carry the large base shear amplified by I_E . In this light, its fundamental period is shortened compared to a similar building designed with $I_E=1$. During an earthquake, the amount of energy that a building attracts is dependent on its period and site conditions. Hence, it is not directly related to the importance factor, but it is dependent on its resulting period. In other words, during an earthquake, the post-disaster building will be subjected to the same level of ground acceleration as the normal importance category building but it would attract more energy due to its shorter period. Under this condition, the interstorey drifts of both structures must be below the allowable drift limits. When a larger than expected seismic event occurs, post-disaster buildings have the reserve capacity to withstand the shaking because $I_E=1.5$ was considered in design. In this study, the behaviour of post-disaster buildings subjected to higher than code-level earthquakes is also examined.

There are no straight-forward guidelines on time-history analysis for post-disaster buildings with higher importance factor. On one hand, to determine the expected deformation under a code level earthquake, an OpenSees model was created and subjected to ground motions that are scaled to fit the DS for Victoria, which corresponds to $I_E=1$. It is worth noting that CBF members were

designed to respond to the base shear computed with $I_E = 1.5$. On the other hand, to verify the strength reserve capacity of the building, the structure was also subjected to ground motions scaled to fit the DS amplified by $I_E=1.5$. It is recommended that structural members and connections do not fail under both scenarios. However, the structure is permitted to have interstorey drift larger than the allowable drift limit of $1\%h_s$ when subject to code-level ground motions amplified by $I_E=1.5$. Herein, it is also proposed to limit the peak of maximum interstorey drift to $2.0\%h_s$, while the Mean should be $\leq 1\%h_s$ for post-disaster buildings.

4.3.1 Ground motion selection and scaling

To analyze the seismic behaviour of low-rise braced frames located in high seismic zone (e.g. Victoria, BC), a suite of ground motions was selected and scaled in agreement with the ASCE/ SEI 2007 procedure in order to fit the design spectrum for Victoria.

Several historic ground motions respond to the intensity demand for Victoria. However, the most important factor in selecting ground motions for scaling to a target spectrum is the spectral shape over the period range of interest (currently $0.2T_1$ to $1.5T_1$ in ASCE/SEI 7-10). The other considerations are the earthquake magnitude M_w , site-to-source distance r , and local site conditions. Selecting a pair of motions whose geometric mean spectral shape is similar to the target spectrum minimizes the need for scaling and modification. Magnitude and distance will affect strong motion duration, which may be important for buildings with components that will degrade under cyclic loading. If the mathematical model used for analysis cannot capture cyclic degradation, there is little need to consider strong motion duration in the selection process. It is noted that for near-fault ground motions, the two most important factors are spectral shape and presence of velocity pulses. Velocity pulses are present in many near-fault ground motion recordings, especially in the forward directivity region (Baker, 2019). However, no near-fault ground motions were selected in this analysis. The 10 crustal ground motions selected are given in Table 4.31.

Table 4.31 Ground motion selection and characteristics

Event No.	Station	V_s (m/s)	R_{typ} (km)	R_{rupt} (km)	Comp ($^{\circ}$)	PHA (g)	PHV (m/s)	PHA (m/s ²)	PHV/PHA	t_D (s)	T_p	T_m
963	Castaic, Old Ridge Route	450	44	21	90	0.57	0.52	5.59	0.09	9.08	0.26	0.54
986	LA - Brentwood VA Hospital	417	25	23	195	0.19	0.24	1.86	0.13	11.43	0.24	0.63
1006	LA - UCLA Grounds	398	25	22	90	0.28	0.22	2.75	0.08	11.30	0.22	0.34
1039	Moorpark - Fire Sta	405	36	25	180	0.29	0.20	2.84	0.07	14.22	0.26	0.47
57	Castaic, Old Ridge Route	450	29	23	291	0.27	0.26	2.63	0.10	15.35	0.20	0.48
767	Gilroy Array #3	350	36	13	0	0.56	0.36	5.49	0.07	6.37	20.00	0.37
787	Palo Alto - SLAC Lab	425	54	31	360	0.28	0.29	2.75	0.11	11.58	0.30	0.65
796	SF-Presidio	595	99	77	90	0.20	0.32	1.96	0.16	8.72	0.48	0.81
739	Anderson Dam (Downstream)	489	20	20	250	0.25	0.20	2.45	0.09	10.40	0.20	0.46
1077	St Monica	450	31	31	360	0.37	0.25	3.63	0.07	12.7	0.12	0.51

In general, there is greater record-to-record variability. Design practice as per ASCE/SEI 7-10, requires the use of a minimum of seven ground motions for response-history analysis. If seven are used for analysis, the Mean response can be used for component checking. Assuming that ground motions are selected with explicit consideration of spectral shape and the mathematical model can trace cyclic component behaviors accurately over the expected ranges of inelastic response, no less than seven ground motions should be used to estimate values of mean response.

The selected records for Victoria are from moderate to large crustal earthquakes of magnitude varying from M_w 6.6 to M_w 6.9 that occurred on the west coast of North America. The 10 records given in Table 4.31 were selected from the Peer Ground Motion Database website (www.peer.berkeley.edu) such that their shear wave velocity corresponds to Class C soil. To match the design spectrum for Victoria, all records were scaled according to ASCE/SEI07-10 requirements. To scale the ground motions, the methodology proposed by Reyes and Kalkan (2011) was employed. As illustrated in Fig. 4.8, the mean of the 5% damped response spectra of the 10 scaled records matches or is above the design spectrum in any points over the interval $[0.2T_1 - 1.5T_1]$. In addition, the same suite of ground motions was scaled to match the design spectrum for Victoria after it was amplified by importance factor $I_E=1.5$. The scale factor for each ground motion is summarized in Table 4.32.

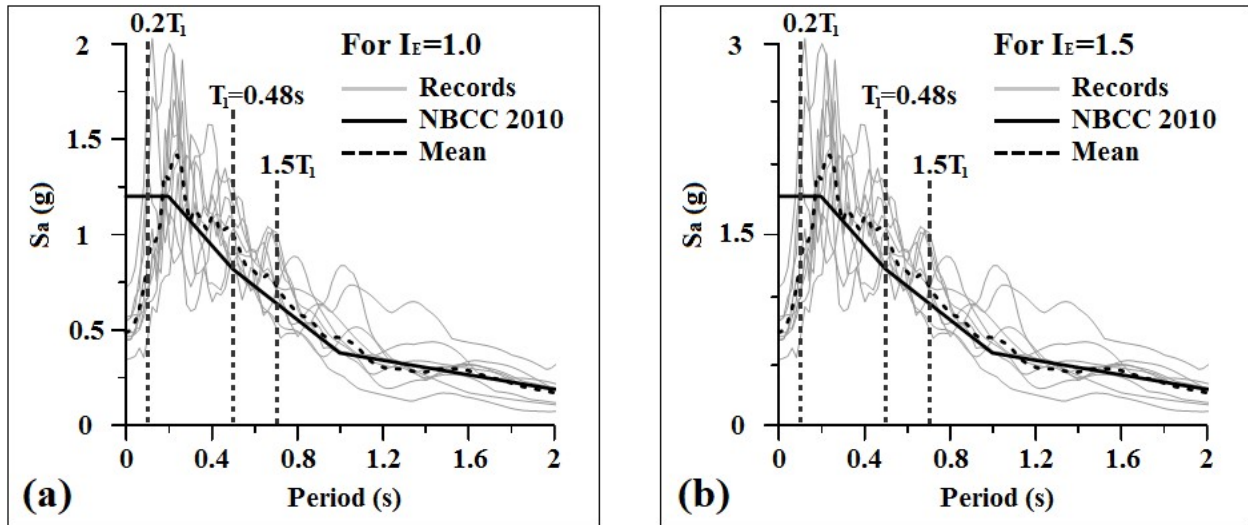


Figure 4.8 Design spectrum and 5% damped absolute acceleration spectra of the scaled ground motions for: a) $I_E = 1.0$ and b), $I_E = 1.5$

Table 4.32 Ground motion scaling factor to match the design level

GM	Event	Mw	Station	S. F. for $I_E=1$	S. F. for $I_E=1.5$
57	Feb. 9, 1971 San Fernando	6.6	Castaic, Old Ridge Route	1.85	2.78
767	Oct. 18, 1989 Loma Prieta	6.9	Gilroy Array #3	1.68	2.52
787	Oct. 18, 1989 Loma Prieta	6.9	Palo Alto - SLAC Lab	0.98	1.47
796	Oct. 18, 1989 Loma Prieta	6.9	SF - Presidio	1.91	2.87
739	Oct. 18, 1989 Loma Prieta	6.9	Anderson Dam (Downstream)	1.95	2.93
963	Jan. 17, 1994 Northridge	6.7	Castaic, Old Ridge Route	0.85	1.28
986	Jan. 17, 1994 Northridge	6.7	LA - Brentwood VA Hospital	1.98	2.97
1006	Jan. 17, 1994 Northridge	6.7	LA - UCLA Grounds	1.94	2.91
1039	Jan. 17, 1994 Northridge	6.7	Moorpark - Fire Station	1.84	2.76
1077	Jan. 17, 1994 Northridge	6.7	St Monica	1.68	2.52

4.3.2 Nonlinear response of building at the design level $I_E=1.0$

In order to ensure that the building model in OpenSees is reliable, it is recommended to compare the fundamental building period of the first mode T_1 with the dynamic period obtained from ETABS. The fundamental period of the building in the E-W direction is given in Table 4.33.

Table 4.33 Fundamental period T_1 comparison between different software models

Table 4.33 Software model	$T_{1,E-W}$ (s)
ETABS	0.483
OpenSees –MD-CBF with Linear gusset plate model	0.5157
OpenSees –MD-CBF with Elliptical gusset plate model	0.5158

The obtained periods are relatively close to one another given the fact that in ETABS, connections are often overestimated by a full pin connection or a fixed connection. It is noted that for both clearance models, in OpenSees, the first mode period is nearly identical. Hence, in a seismic event, both structures are expected to attract the same amount of forces as one another.

The hospital building model was subjected to 10 ground motions given in Table 4.31. Then, a comparative study between the two models of brace-to-frame gusset plates (e.g. $2t_g$ linear and $8t_g$ elliptical clearance) was carried out. To emphasise the differences, the selected parameters were: i) the interstorey drift, ii) the residual interstorey drift, iii) floor acceleration and iv) the energy dissipated by braces illustrated by means of hysteresis loops.

The maximum interstorey drift was recorded for each ground motion scaled at their specific scale factor at code level and the results are given in Table 4.34 and 4.35 for $2t_g$ linear and $8t_g$ elliptical clearance model, respectively.

Table 4.34 Distribution of interstorey drift for MD-CBF with $2t_g$ linear clearance gusset plate model under 10 GMs scaled at code level considering $I_E=1.0$ (E-W)

Distribution of interstorey drift at code level with $I_E=1$ for MD-CBF with $2t_g$ linear band gusset plate											
St.	H	GM	GM	GM	GM	GM	GM	GM	GM	GM	GM
	(m)	(% h_s)	(% h_s)	(% h_s)	(% h_s)	(% h_s)	(% h_s)	(% h_s)	(% h_s)	(% h_s)	(% h_s)
4	18.2	0.571	0.692	0.653	0.418	0.804	0.675	0.626	0.421	0.569	0.680
3	13.8	0.646	0.834	0.622	0.541	0.808	0.656	0.635	0.460	0.563	0.881
2	9.4	0.345	0.549	0.404	0.448	0.414	0.381	0.393	0.389	0.478	0.494
1	5.0	0.512	0.480	0.457	0.636	0.453	0.436	0.406	0.547	0.660	0.429

In all situations, the maximum interstorey drift is smaller than the allowable maximum interstorey drift of $1\%h_s$ for post-disaster buildings at code level. In the following table, the values in red represent the interstorey drifts from $8t_g$ elliptical model that exceeds the drift obtained from the previous $2t_g$ linear model.

Table 4.35 Distribution of interstorey drift for MD-CBF with $8t_g$ elliptical clearance gusset plate model under 10 GMs scaled at code level considering $I_E=1.0$ (E-W)

Distribution of interstorey drift at code level with $I_E=1$ for MD-CBF with $8t_g$ elliptical band gusset plate											
St.	H	GM	GM	GM	GM	GM	GM	GM	GM	GM	GM
	(m)	(% h_s)	(% h_s)	(% h_s)	(% h_s)	(% h_s)	(% h_s)	(% h_s)	(% h_s)	(% h_s)	(% h_s)
4	18.2	0.570	0.697	0.653	0.405	0.806	0.670	0.635	0.415	0.571	0.684
3	13.8	0.663	0.853	0.627	0.548	0.824	0.663	0.644	0.466	0.578	0.997
2	9.4	0.342	0.539	0.396	0.437	0.421	0.382	0.390	0.383	0.476	0.546
1	5.0	0.516	0.482	0.465	0.647	0.449	0.428	0.402	0.547	0.648	0.460

It is apparent that the $8t_g$ elliptical gusset plate model does not necessarily give a larger interstorey drifts than the $2t_g$ linear. In order to further investigate the difference in drifts, the Mean, the Mean+SD and the maximum drifts of all ground motions is given in Table 4.36, where SD is the standard deviation. Meanwhile, the interstorey drift envelope resulted from the building response under the 10 scaled ground motions is depicted in Fig. 4.9 using the Mean and Mean+SD.

Table 4.36 Distribution of Mean, Mean+SD and Max. interstorey drift of MD-CBF response (E-W) obtained at code level considering $I_E=1.0$

Mean, Mean+SD and Max. interstorey drifts comparison at code level with $I_E=1$							
St.	H	Mean (% h_s)		Mean+SD (% h_s)		Maximum (% h_s)	
		(m)	$2t_g$ linear	$8t_g$ elliptical	$2t_g$ linear	$8t_g$ elliptical	$2t_g$ linear
4	18.2	0.611	0.611	0.739	0.736	0.804	0.806
3	13.8	0.664	0.686	0.809	0.846	0.881	0.997
2	9.4	0.430	0.431	0.488	0.500	0.549	0.546
1	5.0	0.502	0.504	0.589	0.590	0.660	0.648

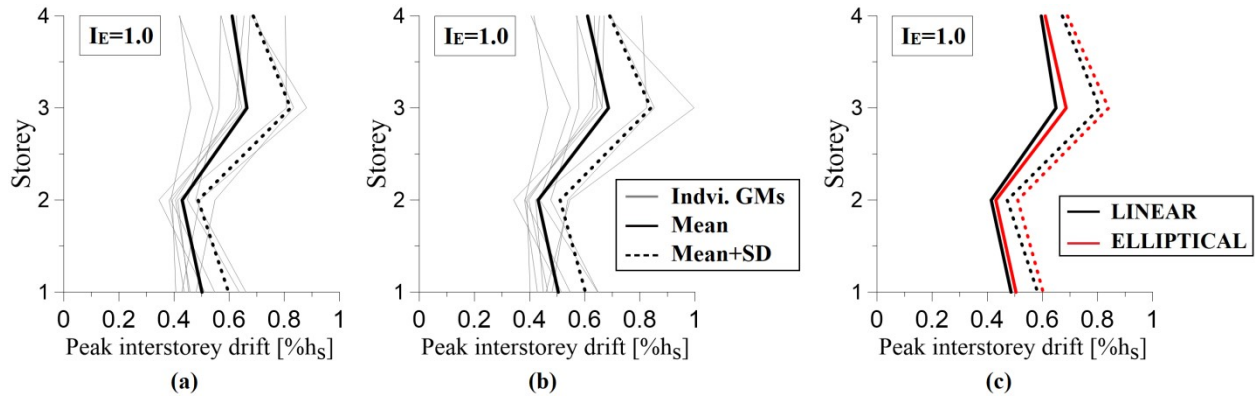


Figure 4.9 Distribution of interstorey drift across the building height: a) $2t_g$ linear gusset plate model, b) $8t_g$ elliptical gusset plate model and c) Mean and Mean+SD comparison between the 2 models

The recorded peak drift envelopes for each ground motions are almost identical for both models. In both cases, the largest peak interstorey drift occurred on the 3rd floor for all ground motions. Moreover, the drifts recorded in the case of $8t_g$ clearance model are slightly larger than those that resulted for the $2t_g$ linear gusset plate model at that specific floor. However, the difference in drifts is at most 2.75%, which is almost negligible. Hence, further investigation is required to assess the difference in performance.

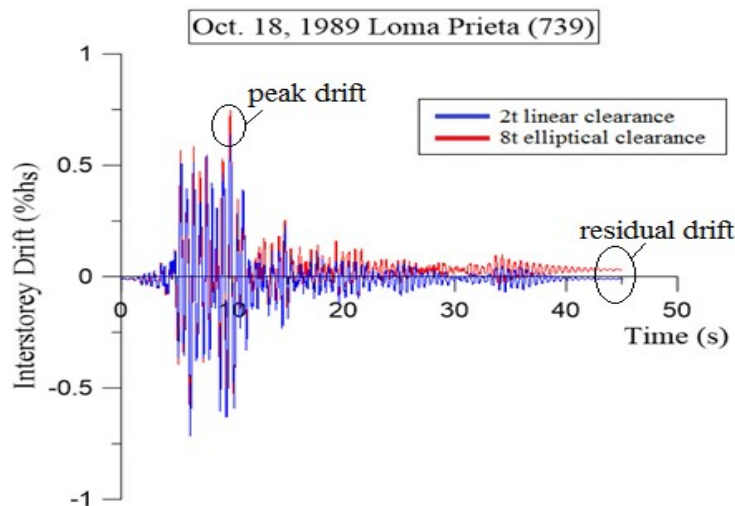


Figure 4.10 Time-history response of MD-CBF subjected to Loma Prieta ground motion #739 scaled at code level considering $I_E=1.0$

As shown in Fig. 4.10, the time-history series of interstorey drift is recorded at the 3rd floor under the #739 Loma Prieta earthquake. As depicted, the residual drift is slightly larger for the $8t_g$ clearance model than the $2t_g$ model. The peak in demand occurred at $t = 9.38$ s. The resulted residual interstorey drifts for both clearance models and for all ground motions are given in Tables 4.37 and 4.38.

In order to capture the residual interstorey drifts in OpenSees, the duration of the ground motion accelerograms were increased to allow the building to behave in free vibrations until the drift converges. In general, adding 20 to 30 seconds of zero amplitude accelerogram in time steps at the end of the ground motion is sufficient to converge the residual drifts. It is also noted that it is recommended to add 10 time steps with no excitation at the beginning of the ground motion to allow the gravity loads to settle prior to the earthquake simulation.

Table 4.37 Distribution of residual drift along the building height for MD-CBF with $2t_g$ linear gusset plate model under 10 GMs scaled at code level considering $I_E = 1.0$

Distribution of residual drift at code level with $I_E=1$ for MD-CBF with $2t_g$ linear band gusset plate											
St.	H	GM	GM	GM	GM	GM	GM	GM	GM	GM	GM
	(m)	(%h _s)	(%h _s)	(%h _s)	(%h _s)	(%h _s)	(%h _s)	(%h _s)	(%h _s)	(%h _s)	(%h _s)
4th	18.2	0.044	0.075	0.064	0.023	0.104	0.044	0.047	0.025	0.014	0.099
3rd	13.8	0.022	0.153	0.063	0.012	0.071	0.046	0.054	0.007	0.009	0.131
2nd	9.4	0.008	0.070	0.025	0.045	0.019	0.031	0.039	0.021	0.043	0.057
GF	5.0	0.077	0.029	0.055	0.086	0.029	0.018	0.028	0.068	0.047	0.019

Table 4.38 Distribution of residual drift along the building height for MD-CBF with $8t_g$ elliptical gusset plate model under 10 GMs scaled at code level considering $I_E = 1.0$

Distribution of residual drift at code level with $I_E=1$ for MD-CBF with $8t_g$ elliptical band gusset plate											
ST	H	GM	GM	GM	GM	GM	GM	GM	GM	GM	GM
	(m)	(%h _s)	(%h _s)	(%h _s)	(%h _s)	(%h _s)	(%h _s)	(%h _s)	(%h _s)	(%h _s)	(%h _s)
4th	18.2	0.050	0.081	0.069	0.021	0.114	0.052	0.054	0.025	0.015	0.107
3rd	13.8	0.026	0.171	0.068	0.019	0.078	0.057	0.063	0.011	0.013	0.125
2nd	9.4	0.009	0.069	0.023	0.042	0.022	0.031	0.038	0.021	0.039	0.060
GF	5.0	0.087	0.036	0.060	0.092	0.029	0.016	0.028	0.075	0.044	0.008

The $8t_g$ elliptical model is prone to have larger residual drifts than the code recommended $2t_g$ clearance gusset plate model, as shown in red in Table 4.38. The largest difference between them is about 57%, which is significant, however the highest value of $0.17\%h_s$ does not exceed the suggested $0.5\%h_s$ residual drift limit. For comparison, the Mean, the Mean+SD and the Maximum residual drifts response resulted for all GMs excitations is given in Table 4.39, while the permanent drift envelope resulted from the building response under the 10 scaled ground motions are depicted in Fig. 4.11 using the Mean and Mean+SD.

Table 4.39 Distribution of Mean, Mean+SD and Max residual drifts of MD-CBF (E-W) response along the building height under GMs scaled at code level considering $I_E=1.0$

Mean, Mean+SD, Max. residual interstorey drifts response at code level with $I_E=1$							
St.	Height (m)	Mean ($\%h_s$)		Mean+SD ($\%h_s$)		Maximum ($\%h_s$)	
		$2t_g$ linear	$8t_g$ elliptical	$2t_g$ linear	$8t_g$ elliptical	$2t_g$ linear	$8t_g$ elliptical
4th	18.2	0.054	0.059	0.085	0.093	0.104	0.114
3rd	13.8	0.057	0.063	0.107	0.115	0.153	0.171
2nd	9.4	0.036	0.035	0.055	0.054	0.070	0.069
GF	5.0	0.046	0.048	0.071	0.077	0.086	0.092

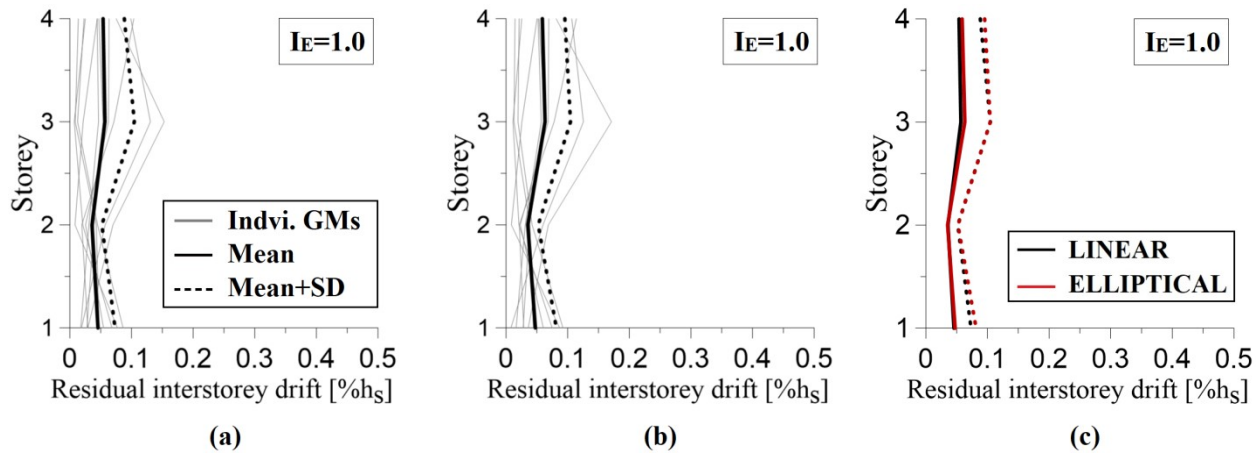


Figure 4.11 Residual drift response of MD-CBF with: a) $2t_g$ linear gusset plate model and b) $8t_g$ elliptical gusset plate model. c) Mean and Mean+SD comparison between the 2 models

The largest residual interstorey drift does not necessarily occur at a specific floor for all ground motions. The first floor experiences the largest permanent drifts under the ground motion#57. The

2nd and 3rd floor experience the largest permanent drifts under the ground motion #986. The 4th floor experiences the largest permanent drift under the ground motion #1077. However, similar to peak interstorey drifts, the largest average of residual drifts occurs at the 3rd floor. In general, the permanent drifts recorded in case of MD-CBF with $8t_g$ clearance gusset plate model are larger than that resulted for the $2t_g$ linear model. The increase in permanent drifts is at most 57%, which occurs at the 3rd floor under GM #986. It is noted that the overall shape of the permanent drift envelope does indicate that the $8t_g$ elliptical model can better distribute the residual drifts over the height of the building. However, the model with $8t_g$ shows slightly larger permanent drift than the model with $2t_g$ clearance. This phenomenon is further investigated in the following sections.

The maximum floor accelerations were also recorded for each ground motion scaled at their specific scale factor at code level and are given in Tables 4.40 and 4.41 for MD-CBF building with $2t_g$ linear and $8t_g$ elliptical clearance gusset plate model, respectively.

Table 4.40 Distribution of floor acceleration along the height of MD-CBF with $2t_g$ gusset plate model resulted under 10 GMs scaled at code level considering $I_E=1.0$

Distribution of floor acceleration resulted for MD-CBF with $2t_g$ linear clearance gusset plate under 10 GMs scaled at code level considering $I_E=1$											
ST	H	GM	GM	GM	GM	GM	GM	GM	GM	GM	GM
	(m)	(g)	(g)	(g)	(g)	(g)	(g)	(g)	(g)	(g)	(g)
4th	18.2	0.95	0.85	0.98	0.89	1.00	0.94	0.96	0.83	1.03	0.91
3rd	13.8	0.87	0.75	0.77	0.71	0.95	0.65	0.96	0.70	1.19	0.95
2nd	9.4	0.75	0.68	0.88	0.77	0.95	0.74	1.21	0.76	1.23	0.73
GF	5.0	0.60	0.52	0.64	0.73	0.84	0.72	0.86	0.69	0.91	0.67

In the following table, the values in red represent the floor accelerations from $8t_g$ elliptical model that exceeds the values from the previous $2t_g$ linear model.

Table 4.41 Distribution of floor acceleration for MD-CBF with $8t_g$ gusset plate model resulted under 10 GMs scaled at code level considering $I_E=1.0$

Floor acceleration resulted for MD-CBF with $8t_g$ elliptical band gusset plate under GMs scaled at code level considering $I_E=1$											
ST	H (m)	GM 739 (g)	GM 986 (g)	GM 1006 (g)	GM 57 (g)	GM 1077 (g)	GM 1039 (g)	GM 767 (g)	GM 963 (g)	GM 796 (g)	GM 787 (g)
4th	18.2	0.96	0.87	0.99	0.90	1.00	0.95	0.98	0.85	1.04	0.90
3rd	13.8	0.87	0.75	0.79	0.70	0.97	0.66	0.96	0.71	1.20	0.95
2nd	9.4	0.75	0.68	0.88	0.76	0.95	0.73	1.23	0.75	1.24	0.74
GF	5.0	0.62	0.54	0.65	0.74	0.86	0.71	0.86	0.68	0.90	0.68

It is apparent that the $8t_g$ elliptical model does not necessarily show larger floor acceleration than the $2t_g$ linear model. In addition, the maximum floor acceleration does not always occur on a specific storey for all ground motions. In order to further investigate the difference in acceleration, the Mean, the Mean+SD and the Maximum acceleration resulted for all ground motions scaled at the code level considering $I_E=1.0$ is given in Table 4.42. Meanwhile, the Mean and Mean+SD of the floor acceleration envelope resulted from the building response under the 10 scaled ground motions and a comparison between the model with $2t_g$ and $8t_g$ are depicted in Fig. 4.12.

Table 4.42 Distribution of Mean, Mean+SD and Max. floor acceleration of MD-CBF response when subjected to GMs scaled at code level considering $I_E=1.0$

Mean, Mean+SD and Max. floor acceleration response of MD-CBF scaled at code level and $I_E=1$							
St.	Height (m)	Mean (g)		Mean+SD (g)		Maximum (g)	
		$2t_g$ linear	$8t_g$ elliptical	$2t_g$ linear	$8t_g$ elliptical	$2t_g$ linear	$8t_g$ elliptical
4th	18.2	0.94	0.95	0.99	1.00	1.03	1.04
3rd	13.8	0.85	0.86	0.96	0.97	1.19	1.20
2nd	9.4	0.87	0.87	1.10	1.11	1.23	1.24
GF	5.0	0.72	0.72	0.85	0.86	0.91	0.90

In general, the accelerations recorded for MD-CBF with $8t_g$ clearance gusset plate model are larger than that of MD-CBF with $2t_g$ linear gusset plate model. However, the difference in floor acceleration is at most 1.81%, which is almost negligible. The largest peak floor accelerations occur either at the 3rd floor or at the roof. Thus, both systems appear to behave almost identically.

Under the same scaled ground motion, when one model undergoes larger interstorey drifts than the other, it reaches those thresholds within the same time interval. In this manner, larger floor acceleration may be expected on that specific floor. Nonetheless, the maximum floor acceleration does not occur at the storey with the largest interstorey drift.

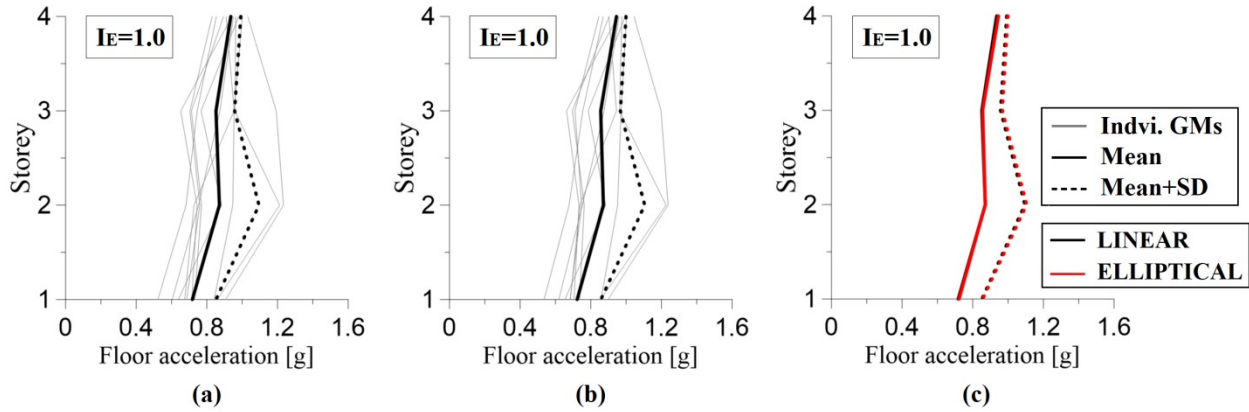


Figure 4.12 Distribution of floor acceleration along the MD-CBF height with a) $2t_g$ linear clearance gusset plate model, b) $8t_g$ elliptical clearance gusset plate model and c) Mean and Mean+SD comparison between the 2 models

It was observed that the maximum floor acceleration and maximum interstorey drift occur at the same floor under 3 ground motions: GM #787, GM #1006 and GM #1077. The behaviour of all HSS braces subjected to ground motion GM #787 is investigated by means of hysteresis loops plotted in Figure 4.13. At each floor, the left brace was first to reach buckling in compression. On all storeys excepting the 2nd floor, the right braces experience their first yielding around the time step of 9.9s when the left braces buckle a second time at a similar time of 9.86s. At the 2nd floor, the left brace buckles first at 9.86s, which is then instantly followed by the yielding of the right brace at 9.93. Under GM #787, both MD-CBFs detailed with $2t_g$ and $8t_g$ clearance gusset plate models experience their first buckling and first yielding of braces at the same time. As strain is accumulated in the HSS braces, the difference in the hysteretic loop is further pronounced. At the upper 2 floors, the braces with $8t_g$ elliptical gusset plate model undergo through larger axial deformation and hence, are required to dissipate a larger amount of energy to mitigate damages as shown in Figure 4.13. However, the opposite is true on the lower 2 floors.

Although, the peak drifts do occur under GM #787, the difference in the hysteretic loop is too small and negligible to make any valuable conclusions.

The braces of the 3rd floor show the largest difference in axial deformation between the two models when subjected to GM #739 ground motion. In this light, the hysteresis loops of the 3rd floor braces obtained under the #739 Loma Prieta record are investigated and plotted in Figure 4.14.

Under both records, the left brace was the first that buckled in compression. Under the #739 record, the left brace buckles first at $t = 5.12$ s, while the right brace reached buckling at the same time ($t = 5.38$ s) at which the left brace reached yielding in tension. Then, the right brace reached yielding in tension simultaneously with the maximum deflection in compression experienced by the left brace at $t = 6.20$ s. Similarly, the right brace experiences the maximum deflection in compression at $t = 9.38$ s. Simultaneously, at $t = 9.38$ s, the left brace undergoes the largest tensile axial deformation.

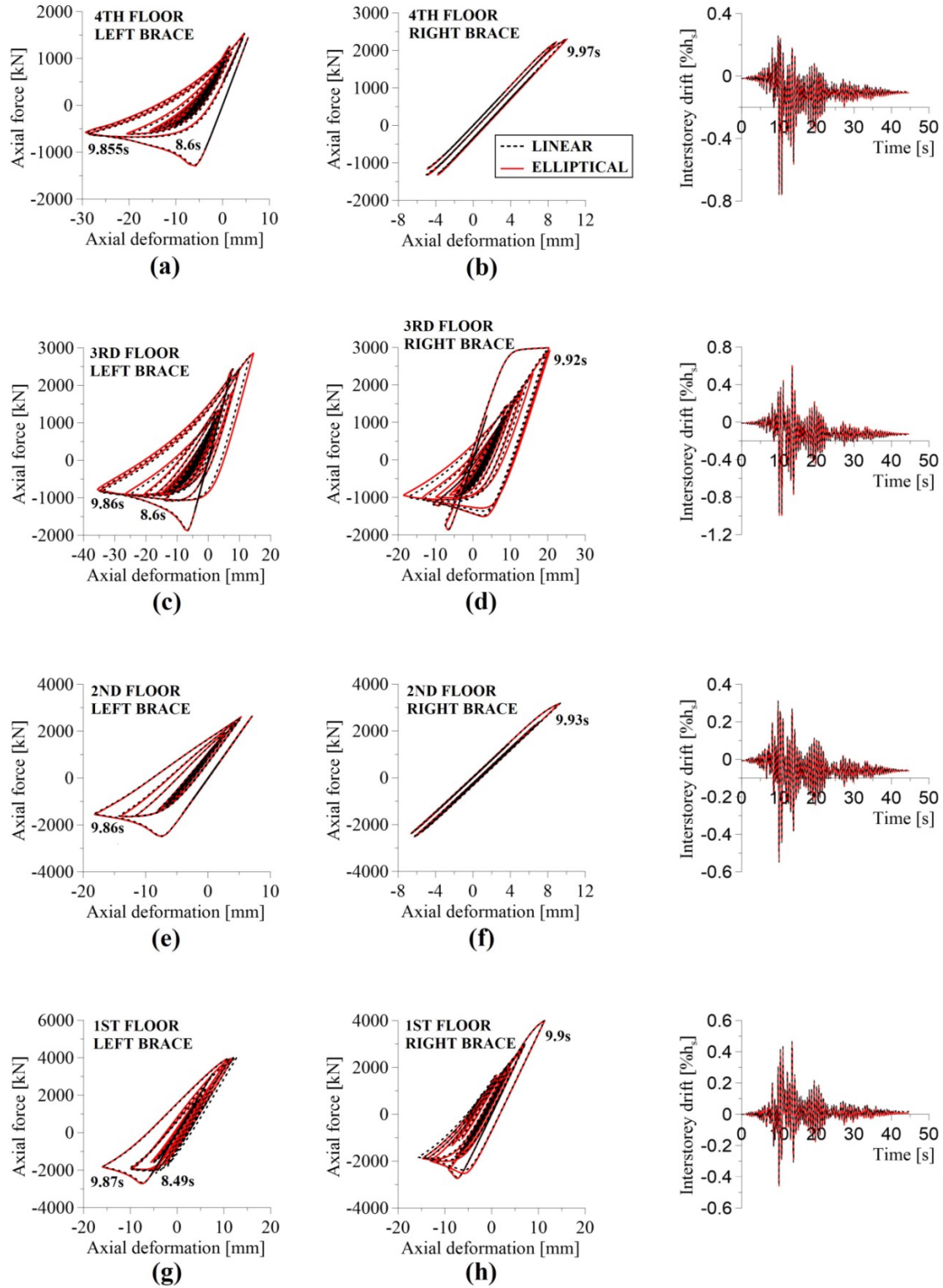


Figure 4.13 Hysteretic loops of braces of MD-CBF (E-W) under GM #787 scaled at code level considering $I_E=1$

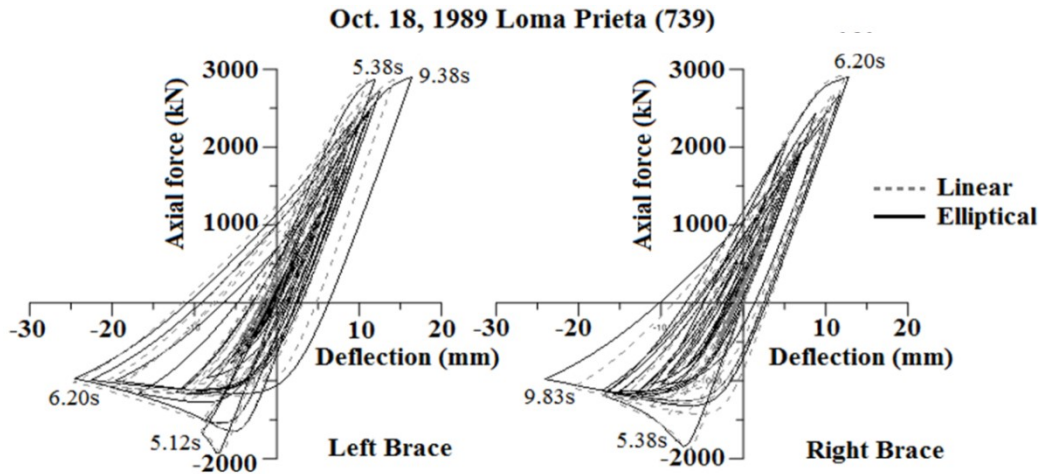


Figure 4.14 Hysteresis loops of the 3rd floor braces resulted under: a) #739 Loma Prieta record, b) #1006 Northridge record scaled to code level considering $I_E=1$

4.3.3 Nonlinear response of CBF (E-W) corresponding to design spectrum amplified by $I_E=1.5$

These events represent earthquakes that would be more severe than the earthquakes that are likely to occur (2% in 50 years), and therefore, are even more unlikely to occur. As aforementioned, post-disaster buildings are expected to be able to perform adequately under larger demand than the code level earthquakes. The SFRS must be capable of withstanding the amplified seismic forces ($I_E=1.5$) while demonstrating, in terms of drifts and accelerations, that it can keep the building operational under these increased demands.

The maximum interstorey drifts were recorded for each ground motion scaled at their specific scale factor corresponding to $I_E=1.5$ and are given in Tables 4.43 and 4.44 for $2t_g$ linear and $8t_g$ elliptical clearance model, respectively.

The drifts are not always below the allowable drift limit of $1\%h_s$ set by the code for post-disaster buildings for both clearance models. The code requires that the Mean of the peak interstorey drifts to be below the $1\%h_s$. According to Table 4.45, the Mean of peak interstorey drift is equal or less than $1\%h_s$ at all floors. Under all ground motions, the maximum interstorey drift occurs at the 3rd floor except for #GM787, where the peak drift is on the 1st floor.

Table 4.43 Distribution of interstorey drift recorded for MD-CBF (E-W) with $2t_g$ linear gusset plate model under 10 GMs scaled at code level considering $I_E=1.5$

Distribution of interstorey drift obtained at code level amplified with $I_E=1.5$ for MD-CBF with $2t_g$ linear clearance gusset plate											
St.	H	GM	GM	GM	GM	GM	GM	GM	GM	GM	GM
	(m)	(%h _s)	(%h _s)	(%h _s)	(%h _s)	(%h _s)	(%h _s)	(%h _s)	(%h _s)	(%h _s)	(%h _s)
4	18.2	0.573	0.668	0.945	0.545	1.010	0.782	0.643	0.770	0.342	0.772
3	13.8	1.038	0.734	0.996	1.084	1.526	0.830	0.953	1.229	0.347	1.272
2	9.4	0.476	0.692	0.408	0.468	0.562	0.451	0.369	0.587	0.471	0.574
1	5.0	0.593	1.104	0.518	0.818	0.551	0.567	0.409	0.842	1.761	0.808

Table 4.44 Distribution of interstorey drift recorded for MD-CBF (E-W) with $8t_g$ elliptical gusset plate model under 10GMs scaled at code level considering $I_E=1.5$

Distribution of interstorey drift at code level with $I_E=1.5$ for MD-CBF with $8t_g$ elliptical band gusset plate											
St.	H	GM	GM	GM	GM	GM	GM	GM	GM	GM	GM 787
	(m)	(%h _s)	(%h _s)	(%h _s)	(%h _s)	(%h _s)	(%h _s)	(%h _s)	(%h _s)	(%h _s)	(%h _s)
4	18.2	0.572	0.673	0.945	0.528	1.014	0.776	0.651	0.760	0.344	0.776
3	13.8	1.065	0.752	1.005	1.099	1.556	0.839	0.968	1.245	0.357	1.439
2	9.4	0.472	0.680	0.400	0.456	0.572	0.452	0.366	0.579	0.469	0.634
1	5.0	0.598	1.109	0.527	0.833	0.546	0.557	0.406	0.841	1.728	0.867

Table 4.45 Mean, Mean+SD and Max interstorey drift of MD-CBF response at code level considering $I_E=1.5$

Mean, Mean+SD and Max interstorey drifts comparison at code level with $I_E=1.5$							
St.	Height (m)	Mean (%h _s)		Mean+SD (%h _s)		Maximum (%h _s)	
		$2t_g$ linear	$8t_g$ elliptical	$2t_g$ linear	$8t_g$ elliptical	$2t_g$ linear	$8t_g$ elliptical
4th	18.2	0.705	0.704	0.901	0.901	1.010	1.014
3rd	13.8	1.001	1.033	1.324	1.377	1.526	1.556
2nd	9.4	0.506	0.508	0.603	0.611	0.692	0.680
GF	5.0	0.797	0.801	1.193	1.190	1.761	1.728

The recorded peak drift envelopes are almost identical for both clearance models under all ground motions. The overall shape of the drift envelope plotted in Fig. 4.15 is similar with that resulted when $I_E=1$.

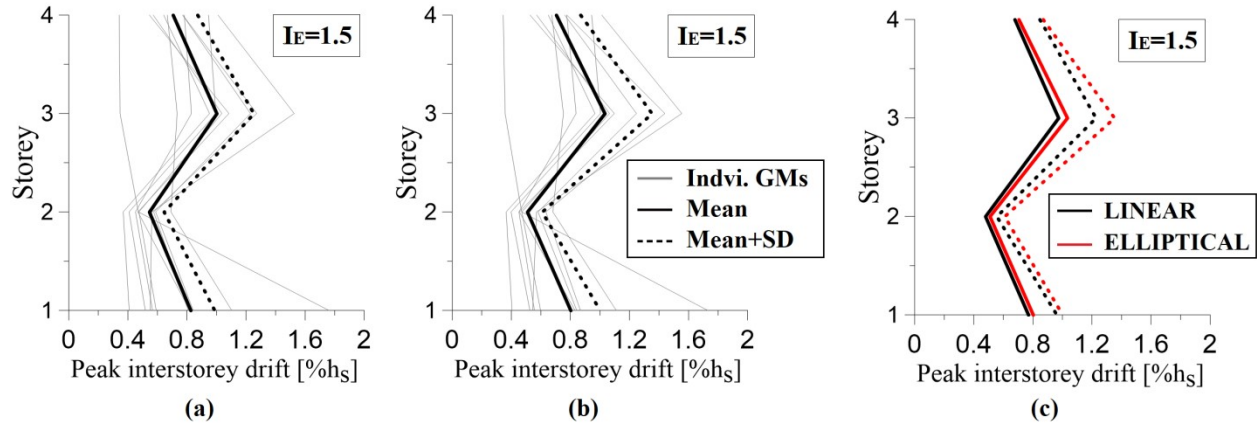


Figure 4.15 Distribution of interstorey drift: a) MD-CBF with $2t_g$ linear gusset plate model, b) MD-CBF with $8t_g$ elliptical gusset plate model and c) Mean and Mean+SD comparison between the 2 models

As previously mentioned, these post-disaster buildings experience a peak of Mean interstorey drift of $1\%h_s$, which is within the code limit when ground motions were amplified by $I_E=1.5$. However, to ensure its structural integrity during such events, it is recommended to limit the peak of Max interstorey drift to $2.0\%h_s$ and the residual drift to $0.5\%h_s$ when post-disaster building is subjected to ground motions scaled to the amplified design spectrum ($I_E=1.5$).

The maximum permanent drifts were recorded for each ground motion scaled at their specific scale factor corresponding to $I_E=1.5$ and are provided in Tables 4.46 and 4.47 for $2t_g$ linear and $8t_g$ elliptical clearance model, respectively. Similar to the analysis done with $I_E=1$, the $8t_g$ elliptical model is prone to have larger residual drifts than the case with $2t_g$ clearance gusset plate model. The overall shape of the residual drift envelope is similar to that obtained when ground motions were amplified by $I_E=1$, but the gap in the response between the two clearance model is widened. This may suggest that by further increasing the seismic demand, the potential difference in behaviour can be further investigated.

Table 4.46 Distribution of residual drift of MD-CBF with $2t_g$ linear gusset plate model under 10 GMs scaled at code level considering $I_E=1.5$

Distribution of residual interstorey drift at code level with $I_E=1.5$ for MD-CBF with $2t_g$ linear band gusset plate											
St.	H	GM	GM	GM	GM	GM	GM	GM	GM	GM	GM
	(m)	(%h _s)	(%h _s)	(%h _s)	(%h _s)	(%h _s)	(%h _s)	(%h _s)	(%h _s)	(%h _s)	(%h _s)
4	18.2	0.029	0.075	0.065	0.002	0.128	0.055	0.012	0.055	0.009	0.090
3	13.8	0.138	0.097	0.021	0.161	0.194	0.087	0.002	0.093	0.007	0.221
2	9.4	0.033	0.124	0.019	0.024	0.061	0.040	0.004	0.009	0.088	0.046
1	5.0	0.006	0.103	0.079	0.113	0.014	0.004	0.032	0.064	0.272	0.063

Table 4.47 Distribution of residual drift of MD-CBF with $8t_g$ elliptical gusset plate model under 10 GMs scaled at code level considering $I_E=1.5$

Residual interstorey drift of MD-CBF with $8t_g$ elliptical clearance gusset plate under GMs scaled at code level with $I_E=1.5$											
St.	H	GM	GM	GM	GM	GM	GM	GM	GM	GM	GM
	(m)	(%h _s)	(%h _s)	(%h _s)	(%h _s)	(%h _s)	(%h _s)	(%h _s)	(%h _s)	(%h _s)	(%h _s)
4	18.2	0.032	0.082	0.070	0.002	0.140	0.065	0.014	0.056	0.009	0.097
3	13.8	0.165	0.108	0.023	0.250	0.212	0.107	0.003	0.145	0.010	0.213
2	9.4	0.035	0.122	0.018	0.023	0.068	0.041	0.004	0.009	0.079	0.048
1	5.0	0.007	0.127	0.088	0.121	0.014	0.004	0.032	0.070	0.255	0.027

Table 4.48 Mean, Mean+SD and Max. residual drifts response under GMs scaled at code level considering $I_E=1.5$

Mean, Mean+SD, Max. residual interstorey drifts response of MD-CBF at code level with $I_E=1.5$							
St.	Height (m)	Mean (%h _s)		Mean+SD (%h _s)		Maximum (%h _s)	
		$2t_g$ linear	$8t_g$ elliptical	$2t_g$ linear	$8t_g$ elliptical	$2t_g$ linear	$8t_g$ elliptical
4th	18.2	0.052	0.057	0.092	0.101	0.128	0.140
3rd	13.8	0.102	0.124	0.179	0.213	0.221	0.250
2nd	9.4	0.045	0.044	0.082	0.081	0.124	0.122
GF	5.0	0.075	0.074	0.154	0.153	0.272	0.255

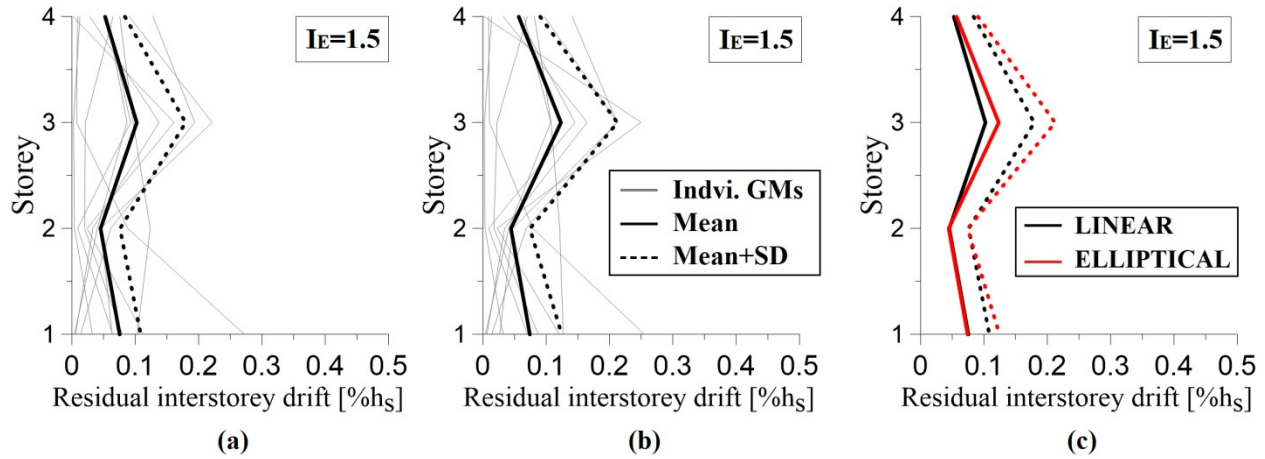


Figure 4.16 Residual drift response: a) MD-CBF with $2t_g$ linear clearance gusset plate model, b) MD-CBF with $8t_g$ elliptical clearance gusset plate model and c) Mean and Mean+SD comparison between the two models

The distribution of floor acceleration along the building height was recorded for each ground motion scaled at their specific scale factor corresponding to $I_E=1.5$ and is given in Tables 4.49 and 4.50 for MD-CBF with $2t_g$ linear and $8t_g$ elliptical clearance models, respectively.

Table 4.49 Distribution of floor acceleration along the MD-CBF building height for the case with $2t_g$ gusset plate model resulted under 10 GMs scaled at code level considering $I_E=1.5$

Distribution of floor acceleration resulted for MD-CBF with $2t_g$ linear clearance gusset plate under GMs scaled at code level considering $I_E=1.5$											
St.	H	GM	GM	GM	GM	GM	GM	GM	GM	GM	GM
	(m)	(g)	(g)	(g)	(g)	(g)	(g)	(g)	(g)	(g)	(g)
4	18.2	1.16	0.93	1.11	1.07	1.02	1.07	1.10	1.04	0.96	1.04
3	13.8	0.81	0.79	1.02	0.84	1.24	0.76	0.89	0.86	0.83	0.89
2	9.4	0.94	0.73	1.27	0.84	1.26	1.06	1.30	0.89	0.97	0.78
1	5.0	0.84	0.68	0.96	0.72	1.04	0.88	0.95	0.80	1.04	0.71

Table 4.50 Distribution of floor acceleration of MD-CBF building height with $8t_g$ gusset plate model resulted under 10 GMs scaled at code level considering $I_E=1.5$

Distribution of floor acceleration resulted for MD-CBF with $8t_g$ elliptical clearance gusset plate under GMs scaled at code level considering $I_E=1.5$											
St.	H	GM	GM	GM	GM	GM	GM	GM	GM	GM	GM
	(m)	(g)	(g)	(g)	(g)	(g)	(g)	(g)	(g)	(g)	(g)
4	18.2	1.17	0.95	1.13	1.08	1.02	1.08	1.12	1.06	0.97	1.03
3	13.8	0.81	0.80	1.05	0.82	1.26	0.77	0.89	0.86	0.83	0.88
2	9.4	0.94	0.72	1.28	0.83	1.27	1.04	1.31	0.88	0.97	0.80
1	5.0	0.86	0.70	0.98	0.73	1.06	0.87	0.94	0.80	1.03	0.72

Although the peak interstorey drift increases on average by 36% from $I_E=1$ to $I_E=1.5$, the peak floor acceleration increased on average by 15%.

Table 4.51 Distribution of Mean, Mean+SD and Max floor acceleration of MD-CBF response when subjected to GMs scaled at code level considering $I_E=1.5$

Mean, Mean+SD and Max. floor acceleration response of MD-CBF at code level considering $I_E=1.5$							
St.	Height (m)	Mean (g)		Mean+SD (g)		Maximum (g)	
		2t linear	8t elliptical	2t linear	8t elliptical	2t linear	8t elliptical
4th	18.2	1.05	1.06	1.11	1.13	1.16	1.17
3rd	13.8	0.89	0.90	0.97	0.98	1.24	1.26
2nd	9.4	1.01	1.01	1.27	1.27	1.30	1.31
GF	5.0	0.86	0.87	1.00	1.01	1.04	1.06

Meanwhile, the Mean and Mean+SD of the floor acceleration envelope resulted from the building response under the 10 scaled ground motions and a comparison between the model with $2t_g$ and $8t_g$ are depicted in Fig. 4.17.

There are little differences in floor accelerations from one clearance model to another. However, it is important to note that, the marginal increase in floor acceleration due to increased seismic demand is smaller than the marginal increase in deformation. It seems that floor accelerations are not as sensitive to earthquake intensity as drifts and residual drifts are. In general, the non-structural components are not damaged when the recorded floors acceleration are less than 1.0g.

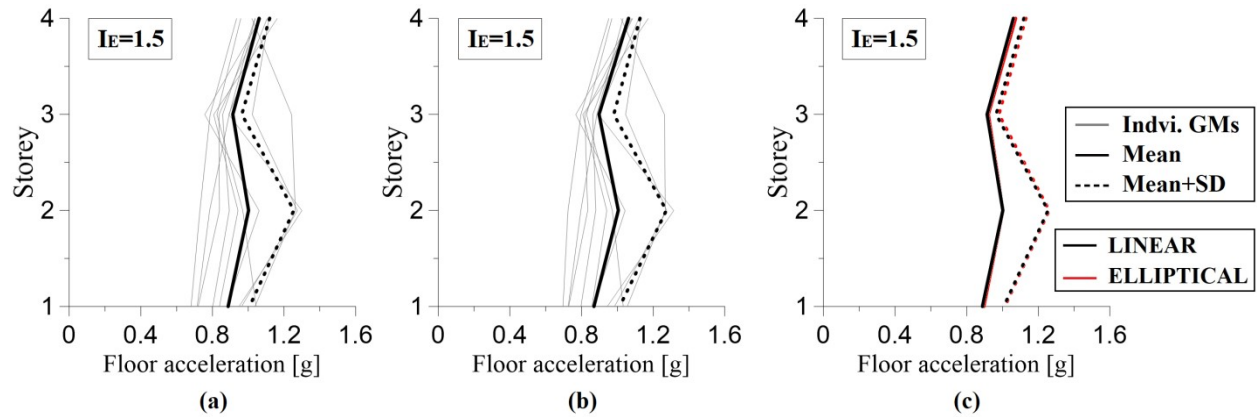


Figure 4.17 Distribution of floor acceleration: a) MD-CBF with $2t_g$ linear clearance gusset plate model b) MD-CBF with $8t_g$ elliptical clearance gusset plate model and c) Mean and Mean+SD comparison between the 2 models

The hysteretic loops of all HSS braces and time-history series of interstorey drift resulted under GM #1006 scaled at code level considering $I_E=1.0$ and $I_E=1.5$ are depicted in Fig. 4.18 and Fig. 4.19, respectively.

The peak interstorey drift occurs at the 3rd floor under GM #1006. By means of hysteresis loop, the behaviour of all HSS braces subjected to ground motion GM #1006 is investigated and plotted in Figure 4.18. At each floor excepting the 4th floor, the left braces were first to reach buckling in compression. At the 3rd floor, the right brace experiences its first buckling at $t=5.14s$, while the left brace experiences its first buckling at $t=7.08s$. As strain is accumulated in the HSS braces, the difference in the hysteretic loop is further pronounced. The right brace undergoes its largest deformation in compression around $t=9.06s$ when the right brace in tension reached its peak elongation value. Finally, at $t=9.42s$, the left brace buckled in compression one last time.

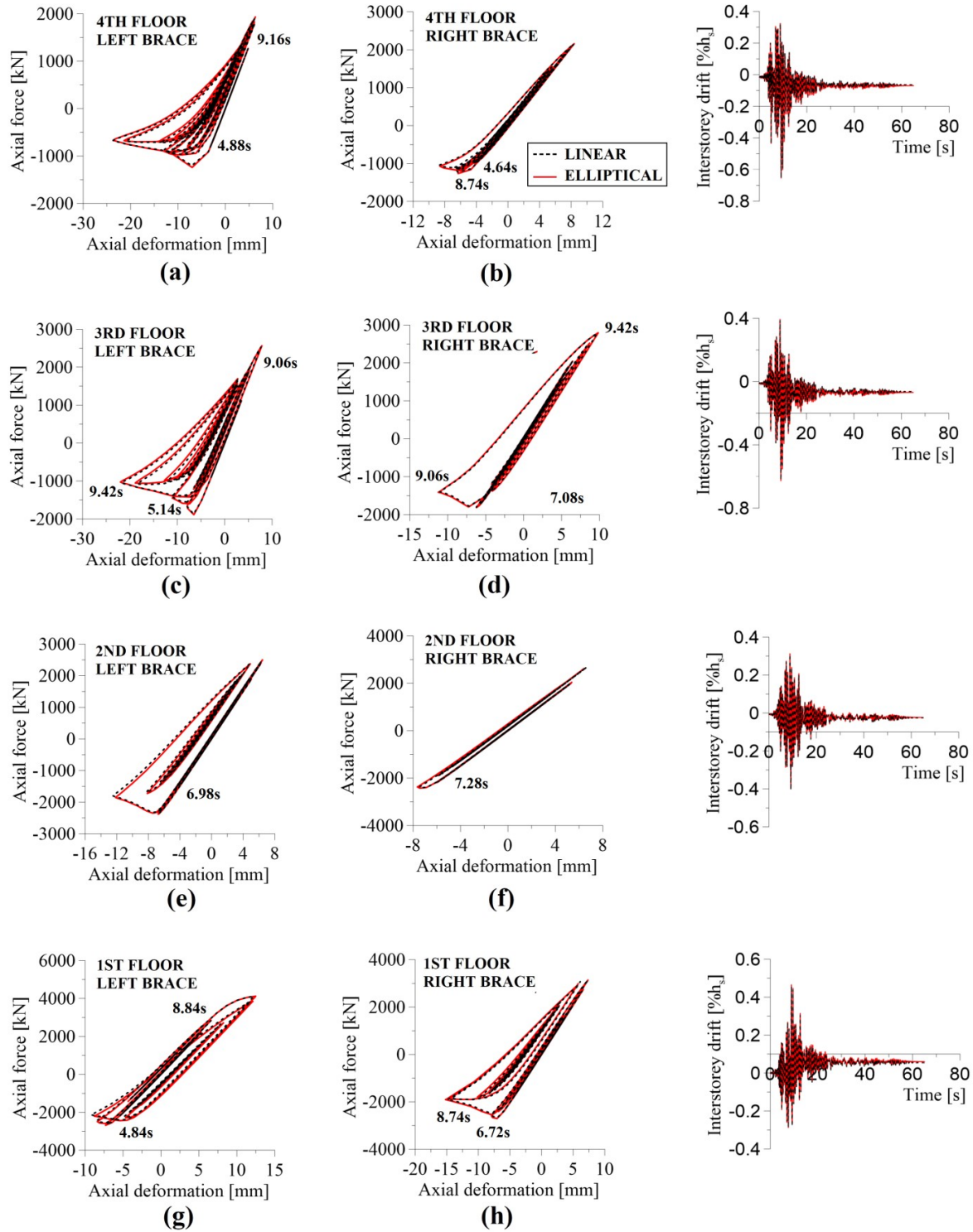


Figure 4.18 Hysteretic loops of HSS braces with $2t_g$ and $8t_g$ gusset plate model and interstorey drift time-history series resulted under GM #1006 scaled at code level considering $I_E=1.0$

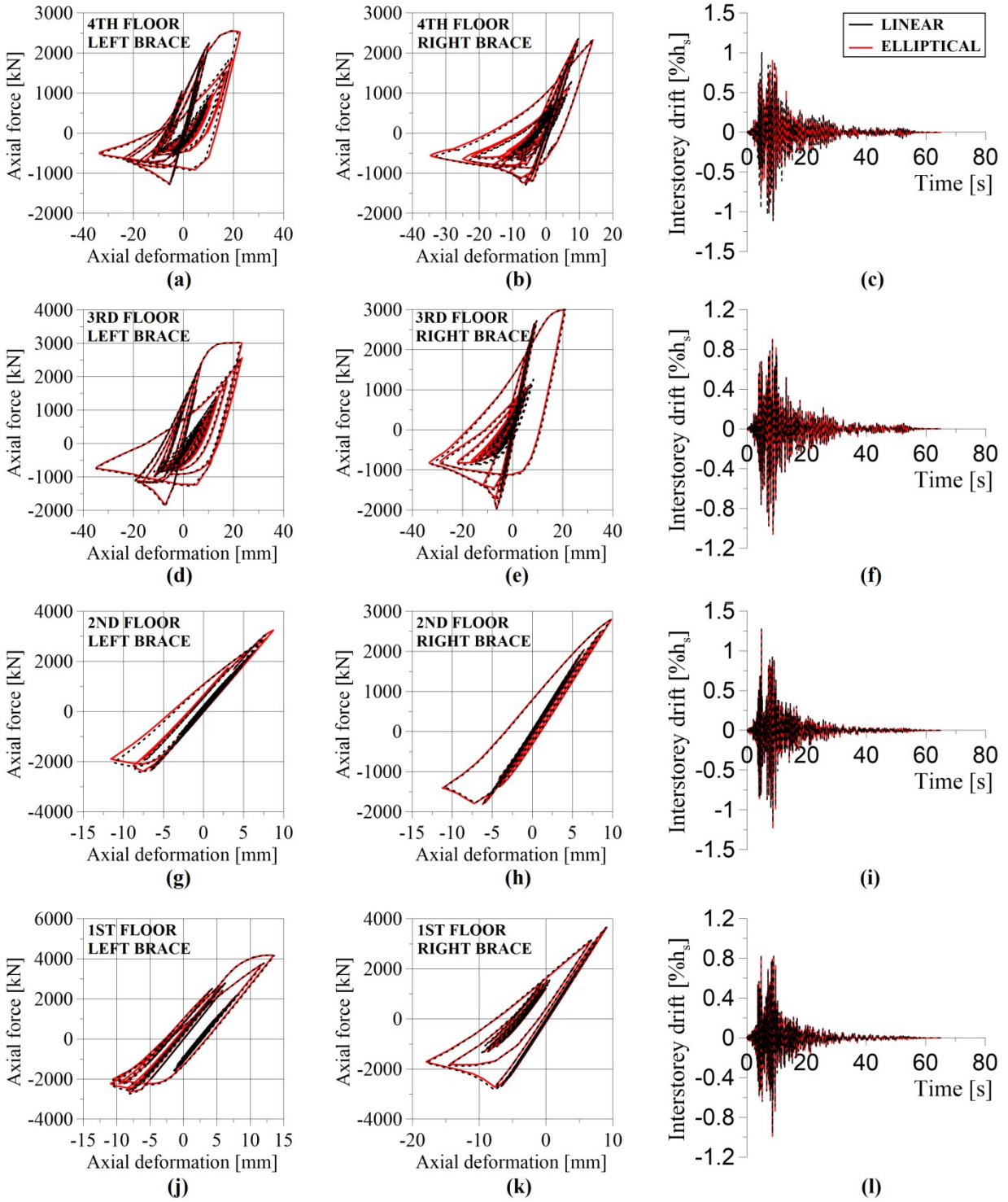


Figure 4.19 Hysteretic loops of HSS braces with $2t_g$ and $8t_g$ gusset plate model and interstorey drift time-history series resulted under GM #1006 scaled at code level considering $I_E=1.5$

When gussets with $8t_g$ elliptical clearance are provided, the rotation capacity increases and larger axial deformation is achieved, as well as larger energy dissipation capacity. Due to the post-disaster building's design that limits the interstorey drift to $1\%h_s$, the potential gain in performance from linear to elliptical clearance gusset plate model is reduced. In other words, by allowing the brace to undergo larger axial deformation, the area under the curve, which represents the dissipated energy becomes larger. In these scenarios, it may have been possible to observe a more favorable building performance when using $8t_g$ elliptical clearance model. Furthermore, the importance factor of 1.5 applied to post-disaster structures increases significantly the forces in members and connections. Hence, thicker gusset plates are required. With thick gusset plates, the benefit of the $8t_g$ elliptical clearance model is further reduced. Furthermore, no significant changes in the floor acceleration were observed. In this light, an alternative system using friction dampers in-line with diagonal braces is investigated in the next chapter to study the overall behaviour of the structure.

Chapter 5

CASE STUDY OF HOSPITAL CBF BUILDING WITH FRICTION SLIDING BRACES

In this chapter, the previous seismic force resisting system of the 4-storey hospital building was redesigned using friction sliding braced frames (FS-BF). Friction dampers can dissipate the earthquake input energy by friction, thereby reducing the earthquake forces that accumulate in adjacent structural members. For this reason, friction dampers are added between the brace end and the brace-to-frame connection to minimize structural damage and the associated cost of repairs. A numerical model of friction dampers behaviour is simulated and calibrated using OpenSees. Then, a full scale model of a hospital building equipped with FS-BFs is subjected to selected ground motions. Hereafter, the previously investigated MD-CBF systems with different gusset plate clearance band of brace-to-frame connections serve as a benchmark to evaluate the seismic behaviour of friction sliding braces. Some guidelines related to seismic design of buildings with friction dampers are presented.

5.1 Design of CBF building with friction sliding braces

To design the FS-BF system, currently, a force-based design method was proposed by Tirca et al. (2018). For comparison purpose, the ductility-related force modification factor R_d and the overstrength-related force modification factor, R_o are considered: $R_o=1.0$ and $R_d=4.0$. In case that the seismic force resisting system has a back-up moment resisting frame system designed to sustain an additional 25% base shear, then $R_o=1.125$ can be used in conjunction with $R_d=5$. However, additional design details are required. It is worth mentioning that the FS-BF system is derived from the MD-CBF with $R_dR_o=3.9$.

As depicted in Fig. 5.1, the HSS brace is connected to a friction damper at one end and to a traditional gusset plate connection at the other end. The FS-BF system behaves as a traditional CBF until the first friction device reaches the slip force, F_{slip} . Employing the force-based design method, to determine the slip force, the equivalent static force procedure is used and the same

lateral force distribution associated with the inverted triangle is applied. Then, the storey shear force is distributed to braces and the factored axial force triggered in braces is the slip force. The associated HSS brace is proportioned to carry $130\% F_{slip}$ in compression and tension. Because the member's buckling strength is lower than its tensile strength, the HSS brace is designed such that: $C_r \geq 130\% F_{slip}$, where C_r is the brace compression resistance. Therefore, friction devices slip before the HSS braces reach buckling. This means that braces behave in the elastic range while friction dampers dissipate energy through friction developed by the relative sliding along the length of a slotted hole. For constructability, the resulted value of slip force is rounded up in multiples of 50 kN and the maximum slip force is recommended to be below 2000 kN for constructability purpose.

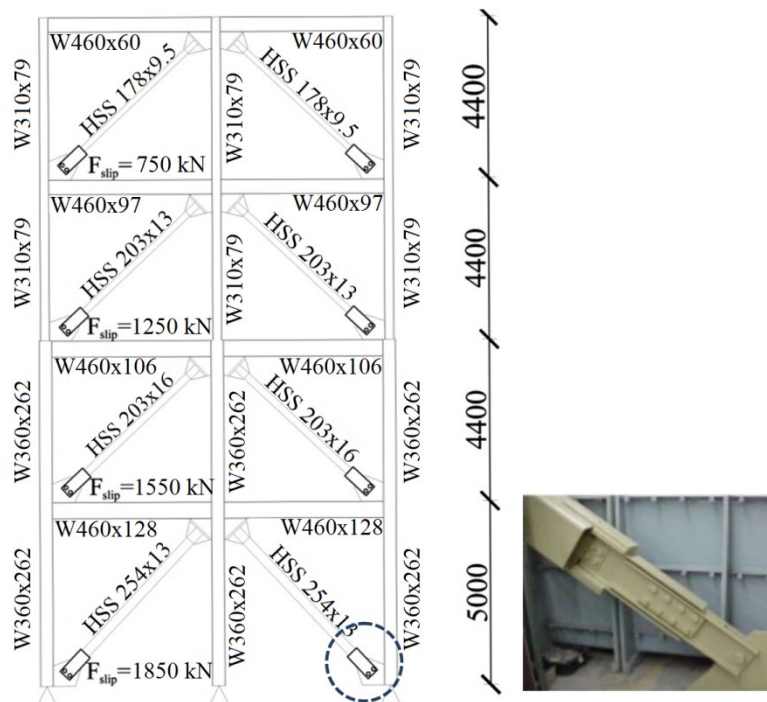


Figure 5.1 Elevation view of FS-BF system (E-W direction): a) elevation, slip force and designed member cross-sections and b) Detail of Pall Friction damper

Meanwhile, it should be check that under the wind load, friction devices do not slip and the system should be proportioned to respond in the elastic range.

As illustrated in Figure 5.1b, the middle plate of friction damper is welded to the slotted HSS brace, while the external channels are bolted to the gusset plate. The friction sliding occurs when

the middle plate slides between the two channels, which are connected with pretension bolts. In order to obtain the required slip length, one must assess the seismic response of the building through nonlinear time-history dynamic analysis under an ensemble of earthquake ground motions that are scaled to match the design spectrum across the periods of interest $0.2T_1-1.5T_1$. This design criterion is discussed later. The cross-sections for the FS-BF system resulted from the equivalent static force procedure are given in Table 5.1. To design beams and columns of the FS-BF system, the capacity design method is applied. Thus, beams are designed to sustain the probable compression strength C_u computed as $1.2C_r(R_y/\phi)$ where $\phi=0.9$ and the probable stress for HSS members is $R_yF_y = 460\text{MPa}$. Herein, the probable tensile strength is limited to the value of probable compression strength. Columns of FS-BF system are designed to carry the loads associated to the load combination $D+0.5L+0.25S+E$ where the earthquake load E is computed as the minimum axial force resulted from the following two cases: a) all braces reached C_u and b) axial factored force associated to $R_dR_\theta = 1.3$. In addition, a bending moment of $0.2M_p$ should be considered. In general, the design of beams and columns follow the procedure provided for CBFs.

Table 5.1 Characteristics of FS-BF system (E-W direction) resulted from the equivalent static force procedure

St.	Slip load, F_{slip} kN	$1.3F_{\text{slip}}$ kN	$C_{r,\text{brace}}$ kN	Brace sections	Beam sections	Column sections
4	750	975	1013	HSS 178X178X9.5	W460x60	W310x79
3	1250	1625	1734	HSS 203X203X13	W460x97	W310x79
2	1550	2015	2053	HSS 203X203X16	W460x106	W360x262
1	1850	2405	2578	HSS 254X254X13	W460x128	W360x262

5.2 Calibration of friction dampers in OpenSees

To perform nonlinear time-history analysis, a model is developed in OpenSees for the friction sliding brace.

5.2.1 Elastic phase and sliding phase calibrations

The OpenSees model for the FS-BF is very similar with the model developed for the traditional CBF system. The difference consists in replacing the traditional gusset plate expected to bend out-of-plane with a friction sliding device. This consists of replacing the rotational spring used to replicate the out-of-plane bending of gusset plate brace connection with a translational spring located in the same *Zero-Length* element in order to simulate the frictional sliding.

Herein, the uniaxial *BoucWen* material was used to simulate the smooth hysteresis behaviour of friction damper replicated by the translational spring displaced in the axial direction in the *Zero-Length* element. The friction damper is activated when the axial force in brace reaches the slip force F_{slip} . The *BoucWen* material is able to simulate the high nonlinear Coulomb friction and has the ability to represent different hysteresis shapes.

The OpenSees model of HSS brace in-line with friction damper device was calibrated against experimental tests conducted on one specimen tested in the Structure lab of Polytechnique University Montreal in 2014. The specimen tested was composed of a short length HSS 203x203x9.5 brace connected to Pall friction damper designed for a slip force of 700kN and the slip length of ± 50 mm. The middle plate of friction damper was welded to a slotted HSS brace. The other end of HSS brace was welded to a thick gusset plate connected to a reaction frame. The other end of full-size friction damper was bolted to a plate attached to the load cell connected to a dynamic actuator. The distance between the end of the HSS brace and the upper channel belonging to friction damper is the damper's stroke or slip length. It is noted that friction devices slip when they are loaded either in tension or in compression. To assure a safety factor, the available slip length or stroke provided by manufacturer is 130% of the design slip length, which is equal to 65 mm in this case. More details regarding the experimental program, loading protocol, and test results on full-scale braces in-line with Pall friction dampers will be presented in a future publication and some info are given in Tirca et al., 2018

The test was conducted under displacement controls. To verify if the friction damper is able to slide across the design slip length of ± 50 mm, a quasi-static cyclic test was applied. The OpenSees model of the test setup is schematically presented in Fig. 5.2. As illustrated, the HSS

brace was divided into four *forceBeamColumn* elements with four integration points per element, while the rigid part of the damper was modelled as a stiff *elasticBeamColumn* element.

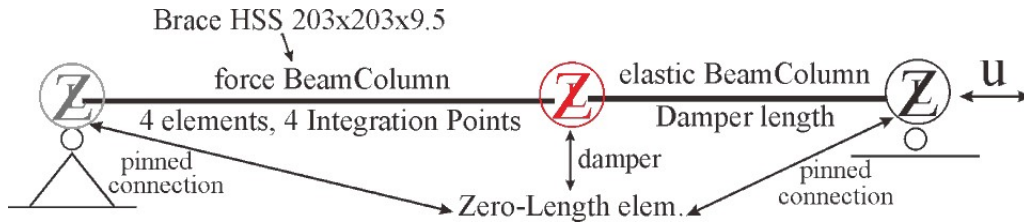


Figure 5.2 OpenSees model of the experimental test

The springs displaced in the *Zero-Length* elements were used to replicate the brace-to-rigid frame connection, the damper-to-actuator connection and to simulate the behaviour of the friction device. In the *BoucWen* material model, the following parameters were given: the ratio of post-yield stiffness to the initial elastic stiffness α , the initial elastic stiffness k_0 , exponent n that influences the sharpness of the model in the transition zones, γ and β parameters controlling the shape of the hysteresis cycle. Other parameters such as A_0 , A , ν and η control the degradation process in stiffness and material, respectively. In this study, the parameters were taken as $A_0 = 1$, $\alpha = A = \nu = \eta = 0$ while γ and β parameters were considered equal and were calculated based on the formula: $\gamma + \beta = 1/(\Delta_y)^n$. In the previous equation, Δ_y represents the yielding displacement of brace member when the damper starts slipping and can be calculated by using the following equation: $\Delta_y = F_{slip}/k_0$, where F_{slip} is the activation slip force and $k_0 = k_{brace} = A_{brace}E/L$. Regarding the sharpness parameter, a value of $n = 10$ was selected for this study, as suggested by Morales (2012). Using this OpenSees model, the replicated hysteresis response against a generic experimental hysteresis loop is shown in Fig. 5.3.

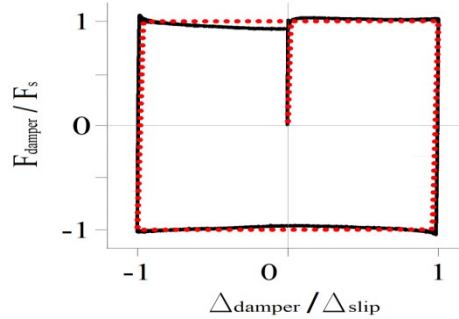


Figure 5.3 Hysteresis response of the OpenSees model versus a generic test response (red is the OpenSees response)

It is noted that an uniaxial *ElasticPerfectlyPlastic* (EPP) material was also used instead of the *BoucWen* material. Although the hysteresis behavior of EPP material does not provide a smooth transition between the elastic phase and sliding phase, it leads to convergence problems when assigned to simulate friction sliding devices of a complex structure model.

5.2.2 Slip-lock phase calibration and failure

In order to investigate the slip-lock phase of friction dampers, the same setup as the previous one was used and the demand exceeded the damper's stroke, which was ± 65 mm (e.g. 50 mm $\times 130\% = 65$ mm). The purpose of investigating the slip-lock response it was to characterize the slip-lock curve. This stage is known as the bearing stage because the end row of pretensioned bolts of friction dampers hit the end of slotted hole and the brace equipped with a friction device behaves as a traditional CBF brace. This may happen when the friction sliding member is loaded either in tension or in compression. During the test, the force was incrementally increased until it reached two times the slip force. Therefore, the friction device was able to sustain two times its design slip force. In terms of deformation, the bearing slope was steeper in compression than that in tension. This is explained that during compression, the available stroke of friction damper u_s is depleted and the outer channels of friction damper may come in contact with the HSS brace end, hence adding more stiffness. The u_s stroke is illustrated in Figure 5.4. During the bearing stage, the holes in the gusset plate used for bolted connections between the two channels and the gusset plate exhibit ovalization type of deformation.

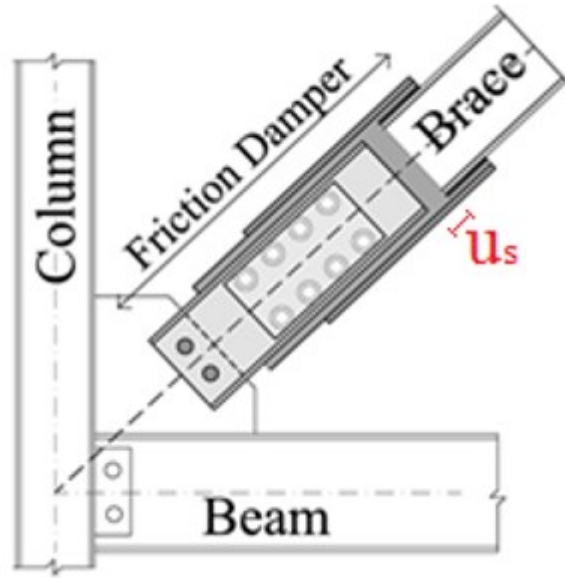


Figure 5.4 Emphasized slip length of friction damper

The stiffness in both compression and tension remained relatively constant. Similar to Morales's proposal (2012), the slip-lock phase was simulated by a series of translational springs made of *ElasticPerfectlyPlastic Gap* material defined in both oscillation directions (tension and compression) and added in parallel to the *BoucWen* material.

A *Hyperbolic Gap* material was also tested and calibrated with the experimental data. After several trials and errors in the input parameters of *Hyperbolic Gap* material, it is possible to better fit the experimental curve in the bearing phase as well as the unloading and reloading stiffness of FDs. However, the hyperbolic gap material can only be implemented as a compression gap material. In this light, the *ElasticPerfectlyPlastic Gap* material is recommended for the slip-lock phase. Using this modeling approach in OpenSees, the model was calibrated against a generic hysteresis loop similar to the experimental tests and is depicted in Fig. 5.5.

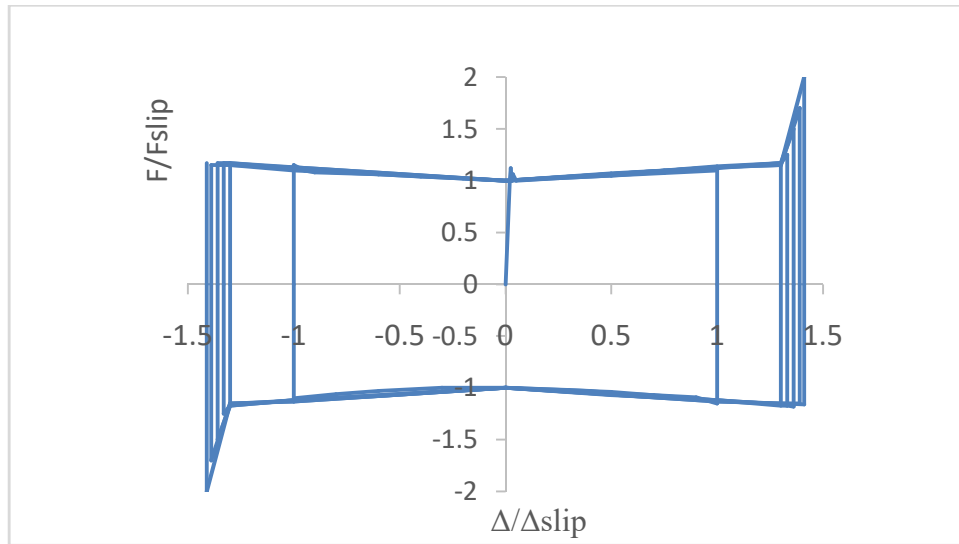


Figure 5.5 Calibration of FD model in OpenSees against a generic hysteresis loop resulted from experimental test

To incorporate the failure of friction damper, a *MinMax* material was assigned to the *ElasticPerfectlyPlastic Gap* material to decouple the device when the force in damper reached two times F_{slip} or bolts fail in shear. Failure of friction damper can be expected when the seismic demand exceeds the available slip length and the pretensioned bolts impact the edge of slotted hole driving the pretensioned bolts to behave in bearing and latter on in shear. Hence, the slip length is an important parameter that is able to control the seismic response of friction damper. On one hand, if the slip length is too small, the energy dissipation capacity of the device is greatly reduced and the slip-lock phase is encountered earlier. On the other hand, if the slip length is too large (e.g. corresponding to $2.5\%h_s$ interstorey drift), important residual deformations are anticipated. It is noted that friction damper devices do not possess self-centering capability.

5.3 Nonlinear response of 4-storey hospital building

Nonlinear dynamic analyses are conducted using OpenSees. Although the brace members were designed to respond in the elastic range, they were simulated by using a force-based nonlinear beam-column elements with distributed plasticity and fiber cross-sections. The *Steel02* material

was assigned to braces, beams and columns. Both beams and columns were simulated using the nonlinear beam-column elements with distributed plasticity similar to the CBF model. It is noted that the brace to frame connection was defined at one brace end as per the CBF model and at the other end as explained above in order to simulate the response of friction damper. The same seismic mass as per the CBF building was considered.

The first-mode period of the 4-storey hospital building resulted from 3-D analysis using ETABS was 0.476s and 0.437s in the E-W and N-S direction, respectively. This value is similar to that resulted from the code equation $0.025h_n$, where $h_n=18.2$ m is the building height. From OpenSees, the first-mode period resulted $T_1= 0.52$ s. Braces of FS-CBF shown in Table 5.1 are slightly stiffer than those of CBF system shown in Table 4.11 and hence the resulted first mode period is slightly shorter.

The hospital building model was subjected to 10 crustal ground motions typical for the Pacific coast of North America. The selected engineering demand parameters are: i) the interstorey drift, ii) the residual interstorey drift iii) floor acceleration and iv) the energy dissipated by friction sliding braces illustrated by means of hysteresis loops.

Table 5.2 First mode period of studied structural systems

Software model	MD-CBF	FS-CBF
	$T_{1,E-W}$ (s)	$T_{1,E-W}$ (s)
ETABS	0.483	0.476
OpenSees	0.516	0.520

5.3.1 Ground motion scaling

The FS-BF hospital building was subjected to the same 10 ground motions as the CBF building. However, due to the slight difference in dynamic period, ground motions were slightly rescaled over the interval $[0.2T_1 - 1.5T_1]$ as shown in Figure 5.6. The scale factor for each ground motion is given in Table 5.3.

Table 5.3 Selected crustal ground motions and scaling factor

GM	Event	M_w	Station	S. F. ($I_E=1$)	S. F. ($I_E=1.5$)
57	Feb. 9, 1971 San Fernando	6.6	Castaic, Old Ridge Route	1.85	2.78
767	Oct. 18, 1989 Loma Prieta	6.9	Gilroy Array #3	1.68	2.52
787	Oct. 18, 1989 Loma Prieta	6.9	Palo Alto - SLAC Lab	0.98	1.47
796	Oct. 18, 1989 Loma Prieta	6.9	SF - Presidio	1.91	2.87
739	Oct. 18, 1989 Loma Prieta	6.9	Anderson Dam (Downstream)	1.95	2.93
963	Jan. 17, 1994 Northridge	6.7	Castaic, Old Ridge Route	0.85	1.28
986	Jan. 17, 1994 Northridge	6.7	LA - Brentwood VA Hospital	1.98	2.97
1006	Jan. 17, 1994 Northridge	6.7	LA - UCLA Grounds	1.94	2.91
1039	Jan. 17, 1994 Northridge	6.7	Moorpark - Fire Station	1.84	2.76
1077	Jan. 17, 1994 Northridge	6.7	St Monica	1.68	2.52

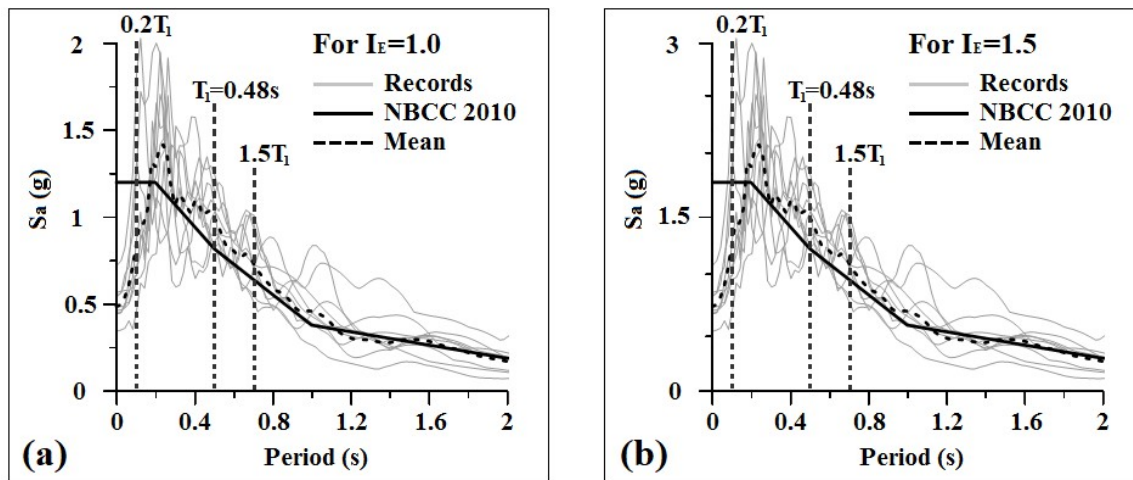


Figure 5.6 Design spectrum and 5% damped absolute acceleration spectra of the scaled ground motions for: a) $I_E = 1.0$ and b), $I_E = 1.5$

5.3.2 Nonlinear response

At first, the friction damper model does not include the simulation of the stick-lock phase (SL) in order to determine the required slip length. The friction damper was simulated by using the *BoucWen* model and the maximum interstorey drifts resulted under each scaled ground motion were recorded and are provided in Table 5.4. To ensure that the parameters used are appropriate,

the *BoucWen* material assigned to simulate the response of friction dampers was replaced by an *ElasticPerfectlyPlastic* (EPP) material for comparison purpose.

Table 5.4 Distribution of interstorey drifts of FS-BF using *BoucWen* material for FDs under scaled ground motions

Distribution of interstorey drift at code level with $I_E=1$ for <i>BoucWen</i> model without SL simulation											
ST	H	GM	GM	GM	GM	GM	GM	GM	GM	GM	GM
	(m)	(% h_s)	(% h_s)	(% h_s)	(% h_s)	(% h_s)	(% h_s)	(% h_s)	(% h_s)	(% h_s)	(% h_s)
		739	986	1006	57	1077	1039	767	963	796	787
4	18.2	0.658	0.810	0.990	0.510	0.926	0.568	0.621	0.959	0.554	0.941
3	13.8	0.671	0.892	0.979	0.517	0.871	0.466	0.515	0.915	0.574	0.970
2	9.4	0.496	0.523	0.520	0.560	0.466	0.441	0.397	0.634	0.737	0.865
1	5.0	0.522	0.553	0.789	0.588	0.594	0.649	0.367	0.719	0.970	0.978

Table 5.5 Distribution of interstorey drifts of FS-BF using EPP model for FDs under scaled ground motions

Distribution of interstorey drift at code level with $I_E=1$ for <i>ElasticPerfectlyPlastic</i> model without SL simulation											
ST	H	GM	GM	GM	GM	GM	GM	GM	GM	GM	GM
	(m)	(% h_s)	(% h_s)	(% h_s)	(% h_s)	(% h_s)	(% h_s)	(% h_s)	(% h_s)	(% h_s)	(% h_s)
		739	986	1006	57	1077	1039	767	963	796	787
4	18.2	0.656	0.812	0.991	0.509	0.926	0.567	0.621	0.957	0.556	0.941
3	13.8	0.670	0.894	0.980	0.517	0.872	0.465	0.515	0.914	0.574	0.970
2	9.4	0.498	0.523	0.521	0.560	0.467	0.441	0.396	0.633	0.737	0.863
1	5.0	0.521	0.553	0.790	0.588	0.595	0.648	0.368	0.719	0.970	0.959

It is concluded that both *BoucWen* and *EPP* models yield similar outputs in terms of interstorey drifts for all ground motions. Hence, both material models could be interchangeably used to mimic the behaviour of friction dampers. In this study, the *BoucWen* model is kept onwards. Under all ground motions, the peak interstorey drift was below the allowable maximum interstorey drift of 1% h_s for post-disaster buildings. FS-BF should be designed not to experience the bearing stage under code level seismic events. The slip length must be increased until this requirement is met for all scaled ground motions. During the slip phase, the period of the building increases due to the decrease in the overall stiffness of the SFRS. In Figure 5.6, the

scaled acceleration response spectrum of ground motion #787 is well above the code design spectrum at T_1 and increases abruptly after that, while other records tend to decrease as the period elongates. This may have contributed to the increase in drift demand. The response under GM #796 is further investigated in a later section.

The distribution of interstorey drift among floors is illustrated in Fig. 5.7. As aforementioned, both models were considered to simulate friction dampers without the consideration of slip-lock phase. As resulted, the average of interstorey drifts under the 10 ground motions is lower than $1.0\%h_s$, which is the code limit for post-disaster buildings and is represented by solid black line.

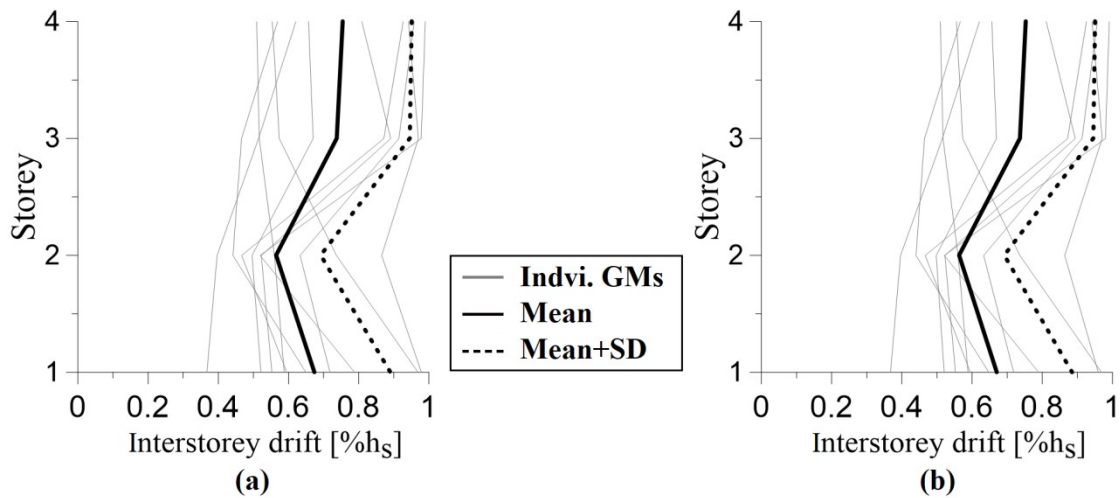


Figure 5.7 Distribution of interstorey drift over building height for FS-BF (E-W direction): a) BW model b) EPP model

By establishing the maximum interstorey drift from nonlinear dynamic analyses without considering the slip-lock phase, the required damper's stroke is obtained for each ground motion and is shown in Table 5.6.

Table 5.6 Damper displacement demand simulated with *BoucWen* material under GMs

Damper displacement demand at code level with $I_E=1$ for BoucWen model without SL simulation										
St.	GM	GM	GM	GM	GM	GM	GM	GM	GM	GM
	739	986	1006	57	1077	1039	767	963	796	787
	(mm)	(mm)	(mm)	(mm)	(mm)	(mm)	(mm)	(mm)	(mm)	(mm)
4	17	21	28	12	25	14	15	26	13	25
3	15	22	26	10	22	9	10	23	12	25
2	10	10	10	12	9	8	6	14	17	22
1	10	13	20	13	14	16	5	17	26	27

There are no strict guidelines for sizing the design slip length, u_{slip} , of friction damper devices. One can consider the average of all ground motion as well as the 84% percentile or the maximum demand. As depicted in Table 5.6, at the top floor, the maximum demand is 28 mm and $130\% \times 28\text{mm} = 36$ mm. At the bottom floor, the maximum demand is 27 mm and $130\% \times 27\text{mm} = 35$ mm. In Table 5.7, the average slip lengths resulted from Table 5.6, as well as the Mean+SD and the Max. Values, are provided. Although, the current code requires using the mean to evaluate the seismic response of a building that is subjected to at least 7 ground motions (AISC), in this case study, it is recommended to use the Max. value to establish the damper's stroke. As depicted in Table 5.7, the maximum demanded slip length at each floor is lower than the associated elongation corresponding to $1\%h_s$. Herein, the axial elongation of brace associated to $1\%h_s$ is computed as: $1\%h_s \times \cos(\alpha)$, where α is the angle between the brace and the horizontal line (e.g. $\alpha = 46.88^\circ$ at typical floor and $\alpha = 46.77^\circ$ at ground floor). The stroke is computed as $1.3u_{slip} + d_{bolt}$, where d_{bolt} is the diameter of pretensioned bolts of friction damper.

Table 5.7 Possible slip length resulted underground motions scaled to comply with $I_E=1$

Slip length (SL) resulted under ground motions scaled to comply with $I_E=1$							
St.	Mean	Mean+SD	Max.	Selected slip length (u_{slip})	1.3 u_{slip}	$1\%h_s$	Axial elongation of sliding brace ($1\%h_s \times \cos(\alpha)$)
	(mm)	(mm)	(mm)	(mm)	(mm)	(mm)	(mm)
4	20	26	28	28	36	44	31
3	17	24	26	26	34	44	31
2	12	17	22	22	29	44	31
1	16	23	27	27	35	50	34

In this study, it is proposed to select the design slip length, u_{slip} , based on the maximum value between the Max. slip length and the slip length associated with interstorey drift of $1\%h_s$ for post-disaster buildings. This will ensure that the FD-BF does not go in the slip-lock phase under severe earthquakes scaled to the code level. Local damages are mitigated by avoiding the pre-tensioned bolts to come in contact with the edge of the slotted hole. The selected slip length, u_{slip} , is then increased by 130% to obtain the damper's stroke. For constructability, the peak among floors was selected and is shown in Table 5.8.

Table 5.8 Proposed slip length for friction dampers associated with $I_E=1$

St.	Max. slip length (mm)	Axial elongation of sliding brace associated with $(1\%h_s) \times \cos(\alpha)$ (mm)	1.3 x Max of Max slip & axial elong. of sliding brace (mm)	Proposed slip length ($1.3u_{slip}$) (mm)
4	28	31	41	45
3	26	31	41	45
2	22	31	41	45
1	27	34	45	45

To analyse the time-history series of interstorey drift obtained at all floors, the responses to GM #1006, GM #739 and GM #796 were selected for investigations. In Fig. 5.8 is depicted the scaled ground motion #1006, which has a duration of 60s. Ten seconds were added with zero displacement to observe the response to free vibrations. As depicted, during the first 10 seconds, the building deflects in the first mode shape. After that, the structure oscillates on one side, while the upper two floors are exposed to higher residual interstorey drift than the bottom two floors. This behaviour may be explained by the fact that columns are continuous over two storeys. The column tier of the upper two floors is pin-connect to the bottom column tier. This behaviour is observed in most situations. For example, in Figs. 5.9 and 5.10 are depicted the time-history series of interstorey drifts of all floors when the FS-BF is subjected to GM #739 and GM #796, respectively. Their behaviour is very similar. Thus, to reduce the residual interstorey drift, one solution could be to maintain columns continuous over the structure height.

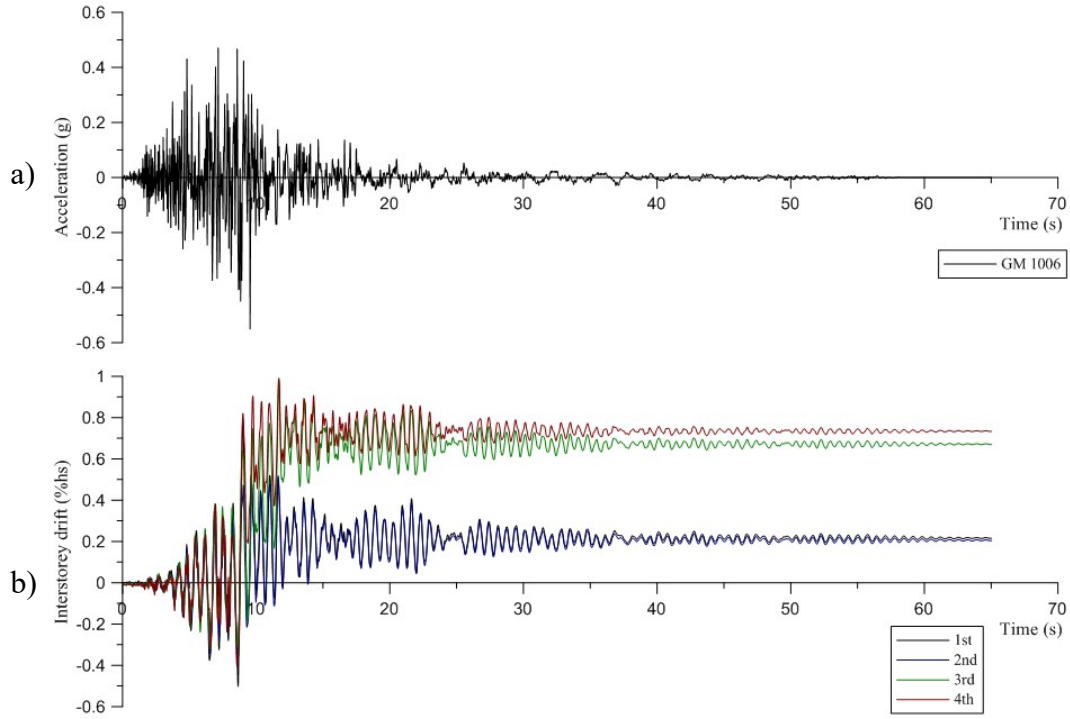


Figure 5.8 Time history response of FD-BF: a) scaled accelerogram of GM # 1006 and b) interstorey drift at each floor of hospital building

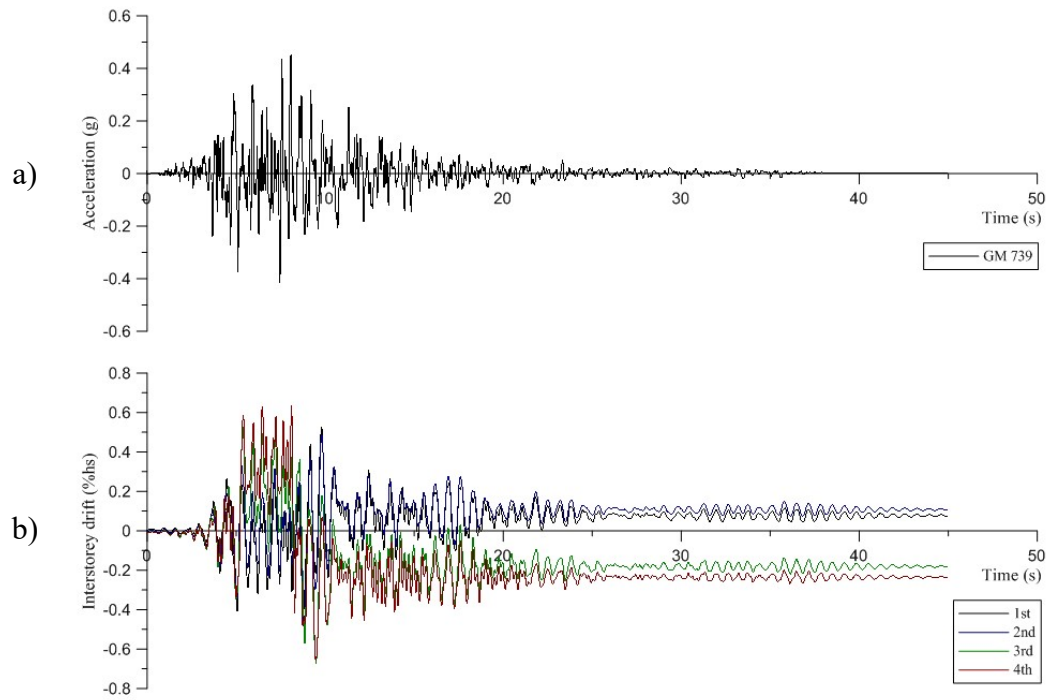


Figure 5.9 Time history response of FD-BF: a) scaled accelerogram of GM #739 and b) interstorey drift at each floor of hospital building

Under low frequency ground motions such as GM #739, dampers of all floors tend to activate at similar time and practically at the beginning of the record. It is apparent that the ground motion's characteristic such as frequency play an important role in FD-BF behavior. The amount of load reversal is smaller during these seismic events, hence reducing the slip-stick behavior seen in FD when the friction coefficient varies from static to dynamic and vice-versa. This, in turn, reduces the vibrations within the system that may lead to premature failure due to excessive wear and tear. The interstorey drifts under GM # 796 are then investigated due to the excessive displacements seen in Table 5.4.

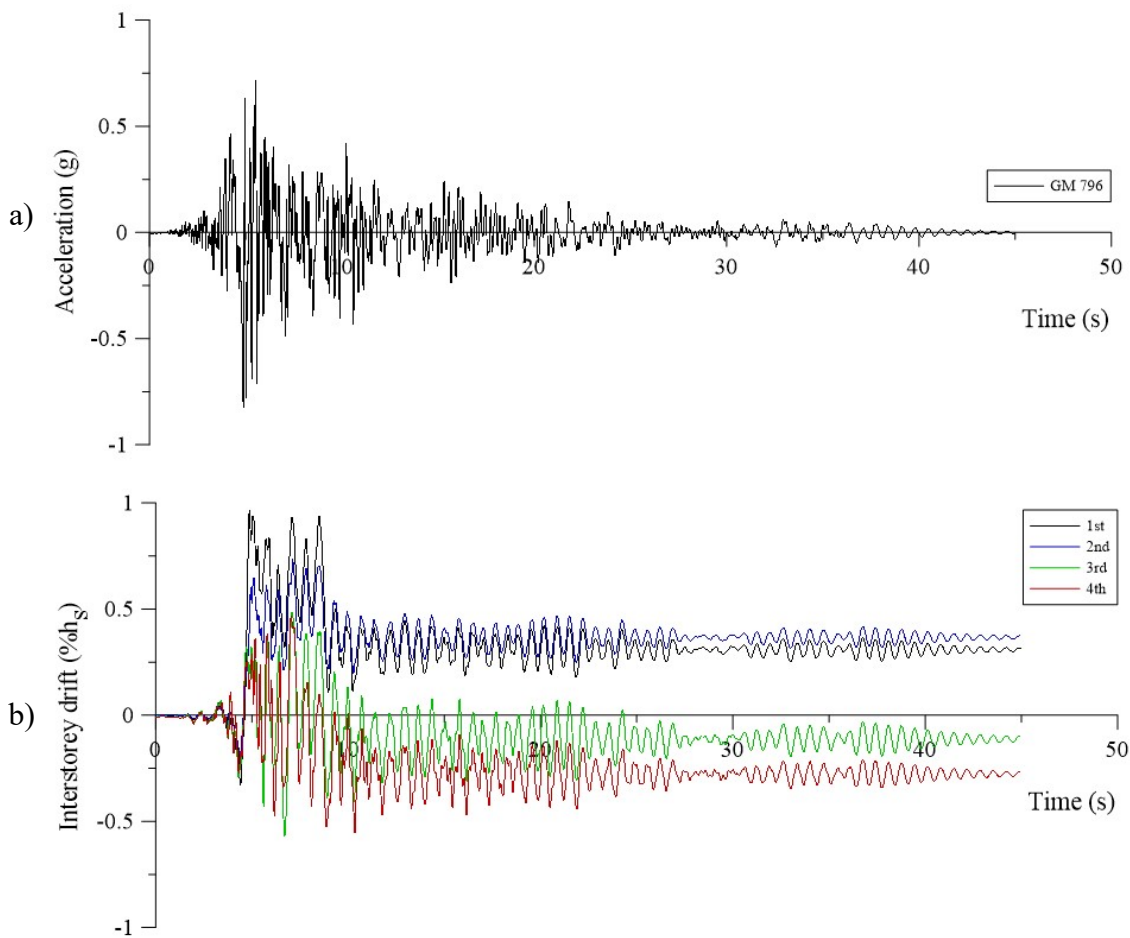


Figure 5.10 Time history response of FD-BF: a) scaled accelerogram of GM #796 and b) interstorey drift at each floor of hospital building

According to Table 5.4, the maximum peak interstorey drift occurred at 1st floor under ground motion #796. As shown in Figure 5.11, the peak drifts and the maximum ground motion accelerations do not occur at the same time. FS-BFs without self-centering systems, such as moment-resisting frames, have no means to realign itself to its initial position. Due to this characteristic, the drifts are cumulated when the ground motion acts in a predominant direction. When GM #796 reached the time step corresponding to T_p (main period of accelerogram), all friction devices yield to their available slip length. After $t = 6.82s$, the ground floor and second floor oscillate on one side with large residual interstorey drift while the upper floors oscillate on the other side but exhibit lower residual interstorey drift of about $0.25\%h_s$. Herein, the simulation of friction dampers with *ElasticPerfectlyPlastic* material is disregarded as it yields the same results as that using the *BoucWen* material for friction damper simulation.

The residual drifts associated with $I_E=1$ are plotted in Table 5.9.

Table 5.9 Residual interstorey drift of FS-BF with FDs simulated with *BoucWen* material at $I_E=1$

Distribution of residual interstorey drift at code level with $I_E=1$ for FDs with BoucWen material											
St.	H	GM	GM	GM	GM	GM	GM	GM	GM	GM	GM
	(m)	(% h_s)	(% h_s)	(% h_s)	(% h_s)	(% h_s)	(% h_s)	(% h_s)	(% h_s)	(% h_s)	(% h_s)
4	18.2	0.240	0.502	0.733	0.051	0.561	0.007	0.104	0.545	0.278	0.634
3	13.8	0.184	0.536	0.669	0.008	0.517	0.127	0.127	0.548	0.188	0.622
2	9.4	0.102	0.170	0.206	0.088	0.023	0.052	0.000	0.308	0.452	0.491
1	5.0	0.069	0.171	0.215	0.057	0.129	0.082	0.021	0.361	0.403	0.587

When the demand in damper displacement is lower than the available slip length of friction dampers, the residual interstorey drifts resulted when the bearing phase is simulated by means of a series of translational springs made of *EPP Gap* material, which is added in parallel to the *BoucWen* material, is the same as that without the addition of *EPP Gap* material. The distribution of residual interstorey drift across the building height is illustrated in Fig. 5.12. As depicted, the peak of Mean residual drift is below $0.5\%h_s$, which means that the building is repairable after an earthquake event of an intensity that meets the code demand. In the case of FS-BF, the Mean+SD residual interstorey drift is about $0.5\%h_s$ underscaled ground motions complying with $I_E=1.0$. This suggests that a back-up system with some self-centering features is

definitely required to decrease the residual drifts below $0.5\%h_s$ and to avoid the case when the building cannot be retrofitted after a severe earthquake event.

The maximum floor acceleration resulted for the FS-BF, equipped with friction dampers simulated with *BoucWen* material, were also recorded for each ground motion scaled at code level ($I_E=1$). The values of floor acceleration demand resulted under each scaled GM are provided in Table 5.10 and the distribution of floor acceleration among floors is depicted in Fig. 5.13. As resulted, the floor acceleration across the building height shows uniform distribution at expected earthquake levels ($I_E=1.0$).

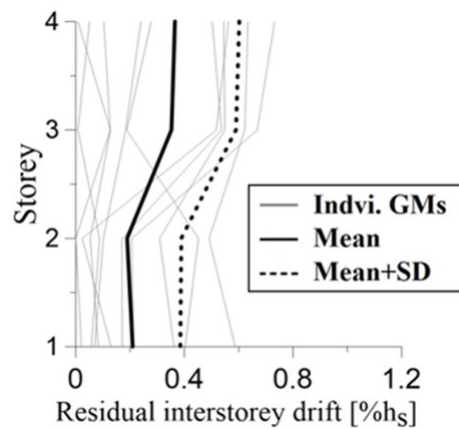


Figure 5.11 Distribution of residual interstorey drift along the height of FS-BF building (E-W)

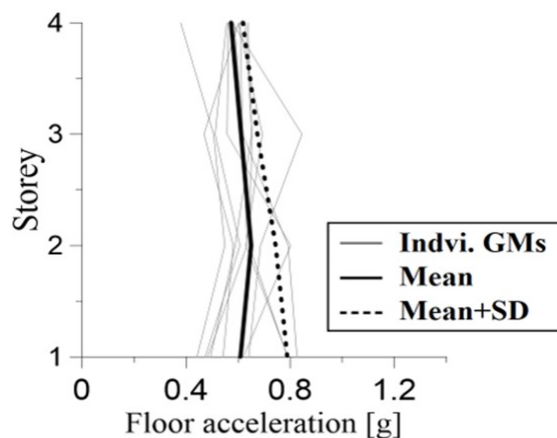


Figure 5.12 Distribution of floor acceleration along the height of FS-BF building (E-W)

Table 5.10 Distribution of floor acceleration of FS-BF equipped with friction dampers simulated with *BoucWen* material at $I_E=1$ (E-W direction).

Distribution of floor acceleration of FS-BF under GMs scaled at code level with $I_E=1$											
St.	H	GM	GM	GM	GM	GM	GM	GM	GM	GM	GM
	(m)	(g)	(g)	(g)	(g)	(g)	(g)	(g)	(g)	(g)	(g)
4	18.2	0.608	0.602	0.585	0.554	0.600	0.628	0.577	0.562	0.380	0.637
3	13.8	0.617	0.469	0.620	0.510	0.692	0.653	0.844	0.557	0.506	0.651
2	9.4	0.792	0.581	0.634	0.605	0.629	0.643	0.685	0.801	0.549	0.588
1	5.0	0.826	0.542	0.483	0.472	0.790	0.789	0.640	0.620	0.442	0.493

The hysteresis response of the left and right damper per floor and the associated interstorey drift resulted under the scaled GM #1006 to match the design spectrum associated to $I_E = 1.0$ is depicted in Figure 5.14. The peak interstorey drift occurred at the 4th floor. At each floor, excepting the 4th, the left and right dampers slide simultaneously. At 4th floor, the left damper slides first at the time step equal to 6s, while the right damper starts sliding at 6.36s.

Furthermore, due to the additional safety measures required for post-disaster buildings, the effects of $I_E=1.5$ amplified forces are examined. As aforementioned, the dynamic analysis procedures are given in NBCC 2010. According to Sentence 4.1.8.12(7), the design elastic base shear V_{ed} , which does not take into account either the inelastic response or the importance of the structure must be divided by the product $R_d R_o$ and multiplied by the importance factor I_E to obtain the design base shear, V_d . In this manner, the post-disaster buildings are deemed to be able to withstand the amplified force related to an importance factor, $I_E=1.5$. In addition, according to Sentence 4.1.8.12(10), the resulted elastic interstorey drifts need to be multiplied by the product $R_d R_o / I_E$ to obtain realistic values of anticipated deflections and drifts. In other words, this clause allows the designer to evaluate the deformations and drifts of a structure at expected code level earthquakes and not at the amplified seismic records associated to $I_E = 1.5$.

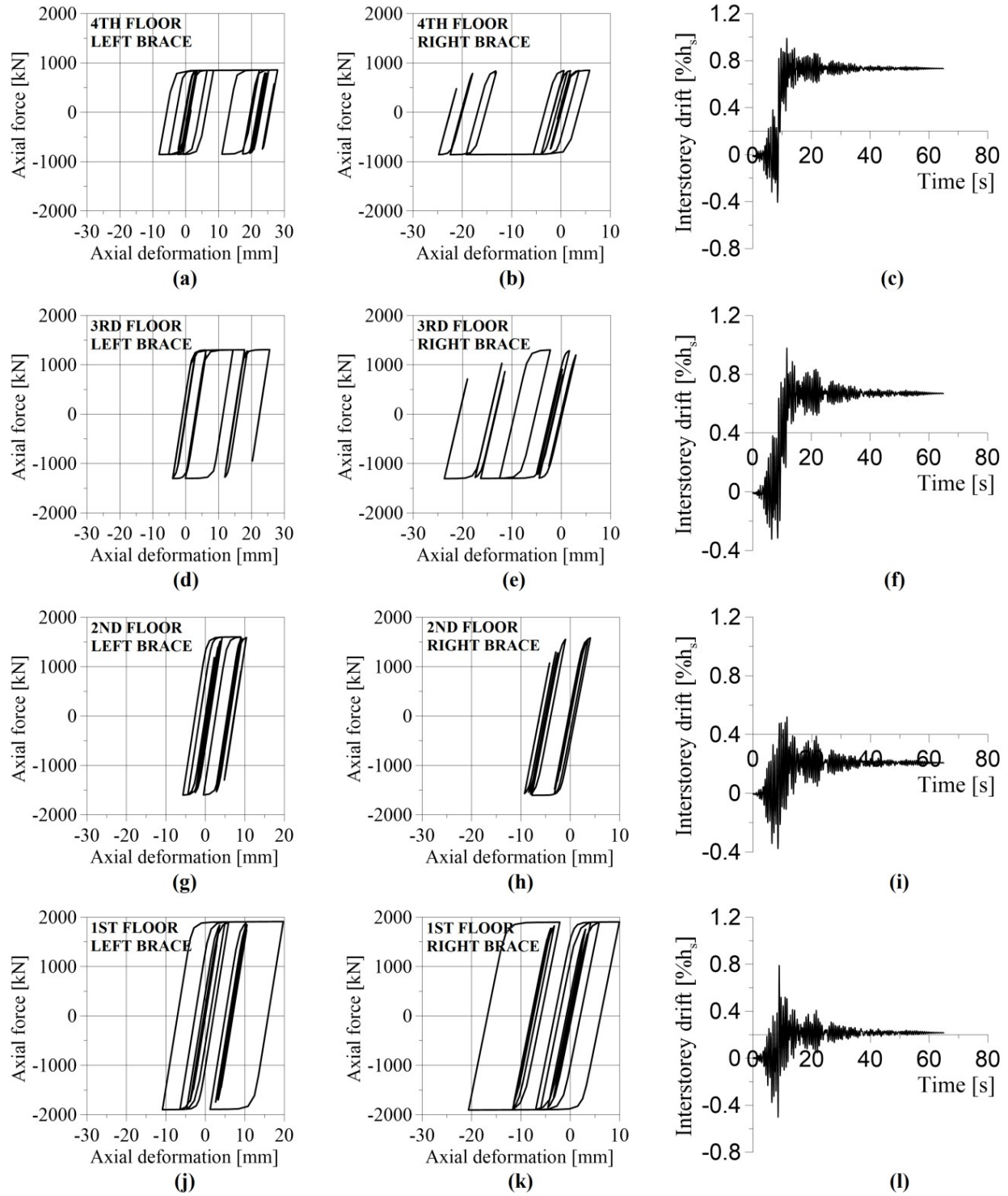


Figure 5.13 Hysteretic loops of friction damper and interstorey drift time-history series resulted under GM #1006 scaled at code level considering $I_E=1.0$

In order to assess the strength resistance of a post-disaster building, the ground motion accelerograms were rescaled to include the effect of I_E , as shown in Table 5.3. In this light, similar to the dynamic analysis procedure described in NBCC 2010, the building is checked against higher scale factors applied to ground motions that are associated with code level earthquake events amplified by $I_E=1.5$. In this light, the distribution of interstorey drifts along the building height obtained under the code level with $I_E=1.5$ is recorded for a model without slip-lock conditions and is shown in Table 5.11. In Table 5.12 it is shown the Mean, Mean+SD and Max. values of interstorey drifts provided in Table 5.11 and the associated damper displacement is shown in Table 5.13.

Table 5.11 Distribution of interstorey drift at code level with $I_E=1.5$ when braces are simulated using *BoucWen* material without Slip Lock simulation

Distribution of interstorey drift at code level with $I_E=1.5$ for <i>BoucWen</i> model without Slip Lock (SL)											
St.	H	GM	GM	GM	GM	GM	GM	GM	GM	GM	GM
	(m)	(%h _s)	(%h _s)	(%h _s)	(%h _s)	(%h _s)	(%h _s)	(%h _s)	(%h _s)	(%h _s)	(%h _s)
4	18.2	1.039	0.860	1.659	0.962	1.022	1.031	0.924	1.669	0.828	1.453
3	13.8	1.284	0.926	1.652	1.273	0.808	0.685	0.716	1.515	0.886	1.558
2	9.4	0.659	1.029	0.706	1.043	1.226	0.577	0.428	0.848	0.966	1.003
1	5.0	0.854	1.307	0.901	1.426	1.437	0.893	0.471	1.264	1.377	1.359

Table 5.12 Distribution of Mean, Mean+SD and Max. interstorey drift response at code level considering $I_E=1.5$

Mean, Mean+SD and Max. interstorey drifts comparison at code level with $I_E=1.5$				
St.	H	Mean	Mean+SD	Maximum
	(m)	(%h _s)	(%h _s)	(%h _s)
4	18.2	1.15	1.45	1.67
3	13.8	1.13	1.48	1.65
2	9.4	0.85	1.09	1.23
1	5.0	1.13	1.44	1.44

As resulted from Table 5.12, the Mean is 15% larger than the code limit of 1.0%h_s. The slip length demand recorded in each damper under each ground motion is shown in Table 5.13 and the Mean, Mean+SD, and the Max. value of slip length are provided in Table 5.14.

Table 5.13 Distribution of damper slip length demand at code level with $I_E=1.5$ for FDs simulated with *BoucWen* material without SL simulation

Damper slip length demand at code level with $I_E=1.5$ for <i>BoucWen</i> model without SL simulation										
S T	GM	GM	GM	GM	GM	GM	GM	GM	GM	GM
	(mm)	(mm)	(mm)	(mm)	(mm)	(mm)	(mm)	(mm)	(mm)	(mm)
4	28	23	47	27	28	29	28	46	19	41
3	34	23	44	34	20	16	19	41	19	42
2	15	26	16	27	32	12	9	21	21	26
1	23	38	24	41	41	24	9	35	33	40

Table 5.14 Proposed slip length for friction dampers associated with $I_E=1.5$

Slip length (SL) to be considered with $I_E=1.5$							
St.	Mean	Mean+SD	Max.	Selected slip length (u_{slip})	$1.3x u_{slip}$	Axial elongation of sliding brace ($1\%h_s$) x $\cos(\alpha)$	Axial elongation of sliding brace ($2\%h_s$) x $\cos(\alpha)$
	(mm)	(mm)	(mm)	(mm)	(mm)	(mm)	(mm)
4	32	41	47	47	61	31	62
3	29	40	44	44	57	31	62
2	21	28	32	32	42	31	62
1	31	41	41	41	53	34	68

Although the Mean interstorey drift is slightly above $1\%h_s$, which may be deemed acceptable, it is recommended to select the slip length demand based on the maximum demand multiplied by 130%. As is shown in Table 5.14, it is recommended to round up the peak of $1.3u_{slip}$ to nearest 5 mm, which leads to 65 mm for the damper's stroke demand, which is approximately associated to $2\%h_s$ interstorey drift.

Once the available slip length is established, the slip-lock phase can be added to the friction damper model. As mentioned in Section 5.2.1, the bearing phase is simulated with a series of translational springs made an *ElasticPerfectlyPlastic* gap material, which is placed in parallel with the *BoucWen* material in the *Zero-Length* element. Due to the lack of experimental data on the bearing phase of FD devices, the tangent stiffness obtained from the aforementioned test is used as a constant in this model for all dampers. The new model is then re-subjected to the same 10 scaled ground motions and the distribution of interstorey drift among floors and the demand

of dampers slip length associated with $I_E = 1.5$ is plotted in Figure 5.14. In addition, the distribution of residual interstorey drift and floor acceleration is depicted in Figures 5.15 and 5.16, respectively. The residual interstorey drift obtained under each scaled ground motions is provided in Table 5.15 and the recorded floor acceleration values are given in Table 5.16.

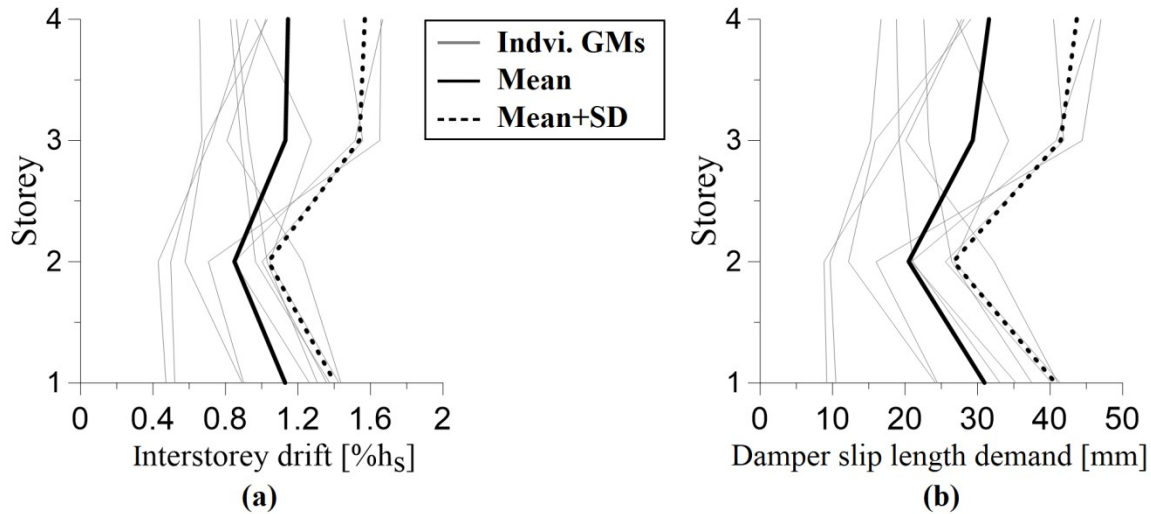


Figure 5.14 Distribution of interstorey drift and damper's slip length demand across the building height under GMs scaled to comply with $I_E=1.5$

Table 5.15 Distribution of residual interstorey drift of FS-BF with FDs simulated with *BoucWen* material resulted under GMs scaled to comply with $I_E=1.5$

Distribution of residual drift at code level with $I_E=1.5$ for BoucWen model											
St.	H	GM	GM	GM	GM	GM	GM	GM	GM	GM	GM
	(m)	(%h _s)	(%h _s)	(%h _s)	(%h _s)	(%h _s)	(%h _s)	(%h _s)	(%h _s)	(%h _s)	(%h _s)
4	18.2	0.529	0.469	1.115	0.686	0.053	0.128	0.123	0.410	0.309	1.027
3	13.8	0.500	0.584	1.099	0.803	0.036	0.124	0.137	0.391	0.456	1.043
2	9.4	0.117	0.635	0.328	0.566	0.037	0.032	0.033	0.505	0.280	0.136
1	5.0	0.217	0.533	0.286	0.679	0.052	0.021	0.089	0.541	0.379	0.207

The residual drifts of FS-BF are much larger than those recorded for the MD-CBF models. The comparison between the 2 systems, MD-CBF and FS-CBF, is discussed in the next section.

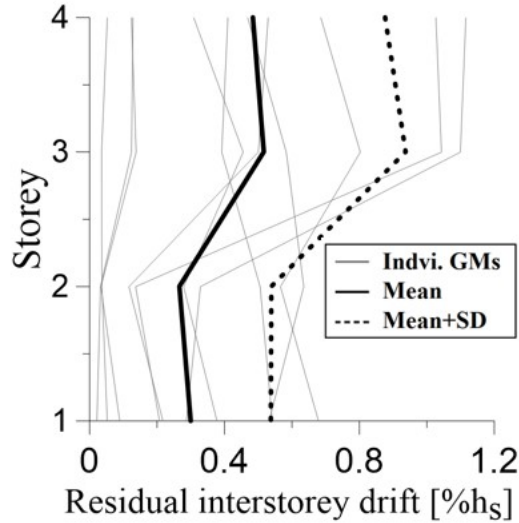


Figure 5.15 Distribution of residual interstorey drift along the height of FS-BF building under GMs scaled to comply with $I_E = 1.5$

Table 5.16 Distribution of floor acceleration along the height of FS-BF building equipped with FDs simulated with *BoucWen* material under GMs scaled to comply with $I_E = 1.5$ (E-W).

Distribution of floor acceleration at code level with $I_E = 1.5$ for BoucWen model											
St.	H	GM	GM	GM	GM	GM	GM	GM	GM	GM	GM
	(m)	(g)	(g)	(g)	(g)	(g)	(g)	(g)	(g)	(g)	(g)
4	18.2	0.693	0.651	0.664	0.658	0.669	0.798	0.644	0.745	0.502	0.773
3	13.8	1.046	0.565	0.993	0.680	0.832	1.260	0.747	0.795	0.647	0.875
2	9.4	0.864	0.674	0.807	0.769	1.147	1.212	0.894	0.941	0.841	0.826
1	5.0	0.869	0.584	0.848	0.647	0.893	0.968	0.736	0.793	0.730	0.764

In general, the addition of friction dampers reduced the floor acceleration of each storey compared to the MD-CBF systems. In addition, the floor acceleration does not vary significantly between different ground motions.

Analysing the FDs response, failure of friction dampers is expected when the seismic demand exceeds the available slip length and the pretensioned bolts impact the edge of slotted hole driving the pretensioned bolts to behave either in bearing or in shear. Hence, the length of slotted hole is an important parameter, which is able to control the seismic response of friction dampers.

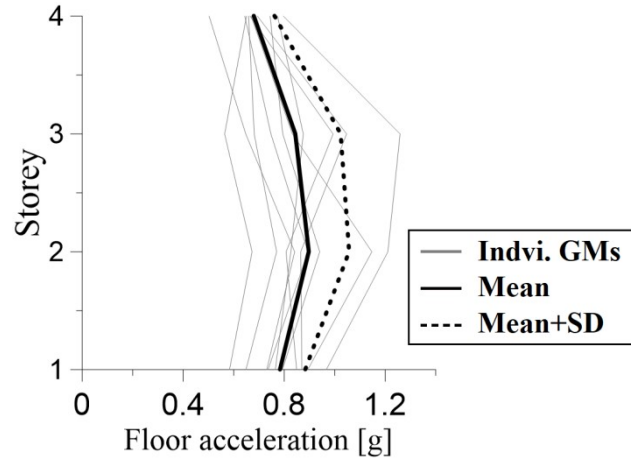


Figure 5.16 Distribution of floor acceleration along the height of FS-BF building under GMs scaled to comply with $I_E = 1.5$

On the one hand, if the length of slotted hole is too small, the energy dissipation capacity of the device is greatly reduced and the slip-lock phase is encountered earlier. On the other hand, if the slip length is too large (e.g. corresponding to $2.5\%h_s$ interstorey drift), important residual deformations are anticipated. The summary of the friction damper properties used hereon is shown in the Table 5.17. Considering the slip length recommendation of 65 mm, hysteretic loops of friction dampers and interstorey drift time-history series resulted under GM #1006 scaled at code level considering $I_E = 1.5$ are provided in Figure 5.17. In case that slip length remained unchanged as provided in Table 5.8 (slip length of 45 mm), the amplified ground motion GM #1006 drives friction dampers into the bearing phase as illustrated in Figure 5.18

Table 5.17 Slip force and slip length of FS-BF hospital building

Storey	Slip load, F_{slip}	$1.3F_{slip}$	C_r of brace	Slip length, Δ_s
	kN	kN	kN	mm
4	750	975	1013	65
3	1250	1625	1734	65
2	1550	2015	2053	65
1	1900	2470	2578	65

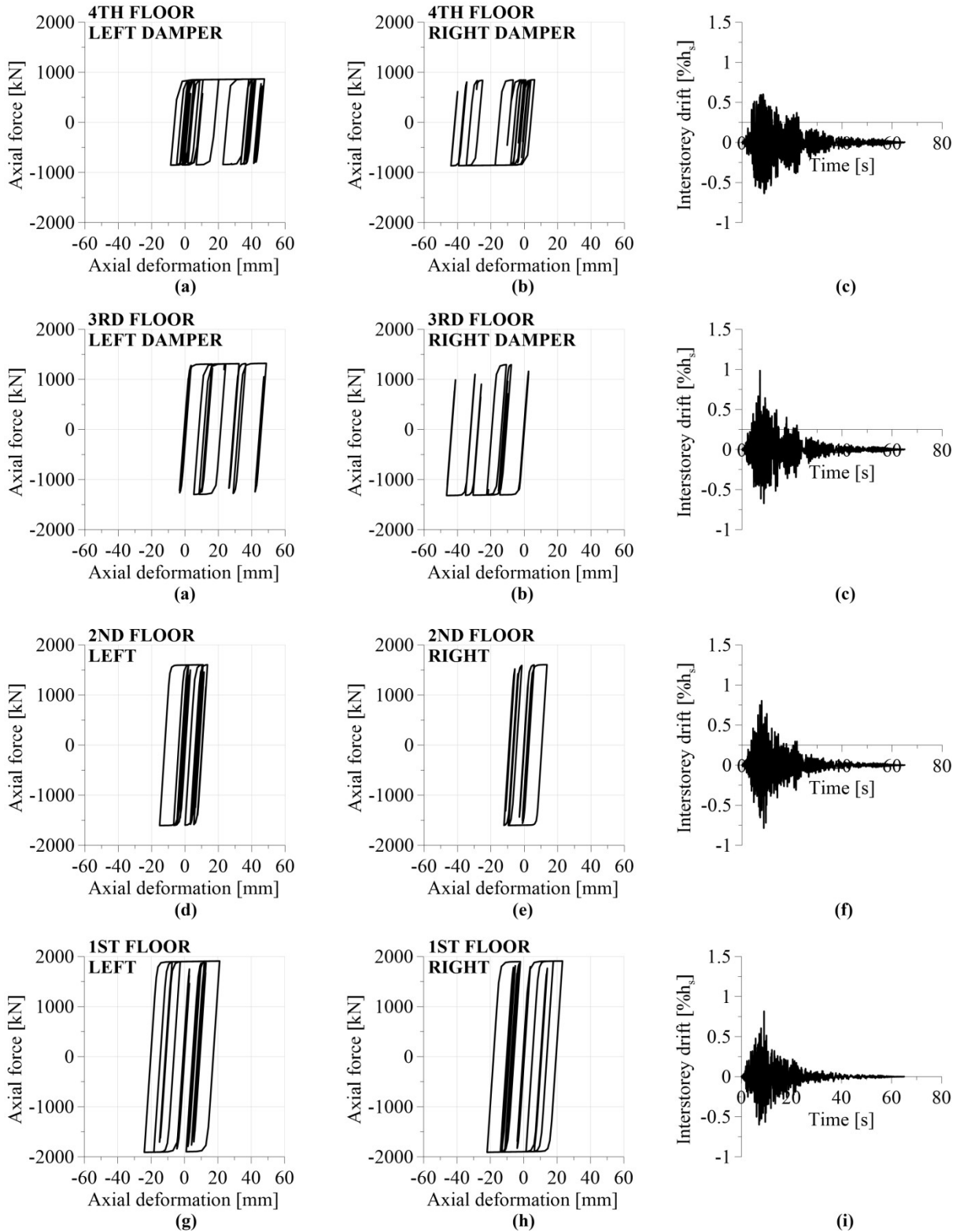


Figure 5.17 Hysteretic loops of friction damper and interstorey drift time-history series resulted under GM #1006 scaled at code level considering $I_E=1.5$ (slip length = 65 mm)

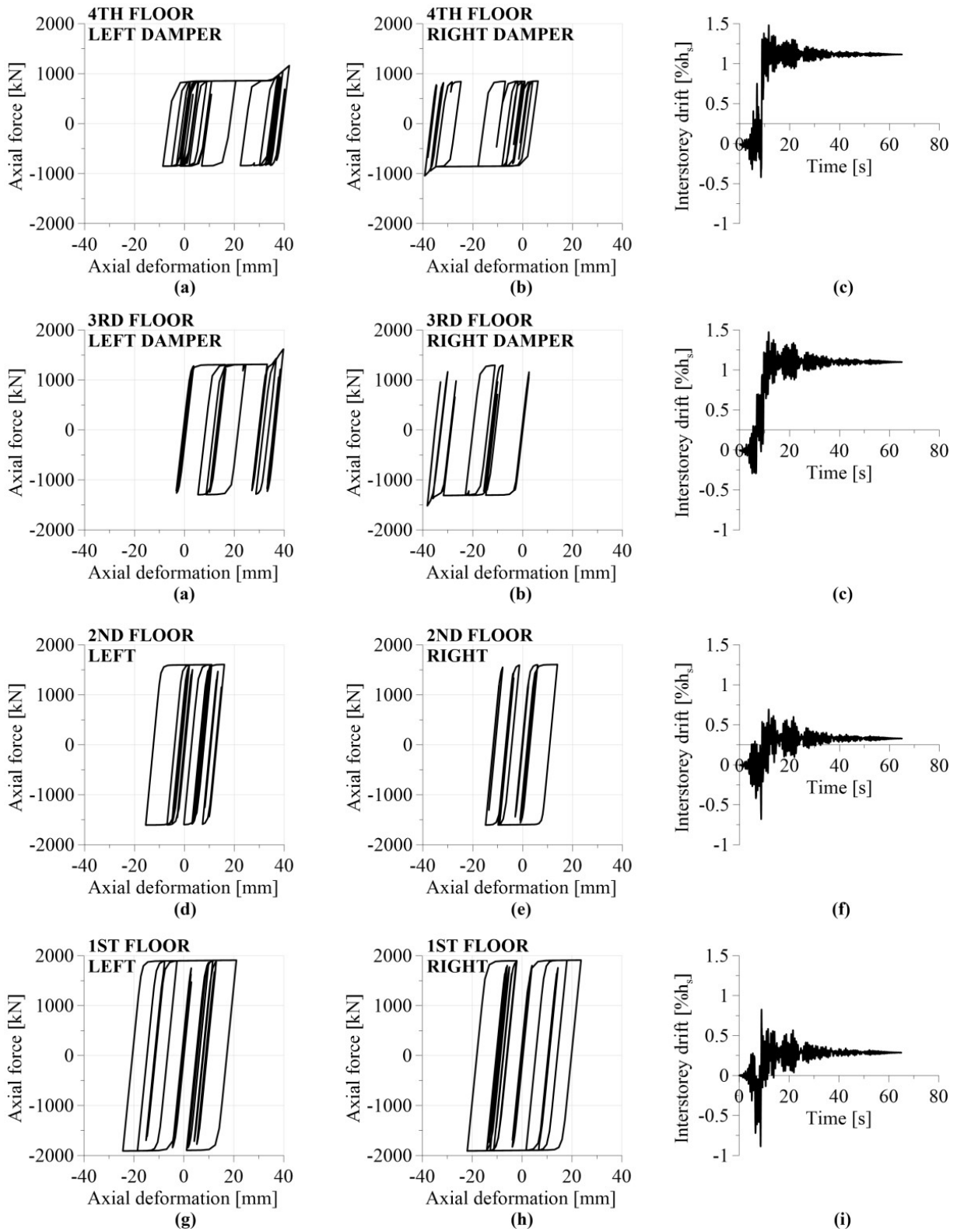


Figure 5.18 Hysteretic loops of friction damper and interstorey drift time-history series resulted under GM #1006 scaled at code level considering $I_E=1.5$ (slip length = 45 mm)

5.4 Comparison between MD-CBF and FS-BF seismic response

The peak interstorey drifts of FD-CBF are greater than those recorded from the MD-CBFs. To emphasize the difference, the Mean and the Mean+SD of residual drifts are given in Table 5.18 and Table 5.19 for $I_E=1$ and $I_E=1.5$, respectively.

Table 5.18 Comparison of interstorey drift distribution along the height of FS-BF and MD-CBF buildings under GMs scaled to match the design spectrum associated to $I_E=1$

Distribution of interstorey drifts comparison at code level with $I_E=1$							
St.	H (m)	Mean (% h_s)			Mean+SD (% h_s)		
		$2t_g$ linear	$8t_g$ elliptical	BW-EPPGap	$2t_g$ linear	$8t_g$ elliptical	BW-EPPGap
4	18.2	0.611	0.611	0.754	0.739	0.736	0.944
3	13.8	0.664	0.686	0.737	0.809	0.846	0.945
2	9.4	0.430	0.431	0.564	0.488	0.500	0.708
1	5.0	0.502	0.504	0.673	0.589	0.590	0.868

Table 5.19 Comparison of interstorey drift distribution along the height of FS-BF and MD-CBF buildings under GMs scaled to match the design spectrum associated to $I_E=1.5$

Distribution of interstorey drifts comparison at code level with $I_E=1.5$							
St.	H (m)	Mean (% h_s)			Mean+SD (% h_s)		
		$2t_g$ linear	$8t_g$ elliptical	BW-EPPGap	$2t_g$ linear	$8t_g$ elliptical	BW-EPPGap
4	18.2	0.705	0.704	1.094	0.901	0.901	1.337
3	13.8	1.001	1.033	1.052	1.324	1.377	1.341
2	9.4	0.506	0.508	0.835	0.603	0.611	1.065
1	5.0	0.797	0.801	1.041	1.193	1.190	1.300

From Tables 5.18 and 5.19 it results that the Mean drifts of the upper 2 floors are increased by approximately 15% when dampers are installed in-line with braces. Similarly, the Mean drifts on the bottom 2 floors increase by roughly 30%. Despite the increase in deformations, the interstorey drifts remain below or around the code limit of 1% h_s . In this manner, the FS-BF provides more uniformly distributed demand across the building height by engaging all friction damper devices into energy dissipation at the expense of having additional deformations. The distribution of interstorey drift of both systems subjected to GMs scaled to design spectrum with

$I_E=1$ and the response comparison is shown in Figure 5.19. A similar figure when the demand is associated to $I_E = 1.5$ is illustrated in Figure 5.20.

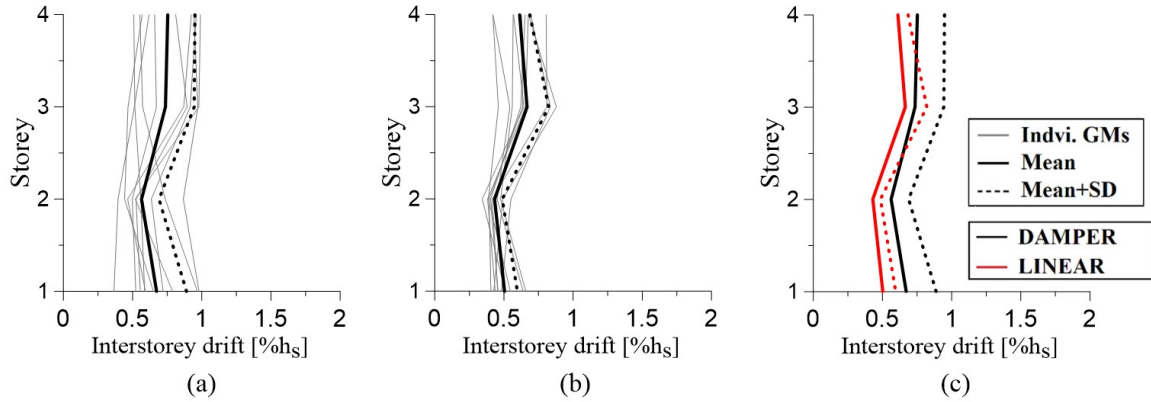


Figure 5.19 Distribution of interstorey drift along the building height under GMs scaled to comply with $I_E = 1$: a) BW & EPPGap material b) $2t_g$ linear model c) Comparison

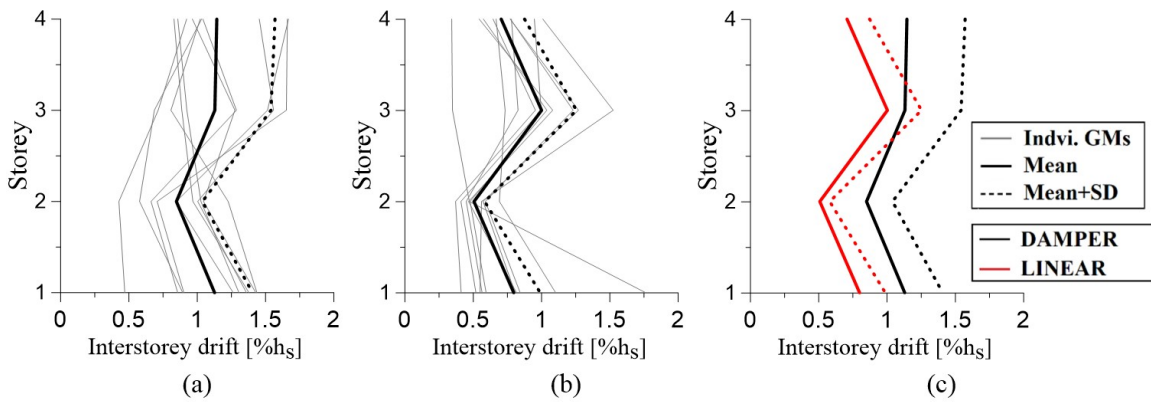


Figure 5.20 Distribution of interstorey drift along the building height under GMs scaled to comply with $I_E = 1.5$: a) BW & EPPGap material b) $2t_g$ linear model c) Comparison

The Mean and the Mean+SD of residual interstorey drifts are given in Table 5.20 and Table 5.21 for $I_E=1$ and $I_E=1.5$, respectively. The associated residual interstorey drift distribution along the building height for $I_E=1$ and $I_E=1.5$ are illustrated in Figures 5.21 and 5.22, respectively.

Table 5.20 Comparison of residual interstorey drift distribution along the height of FS-BF and MD-CBF buildings under GMs scaled to match the design spectrum associated to $I_E=1$

Distribution of residual drifts comparison at code level with $I_E=1$							
ST	H (m)	Mean (% h_s)			Mean+SD (% h_s)		
		$2t_g$ linear	$8t_g$ elliptical	BW-EPP	$2t_g$ linear	$8t_g$ elliptical	BW-EPP
4	18.2	0.054	0.059	0.365	0.085	0.093	0.627
3	13.8	0.057	0.063	0.353	0.107	0.115	0.599
2	9.4	0.036	0.035	0.189	0.055	0.054	0.364
1	5.0	0.046	0.048	0.210	0.071	0.077	0.394

Table 5.21 Comparison of residual interstorey drift distribution along the height of FS-BF and MD-CBF buildings under GMs scaled to match the design spectrum associated to $I_E=1.5$

Distribution of residual drifts comparison at code level with $I_E=1.5$							
St.	H (m)	Mean(% h_s)			Mean+SD (% h_s)		
		$2t_g$ linear	$8t_g$ elliptical	BW-EPP	$2t_g$ linear	$8t_g$ elliptical	BW-EPP
4	18.2	0.052	0.057	0.485	0.092	0.101	0.852
3	13.8	0.102	0.124	0.517	0.179	0.213	0.890
2	9.4	0.045	0.044	0.267	0.082	0.081	0.500
1	5.0	0.075	0.074	0.300	0.154	0.153	0.527

The residual interstorey drift envelope resulted from the building response for the $2t_g$ linear MD-CBF model is more uniformly distributed across the building height and yet it has residual drift values that are almost negligible compared to those of the FD-BF model. In the case of FD-BFs, the residual drift patterns are highly dependent on the ground motion. This is shown by the large gap between the Mean and the Mean+SD curve showed in the above Figures. Although, the Mean residual drifts are well below the $0.5\%h_s$ recommended limit, the Mean+SD values clearly violate this instruction. Hence, as predicted, a backup system with self-centering properties such as a moment-resisting frame (MRF) should be used in parallel with FD-BFs to reduce the residual drift.

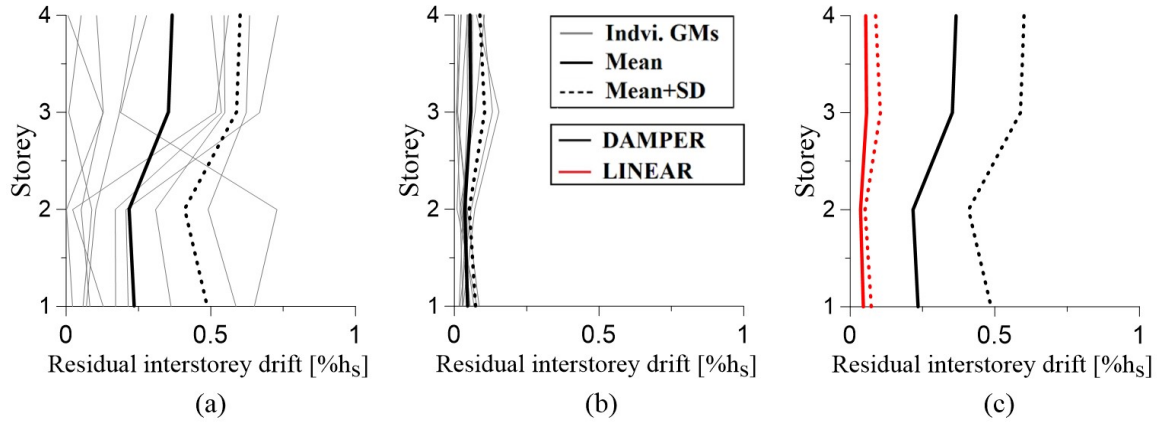


Figure 5.21 Distribution of residual interstorey drift along the building height under GMs scaled to comply with $I_E = 1.0$: a) BW & EPPGap material b) $2t_g$ linear c) comparison

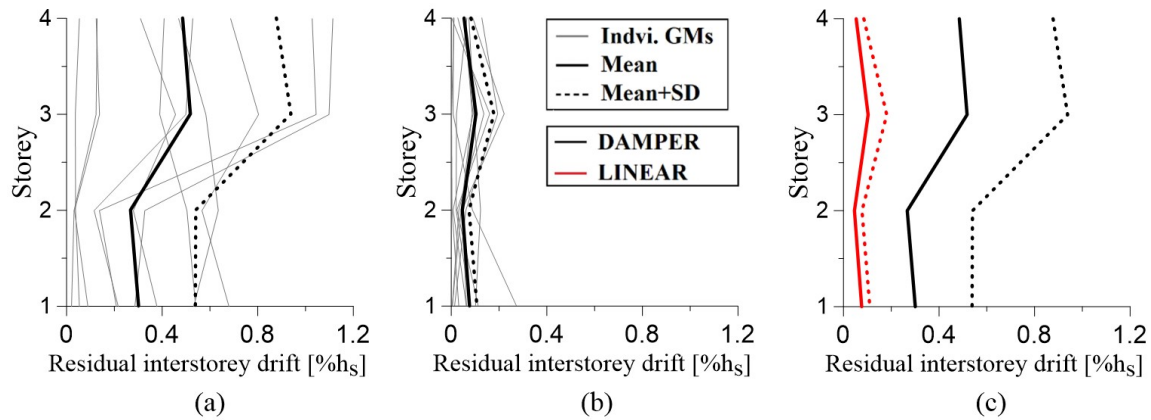


Figure 5.22 Distribution of residual interstorey drift along the building height under GMs scaled to comply with $I_E = 1.5$: a) BW & EPPGap b) $2t_g$ linear c) comparison

In the following Tables 5.22 and 5.23, it is shown the Mean and the Mean+SD of floor acceleration resulted under GMs scaled to comply with $I_E=1$ and $I_E=1.5$, respectively. The associated floor acceleration values distribution pattern along the building height is illustrated in Figures 5.23 and 5.24, respectively.

Table 5.22 Comparison of floor acceleration distribution along the height of FD-BF and MD-CBF buildings under GMs scaled to match the design spectrum associated to $I_E=1.0$

Distribution of floor acceleration comparison at code level with $I_E=1$							
St.	H (m)	Mean (% h_s)			Mean+SD (% h_s)		
		$2t_g$ linear	$8t_g$ elliptical	BW-EPPGap	$2t_g$ linear	$8t_g$ elliptical	BW-EPPGap
4	18.2	0.936	0.945	0.573	0.992	0.999	0.646
3	13.8	0.852	0.856	0.612	0.957	0.967	0.722
2	9.4	0.871	0.871	0.651	1.095	1.105	0.736
1	5.0	0.718	0.723	0.610	0.852	0.857	0.757

Table 5.23 Comparison of floor acceleration distribution along the height of FD-BF and MD-CBF buildings under GMs scaled to match the design spectrum associated to $I_E=1.5$

Distribution of floor acceleration comparison at code level with $I_E=1.5$							
St.	H (m)	Mean (% h_s)			Mean+SD (% h_s)		
		$2t_g$ linear	$8t_g$ elliptical	BW-EPPGap	$2t_g$ linear	$8t_g$ elliptical	BW-EPPGap
4	18.2	1.051	1.062	0.680	1.111	1.126	0.762
3	13.8	0.892	0.897	0.844	0.965	0.979	1.053
2	9.4	1.005	1.005	0.897	1.268	1.272	1.063
1	5.0	0.863	0.869	0.783	1.003	1.012	0.899

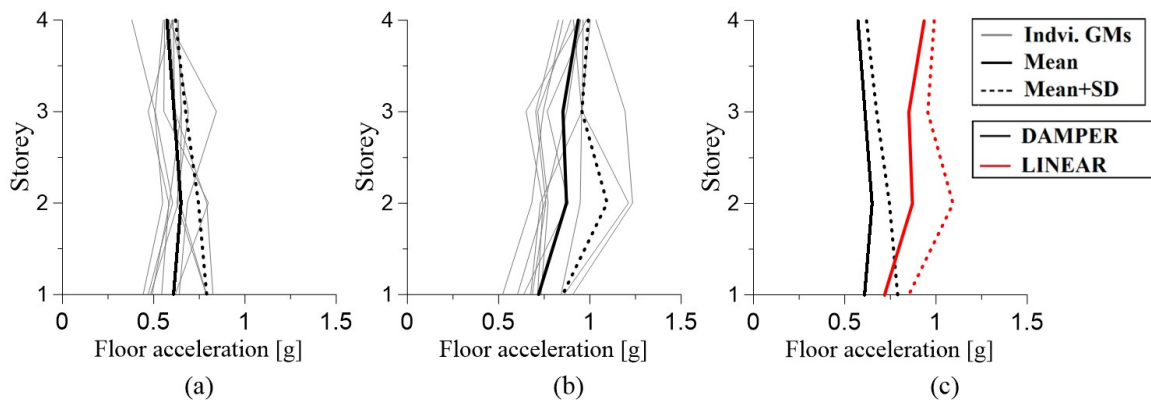


Figure 5.23 Distribution of floor acceleration along the building height under GMs scaled to comply with $I_E=1.0$: a) BW & EPPGap material b) $2t_g$ linear c) both models.

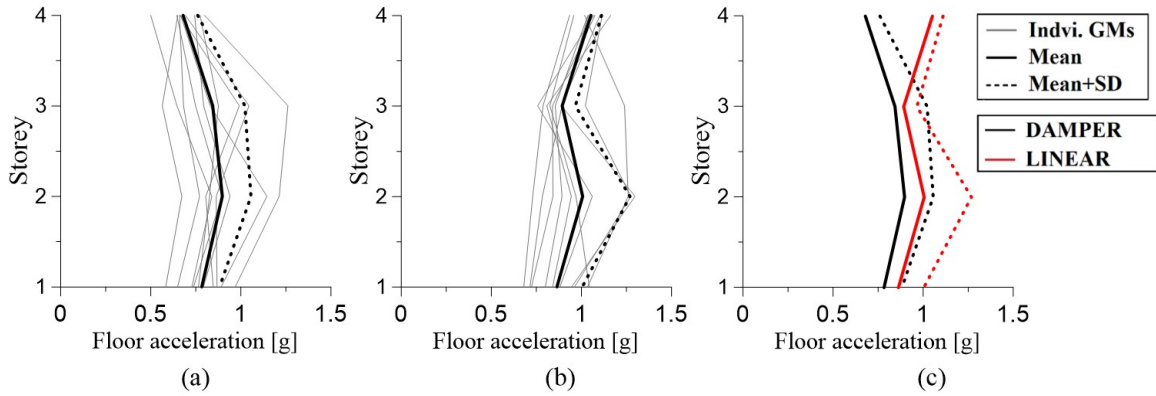


Figure 5.24 Distribution of floor acceleration along the building height under GMs scaled to comply with $I_E = 1.5$: a) BW & EPPGap material b) $2t_g$ linear c) both models.

In general, the accelerations recorded at floors of MD-CBFs are larger than those resulted for the FD-BF. Moreover, the distribution of the floor acceleration envelope is more favorable when friction dampers are installed. The ability to select the desired slip load with respect to the demand is an additional benefit of friction dampers. By an iterative design process, the structure can be opted to engage all friction dampers at all floors to yield simultaneously or in a preferred sequence to further improve the distribution of drift and acceleration envelopes. The benefit of reducing the floor acceleration of a building by using a FS-BF system instead of a MD-CBF system comes at the expense of increased residual drifts. The designer must first assess, which of these parameters is more critical to the function of the building and then to optimize the design.

5.5 FS-BF with Continuous Columns

In the previous case, columns of FS-BF were continuous over two storeys. Herein, it is proposed to mitigate the residual interstorey drifts by making the FS-BF's columns continuous across the building height. If the results are not satisfied, a back-up moment-resisting frames designed to carry 25% of base shear could be added in parallel to the FS-BF system. The effects of using FS-BFs with continuous columns are presented by using data resulted from the nonlinear time-history analyses. The seismic response is expressed in terms of interstorey drift, residual interstorey drift and floor acceleration. Considering the same 10 GMs scaled to comply with $I_E = 1$, the distribution of peak interstorey drift is given in Table 5.24 and is depicted in Figure 5.25a, while a comparison of drifts between the FS-BF without continuous columns and with continuous columns (FS-BF_{CC}) is shown in Figure 5.25c.

Table 5.24 Distribution of peak interstorey drifts of FS-BF_{CC} under GMs scaled for at $I_E = 1$

Distribution of interstorey drift at code level with $I_E = 1$ for BoucWen model with continuous column											
ST	H (m)	GM 739 (%h _s)	GM 986 (%h _s)	GM 1006 (%h _s)	GM 57 (%h _s)	GM 1077 (%h _s)	GM 1039 (%h _s)	GM 767 (%h _s)	GM 963 (%h _s)	GM 796 (%h _s)	GM 787 (%h _s)
4	18.2	0.689	0.748	0.992	0.527	0.914	0.577	0.700	0.998	0.592	1.069
3	13.8	0.578	0.700	0.821	0.501	0.712	0.399	0.453	0.708	0.689	0.740
2	9.4	0.526	0.619	0.592	0.577	0.538	0.436	0.405	0.500	1.061	0.731
1	5.0	0.511	0.615	0.803	0.593	0.628	0.647	0.361	0.737	1.547	1.084

The overall shape of the interstorey drift envelope is different between the FS-BF with continuous columns (FS-BF_{CC}) and the FS-BF with columns continuous over 2 storeys (FS-BF). The difference in interstorey drifts at the 2nd and 3rd floor is reduced in the case of FS-BF_{CC} systems. Furthermore, the Mean+SD interstorey drift is slightly less in the case of FS-BF_{CC} when compared with that of FS-BF. The maximum residual interstorey drifts obtained under the 10 scaled GMs are shown for FS-BF_{CC} in Table 5.25 and the residual interstorey drift is illustrated in Figure 5.26. As depicted, the residual interstorey drift is substantially reduced (e.g. Mean+SD residual interstorey drift < 0.5h_s) when FS-BF_{CC} is used.

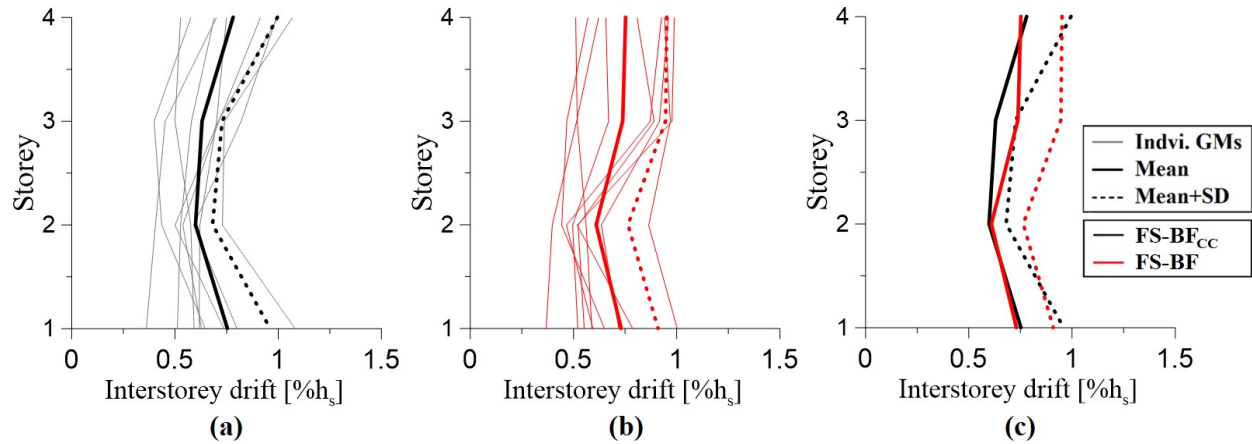


Figure 5.25 Distribution of interstorey drift along the building height under GMs scaled to comply with $I_E = 1.0$: a) FS-BF_{CC} b) FS-BF c) Comparison of FS-BF_{CC} & FS-BF response

Table 5.25 Distribution of residual interstorey drifts of FS-BF_{CC} under GMs scaled for $I_E = 1$

Distribution of residual interstorey drift at code level with $I_E = 1$ for BoucWen model with continuous column											
ST	H (m)	GM 739 (%h _s)	GM 986 (%h _s)	GM 1006 (%h _s)	GM 57 (%h _s)	GM 1077 (%h _s)	GM 1039 (%h _s)	GM 767 (%h _s)	GM 963 (%h _s)	GM 796 (%h _s)	GM 787 (%h _s)
4	18.2	0.198	0.419	0.732	0.071	0.521	0.013	0.111	0.383	0.219	0.632
3	13.8	0.088	0.338	0.500	0.033	0.328	0.055	0.065	0.151	0.176	0.224
2	9.4	0.048	0.265	0.281	0.088	0.060	0.018	0.007	0.139	0.508	0.261
1	5.0	0.039	0.246	0.258	0.060	0.108	0.094	0.015	0.269	0.510	0.501

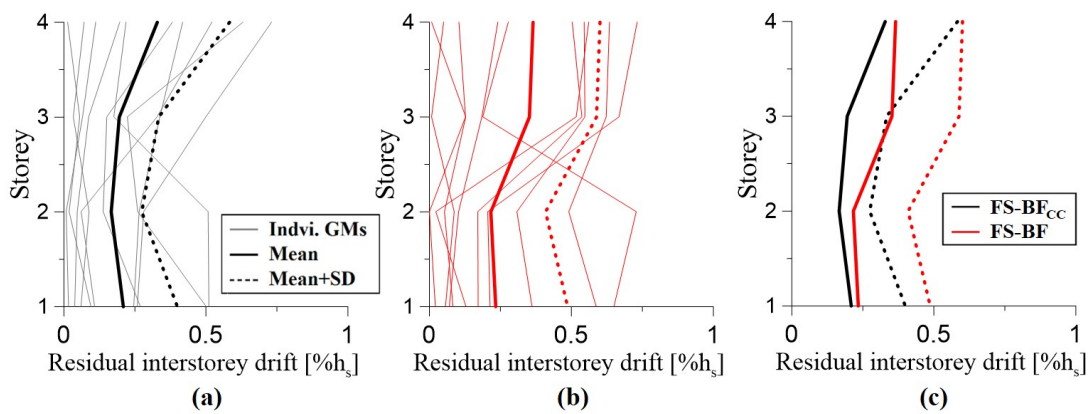


Figure 5.26 Distribution of residual interstorey drift along the building height under GMs scaled to comply with $I_E = 1.0$: a) FS-BF_{CC} b) FS-BF c) Comparison of FS-BF_{CC} & FS-BF response

From Figure 5.26 is concluded that significant improvements of residual interstorey drifts are obtained when continuous columns are used. By providing continuous columns over the building height, the FS-BF_{CC} system is less prone to exhibit soft-storey like behavior. Distribution of floor acceleration resulted under the 10 scaled GMs are given in Table 5.26 and the peak floor acceleration envelopes are depicted in Figure 5.27a. A comparison of Mean and Mean+SD floor acceleration resulted for FS-BF_{CC} and FS-BF is presented in Figure 5.27c. As depicted, no reduction in floor acceleration is noted.

Table 5.26 Distribution of floor accelerations of FS-BF_{CC} under GMs scaled for I_E=1

Distribution of floor acceleration at code level with I _E =1 for BoucWen model with continuous column										
ST	GM 739 (g)	GM 986 (g)	GM 1006 (g)	GM 57 (g)	GM 1077 (g)	GM 1039 (g)	GM 767 (g)	GM 963 (g)	GM 796 (g)	GM 787 (g)
4	0.615	0.602	0.597	0.550	0.606	0.626	0.588	0.566	0.622	0.646
3	0.620	0.462	0.651	0.516	0.712	0.629	0.841	0.558	0.816	0.569
2	0.828	0.566	0.655	0.543	0.752	0.635	0.699	0.800	0.965	0.573
1	0.803	0.527	0.490	0.445	0.820	0.775	0.605	0.579	0.757	0.473

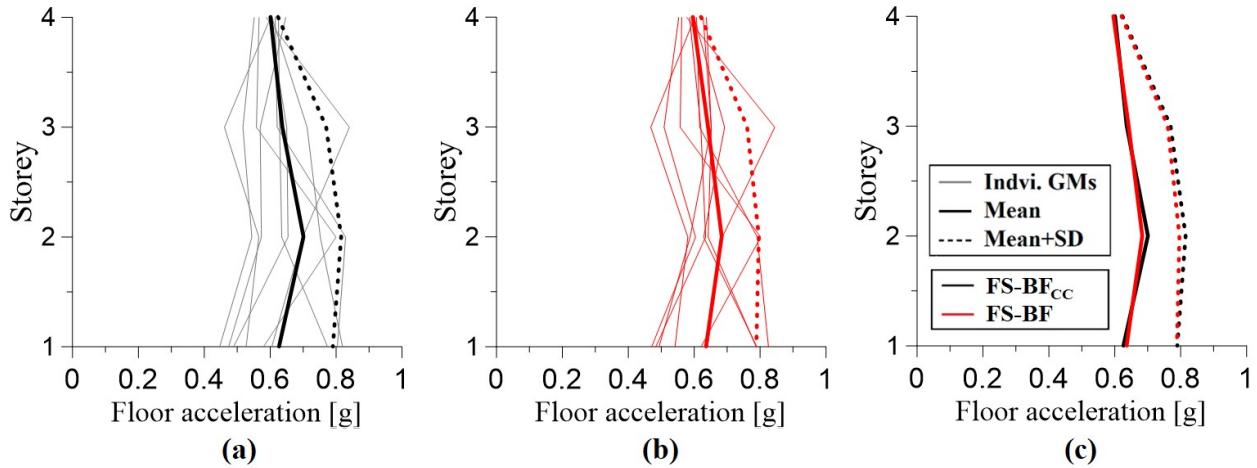


Figure 5.27 Distribution of floor acceleration along the building height under GMs scaled to comply with I_E = 1.0: a) FS-BF_{CC} b) FS-BF c) Comparison of FS-BF_{CC} & FS-BF response

Chapter 6

CONCLUSION AND FUTURE WORK

6.1 Conclusions

In this study, the seismic performances of a 4-storey hospital building equipped with MD-CBFs with improved connection detailing and FS-BFs are evaluated against the current code provisions using nonlinear dynamic analysis. The following findings are reported and some guidelines related to seismic design of post-disaster buildings are proposed.

- There are no straightforward guidelines on conducting nonlinear time-history analysis for post-disaster buildings. It is understood that in the preliminary design, the base shear used to design the SFRS is increased by the earthquake importance factor $I_E=1.5$. Hence, the SFRS system possesses higher strength. Moreover, when linear elastic analysis is used by means of the Modal Response Spectrum, the deflection should be amplified by the ratio R_dR_0/I_E . However, when nonlinear dynamic analyses are conducted by means of time-history analysis, it is not specified if ground motions are scaled to match the design spectrum over the period of interest using $I_E = 1.0$ or are scaled to match the design spectrum amplified by $I_E = 1.5$. To investigate the seismic response of the prototype hospital building, two cases are considered for scaling GMs: (i) to fit the design spectrum amplified with $I_E=1$ over the period of interest and (ii) to fit the design spectrum amplified with $I_E=1.5$. Structural members and connections should not fail under both scenarios. When more than 7 ground motions are used, the peak of mean interstorey drift should be below the $1\%h_s$, which is the code limit and the peak of mean residual interstorey drift should be less than $0.5\%h_s$.
- In general, the governing failure modes for gusset plates are block shear failure and net rupture. If the computed gusset plate thickness, $t_{g,req}$ does not meet all the requirements, it is recommended to increase the weld length L_w rather than the thickness of gusset plate t_g . As previously mentioned, thinner brace-to-frame connections tend to perform

better. Furthermore, by increasing the weld length, thinner weld leg width, D_w may also be achieved; which is beneficial for both cost and on-site constructability.

- In the case where block shear failure of HSS brace governs the design, it may be advantageous to start the design by assuming the weld length to be equal to two times the width of the attached brace ($L_w = 2w$) and to determine the required weld leg width D_w accordingly. In this manner, the framing system is less prone to shear lag effects and promotes thinner gusset plates.
- When gussets with $8t_g$ elliptical clearance are provided, the rotation capacity increases and larger axial deformation is achieved, as well as larger energy dissipation capacity. However, there were no significant changes in the overall behaviour of the building system. Due to the building's post-disaster design requirements that limits the interstorey drift to $1\%h_s$, the potential gain in performance from linear to elliptical clearance model is reduced. In other words, by restricting the brace to undergo larger axial deformation, the amount of energy dissipated by the brace becomes smaller. Furthermore, the importance factor of 1.5 applied to post-disaster structures increases significantly the forces in members and connections. Hence, thicker gusset plates are required. With thick gusset plates, the benefit of the $8t_g$ elliptical clearance model is further reduced. Nevertheless, the $8t_g$ elliptical clearance band does have a more desirable distribution of stresses at the interface of brace-to-frame connections, which minimizes the likelihood of tear.
- During the initial design phase, the overall height HT and width WT of gusset plates are often too large. By increasing the weld leg width D_w , shorter weld length L_w are achieved, which in turn produces a more compact gusset plate connection. Furthermore, the larger the gusset plate connection, the shorter the effective brace length become. Stocky braces tend to have less rotational capacity, hence should be avoided.
- In the case of FS-BF, it is proposed to select the design slip length, u_{slip} , based on the maximum value between the peak of Maximum slip length and the slip length associated with interstorey drift of $1\%h_s$ for post-disaster buildings. The selected slip length, u_{slip} , is then increased by 130% to obtain the damper's stroke, $1.3u_{slip}$, which for the case study is

45 mm. This will ensure that the FD-BF do not go in the slip-lock phase under ground motions scaled to match the design spectrum associated to $I_E = 1$. However, when the demand is associated to ground motions scaled to design spectrum amplified by $I_E = 1.5$, the damper's stroke requirement is 65 mm. To assure sufficient stroke length is provided for friction dampers employed in post-disaster buildings, it is recommended to establish the stroke parameter from the results obtained under GMs amplified by $I_E = 1.5$.

- Comparing the seismic response of MD-CBF with that of FS-BF, it resulted that larger residual interstorey drift was obtained for FS-BF subjected to crustal ground motions and larger floor acceleration for the MD-CBF. Caution should be used when selecting the FS-BF system, which is prone to residual interstorey drift. To improve the response of FS-BF in terms of residual drift, the case with continuous columns was proposed. Thus, for low-rise buildings, it is recommended to use FS-BF with continuous columns. When the results are still not satisfactory, a Dual system composed of FS-BF and 25% MRF system is recommended. It is worth mentioning that the 25% MRF should be designed to carry an additional 25% base shear.
- Under severe ground motions, friction dampers could go into the bearing stage, while high axial forces are transferred to the columns of braced frame. It is worth mentioning that friction dampers may not fail when forces reach $2F_{slip}$ in bearing. To avoid column failures a second fuse should be added to the system.

6.2 Recommendation for Future work

The following work is proposed to further the research of friction dampers installed in-line with braced frames:

- Conduct experimental testing on friction dampers to assess the failure mechanism. Both the initial stiffness k_i and the bearing stiffness coefficient k_b should be measured to obtain the hysteresis backbone curve.
- Braces of FS-BF are designed to carry 1.3 times the design slip force. If friction dampers can withstand up to $2F_{slip}$, the attached brace are likely to buckle out-of-plane under

severe compressive forces. Once the brace buckles, the friction damper may be misaligned with respect to the brace and will no longer be able to dissipate the energy through friction sliding. An investigation on the maximum rotation leading to misalignment of brace with friction damper is recommended.

- Investigate the response of FS-BF systems with continuous columns for buildings with different height and occupancy types.
- Investigate the seismic response of Dual system formed by FS-BF and 25% MRF in order to reduce the residual interstorey drift.
- Analyse the building response under subduction type ground motions that are characterized by long duration and several loading/ unloading cycles

REFERENCES

American Society of Civil Engineers, ASCE (2000). "Prestandard and Commentary for the Seismic Rehabilitation of Buildings." *Federal Emergency Management Agency, FEMA-356*, Washington, D.C.

Aguero, A., Izvernari, C., Tremblay, R. (2006). "Modelling of the Seismic Response of Concentrically Braced Steel Steel Frames using the OpenSees Analysis Environment." *International Journal of Advanced Steel Construction*, 2(3), pp 242-274.

Aiken, I.D., Kelly, J.M., Pall, A.S. (1988). "Seismic response of a nine-story steel frame with friction damped cross-bracing." *Proc. 9th World Conference on Earthquake Engineering*, Tokyo/Kyoto, Japan.

Applied Technology Council, (1992). "Guidelines for Cyclic Seismic Testing of Components of Steel Structures." *Report ATC-24*, Redwood City, CA.

Aslani, F., Goel, S. (1989). "Experimental and Analytical Study of the Inelastic Behavior of Double Angle Bracing Members Under Severe Cyclic Loading," *Research Report UMCE 89-5*, Department of Civil Engineering, University of Michigan, Michigan.

Astaneh-Asl, A., Goel, S.C., Hanson, R.D. (1982). "Cyclic Behavior of Double Angle Bracing Members with End Gusset Plates." *Research Report UMEE 82R7*, Department of Civil Engineering, University of Michigan, Michigan.

Astaneh-Asl, A., Goel, S.C., Hanson, R.D. (1985). "Cyclic Out-ofPlane Buckling of Double-Angle Bracing. *Journal of Structural Engineers.*" *ASCE*, 111, pp. 1135-1153.

Astaneh-Asl, A. (1998). "Seismic Behaviour and Design of Gusset Plates." *Steel TIPS, Journal of Structural Steel Educational Council*, Moraga, California.

Atkinson, G. (2009). "Earthquake time histories compatible with the 2005 NBCC uniform hazard spectrum." *Canadian Journal of Civil Engineering*, 36(6), 991-1000.

Baber, T., Wen, Y. (1981). "Seismic response of hysteretic degrading structures." *Journal of Engineering Mechanics*, ASCE, Vol. 107, No 6, 1067-1087.

- Baker, J. W., (2009). “The conditional mean spectrum: A tool for ground motion selection.” *ASCE, Journal of Structural Engineering*.
- Bruneau, M., Uang C.M., Whittaker, A. (1998) “Ductile Design of Steel Structures.” *McGraw-Hill*, Boston.
- Canadian Standard Association(2009), CAN/CSA-S16-09. “Limit States Design of Steel Structures.” *Canadian Standard Association*, Toronto, ON.
- Clark. K.A. (2009). “Experimental Performance of Buckling Restrained Braced Frames.” Department of Civil Engineering, University of Washington, Seattle, Washington.
- Christopoulos, C., Filiatrault, A. (2006). “Passive supplemental damping and seismic isolation.” *Instituto Universitario di Studi Superiori di Pavia*, IUSS Press.
- Federal Emergency Management Agency (FEMA) (2000). “Prestandard and Commentary for the Seismic Rehabilitation of Buildings.” FEMA-356, Washington, D.C.
- Federal Emergency Management Agency (FEMA) (2009). “NEHRP Recommended seismic provisions for new buildings and other structures.” FEMA-450, Washington, D.C.
- Filiatrault A, Cherry S (1988). “Seismic design of friction damped braced steel plane frames by energy methods.” *Earthquake Engineering Research Laboratory report UBC-EERL-88-01*, Department of Civil Engineering, University of British Columbia, Vancouver.
- Filiatrault A, Cherry S (1990). “Seismic design spectra for friction damped structures.” *ASCE, Journal of Structural Engineering*, 116(5):1334–1355.
- Grondin, G.Y., Nast, T.E., Cheng, J.J.R. (2000). “Strength and Stability of Corner Gusset Plates Under Cyclic Loading.” *Proceedings of Annual Technical Session and Meeting*, Structural Stability Research Council.
- Hardash, S., Bjorhovde, R. (1985). “New Design Criteria for Gusset Plates in Tension.” *Engineering Journal*, AISC, Col. 22, No. 2, Second Quarter, 1985.
- Hsiao, P-C, Lehman, D.E., Roeder, C.W. (2012). “Improved analytical model for special concentrically braced frames.” *Journal of Constructional Steel Research*, Vol. 73, pp. 80-94.

- Hsiao, P-C, Lehman, D.E., Roeder, C.W. (2013a). “A model to simulate special concentrically braced frames beyond brace fracture.” *Earthquake Engineering and Structural Dynamics*, Wiley, Vol. 42, pp. 183-200.
- Hsiao, P-C, Lehman, D.E., Roeder, C.W. (2013b). “Evaluation of response modification coefficient and collapse potential of SCBFs.” *Earthquake Engineering and Structural Dynamics*, Wiley, DOI: 10.1002/eqe.2286.
- Ikeda, K. and Mahin, S. (1984). “A Refined Physical Theory Model for Predicting the Seismic Behaviour of Braced Steel Frames.” *Report no. UCB/EERC-84/12*, Earthquake Engineering Research Center, University of California, Berkeley, California.
- Johnson, S.M. (2005). “Improved Seismic Performance of Special Concentrically Brace Frames.” Department of Civil Engineering, University of Washington, Seattle, WA, June 2005
- Karamachi, E., Lignos, D. (2013). “Predictive equations for modelling cyclic buckling and fracture of steel braces.” *The 10th International Conference on Urban Earthquake Engineering*, Tokyo 2013, pp. 105-107.
- Kahn LF, Hanson RD. 1976. “Inelastic cycles of axially loaded steel members.” *Journal of the Structural Division*, **102**: 947-959
- Lamarche, C.P., Tremblay, R., (2008) “Accounting for Residual Stresses in the Seismic Stability of Nonlinear Beam-Column Elements with Cross-Section Fiber Discretization.” *Annual Stability Conference 2008*, P. 59-78.
- Lehman, D.E., Roeder, C.W., Herman, D., Johnson, S., Kotulka, B. (2008). “Improved seismic performance of gusset plate connections.” ASCE, *Journal of Structural Engineering*, Vol. 134, No. 6, Reston, VA, pp. 890-901.
- Lehman, D.E., Roeder, C.W., (2008). “Influence of connection design parameters on the seismic performance of braced frames.” *Journal of Constructional Steel Research* 64 607-623.
- Liu, J., Astaneh-Asl, A., (2004). “Moment-Rotation Parameters for Composite Shear Tab Connections.” *Journal of structural engineering*, ASCE, 130(9).

- Lumpkin, E.J. (2009). “Enhanced seismic performance of multi-story special concentrically braced frames using a balanced design procedure.” MScEthesis, University of Washington, Seattle, WA.
- Lukkunaprasit, P., Wanitkorkul, A., Filiatrault, A. (2004). “Performance deterioration of slotted-bolted connection due to bolt impact and remedy by restrainers.” *Proc. 13th World Conference on Earthquake Engineering*, Vancouver, B.C., No. 1986.
- Martinez-Saucedo, G., Packer, J.A. (2009). “Static design recommendations for slotted end HSS connections in tension.” *Journal of Structural Engineering*, ASCE, 135(7), 797-805.
- Mazzoni, S., McKenna, F., Scott, M., Fenves, G. et al. (2007). OpenSees User Manual, <http://opensees.berkeley.edu/OpenSees/manuals/usermanual/OpenSeesCommandLanguageManual.pdf>.
- McKenna, F. (1997). “Object Oriented Finite Element Analysis: Frameworks for Analysis Algorithms and Parallel Computing.” Ph.D. Thesis, Department of Civil Engineering, University of California, Berkeley, CA.
- McKenna, F., Fenves, G.L. (2004). “Open System for Earthquake Engineering Simulation (OpenSees).” *Pacific Earthquake Engineering Research Center (PEER)*, University of California, Berkeley, CA. (<http://opensees.berkeley.edu/index.html>).
- Morales, J.D. (2011). “Numerical simulations of steel frames equipped with friction-damped diagonal-bracing devices.” MSc thesis, Building, Civil and Environmental Engineering, Concordia University, Montreal.
- Morales, J.D., Tirca L (2012). “Numerical simulation and design of friction-damped steel frame structures.” *The 15th world conference in earthquake engineering*, Lisbon, paper #2538
- Pall, A., Marsh, C. (1982). “Response of friction damped braces.” *Journal of Structures Division*, ASCE, Vol. 108, No. ST6, 1313-1323.
- Pall, A. (1979). “Limited slip bolted joints: a device to control the seismic response of large panel structures.” PhD Thesis, Building, Civil and Environmental Engineering, Concordia University, Montreal, QC.

- Powell, J., Clark, k., Tsai, K.C., Roeder, C., Lehman, D. (2008). "Test of a full-scale concentrically braced frame with multi-story X-bracing." *Proceedings of Structures Congress 2008*, Vancouver, Apr24-26, 2008.
- Rabinovitch, J., Cheng, R. (1993). "Cyclic behaviour of steel gusset plate connections." University of Alberta, Department of Civil Engineering, Structural Engineering Report, n 19.
- Roeder, C.W., Lumpkin, E.J., Lehman, D.E. (2011). "Balanced design procedure for special concentrically braced frame connections." Elsevier, *Journal of Constructional Steel Research*, Vol. 67 No. 11, pp. 1760-72.
- Roeder, C.W., Sabelli, R., Hajjar, J.F., (2013). "Seismic Design of Steel Special Concentrically Braced Frame Systems." NIST GCR 13-917-24
- Roik, K., Dorka, U. (1986). "Testing of Structural Joints under Earthquake Loadings Using a New Deterministic Testing Procedure." *Proceedings from the 2nd International Conference on Earthquake Prognostics, Hazard Assessment, Evaluation and Damage Prevention*, Berlin, FRG: 463-478
- Shaback, B., Brown, T., (2003). "Behaviour of Square Hollow Structural Steel Braces with End Connections under Reversed Cyclic Axial Loading." *Canadian Journal of Civil Engineering*, 30 (4) pp. 745-753.
- Sherstobitoff, J., Rezai, M., Wong, M. (2004). "Seismic Upgrade of Lions Gate Hospital's Acute Tower South." *The 13th World Conference on Earthquake Engineering*, Vancouver, B.C., Canada, Paper No. 1423
- Song, J., Der Kiureghian, A. (2006). "Generalized Bouc-Wen model for highly asymmetric hysteresis." *Journal of Engineering Mechanics*, ASCE, Vol. 132, No. 6, 610-618.
- Symans, M.D., Charney, F.A., Whittaker, A.S., Constantinou, M.C., Kircher, C.A., Johnson, M.W., McNamara, R.J. (2008). "Energy Dissipation Systems for Seismic Applications: Current Practice and Recent Developments." *Journal of Structural Engineering*, ASCE, 134.10.1061, ASCE 0733-94451 134:1 (3)

Tirca, L. (2015). "Friction Dampers for Seismic Protections of Steel Buildings Subjected to Earthquakes: Emphasis on Structural Design." *Encyclopedia of Earthquake Engineering*, Springer, Berlin, Heidelberg, 978-3-642-35344-4.

Tirca, L., Morales, J.D., Guo, G.L., Chen, L. (2010). "Optimal design of friction dampers for multi-storey buildings." *Proc. 9th US National and 10th Canadian Conference on Earthquake Engineering: Reaching Beyond Borders*, EERI, Toronto, ON.

Tirca, L., Ohira M. (2016). "Nonlinear Response of a CBF hospital building with and without Friction Damper Devices." *The International Colloquium on Stability and Ductility of Steel Structures*, Timisoara, Romania.

Tirca, L., Serban, O., Tremblay, R., Jiang, Yan. (2018). "Seismic Design, Analysis and Testing of a Friction Steel Braced Frame System for Multi-Storey Buildings in Vancouver." *Key Engineering Material*, ISSN 1662-9809, Vol. 763, pp 1077-1086

Tremblay, R. (1993). "Seismic behavior and design of friction concentrically braced frames for steel buildings." PhD Thesis, University of British Columbia, Vancouver, B.C.

Tremblay, R., Archambault, M.-H., Filiatrault, A. (2003). "Seismic Response of Concentrically Braced Steel Frames Made with Rectangular Hollow Bracing Members." *ASCE Journal of Structural Engineering* 129 (12), pp. 1626-1636.

Tremblay, R. (2002). "Inelastic Seismic Response of Steel Bracing Members." *Journal of Constructional Steel Research*, 58, pp. 665-701

Uriz, P., Filippou, F.C., Mahin, S. (2008). "Model for Cyclic Inelastic Buckling of Steel Braces, *Journal of Structural Engineering*." ASCE, pp. 619-628.

Uriz, P. and Mahin, S. (2008). "Toward Earthquake Resistant Design of Concentrically Braced Steel Frame Structures." PEER 2008/08 report

Uriz, P. and Mahin, S. (2004). "Seismic Performance Assessment of Concentrically Braced Steel Frames." *Proc. 13th World Conference on Earthquake Eng.*, Vancouver, BC., Paper No. 1639.

Uriz, P., Mahin, S. A. (2004). "Seismic Vulnerability Assessment of Concentrically Braced Steel Frames." *International Journal of Steel Structures*, 4(4), 239-248.

Wakabayshi, M., Nakamura, T., Yoshida, N., “Experimental Studies on the Elastic-Plastic Behavior of Brace Frames under Repeated Horizontal Loading, Part 2” Kyoto University, Kyoto, Japan, March 1980

Whitmore, R.E. (1952). “Experimental Investigation of Stresses in Gusset Plates.” Bulletin No. 16. University of Tennessee Engineering Experiment Station, Knoxville, TN.

Yoo, J.H., Roeder, C., Lehman, D. (2008). “Analytical performance simulation of special concentrically braced frames.” ASCE, *Journal of Structural Engineering*, Vol. 134 No. 6, pp. 190-198.

Yoo, J.H., Lehman, D., Roeder, C. (2008). “Influence of gusset plate parameters on the seismic resistance of braced frames.” *Journal of Constructional Steel Research*, 64, pp. 607-623.